University of Ljubljana

Faculty of Electrical Engineering

Peter Lombergar

Numerical modeling of temperature distribution during electroporation based treatments in fluid flow conditions

DOCTORAL DISSERTATION

Mentor: Assoc. Prof. Bor Kos, PhD

Ljubljana, 2025

Univerza v Ljubljani

Fakulteta za elektrotehniko

Peter Lombergar

Numerično modeliranje temperature pri elektroporaciji ob prisotnosti pretokov tekočin

DOKTORSKA DISERTACIJA

Mentor: izr. prof. dr. Bor Kos

Ljubljana, 2025

UNIVERZA V LJUBLJANI | FE Fakulteta za elektrotehniko

Senat Fakultete za elektrotehniko Univerze v Ljubljani je na seji dne, 08.09.2022 odobril kandidatu:

PETER LOMBERGAR

temo za doktorsko disertacijo z naslovom:

Numerično modeliranje temperature pri elektroporaciji ob prisotnosti pretokov tekočin

Numerical modeling of temperature distribution during electroporation based treatments in fluid flow conditions

Komisija za doktorski študij Univerze v Ljubljani je po pooblastilu Senata Univerze v Ljubljani temo potrdila na seji dne: 18.10.2022.

Senat Fakultete za elektrotehniko Univerze v Ljubljani je kandidatu na seji dne, 02.10.2025 priznal naslednje izvirne prispevke k znanosti:

1 Napredni numerični modeli pretočnih komor za obdelavo s pulzirajočim električnim poljem.

2 Numerični model nastajanja mehurčkov med srčno ablacijo s pulzirajočim električnim poljem.

3 Numerični modeli in vivo srčne ablacije s pulzirajočim električnim poljem v zdravih in infarktnih ventriklih.

Komisija za zagovor doktorske disertacije:

prof. dr. Boštjan Blažič, predsednik
prof. dr. Damijan Miklavčič, član
izr. prof. dr. Selma Čorović, član
prof. dr. sc. Ratko Magjarević, član

izr. prof. dr. Bor Kos, mentor

UNIVERZA V LJUBLJANI Fakulteta za elektrotehniko 2 LJUBLJANA

Dekan:
prof. dr. Marko Topič

UNIVERSITY OF LJUBLJANA | Faculty of Electrical Engineering

Tržaška cesta 25, POB 2999,
1000 Ljubljana, Slovenija
T: 01 476 84 11
dekanat@fe.uni-lj.si
www.fe.uni-lj.si

Spodaj podpisani študent, Peter Lombergar, vpisna številka 64170370, avtor pisnega zaključnega dela študija z naslovom: Numerično modeliranje temperature pri elektroporaciji ob prisotnosti pretokov tekočin,

IZJAVLJAM,

1.[1] a) da je pisno zaključno delo študija rezultat mojega samostojnega dela in da sem orodja umetne inteligence uporabljal odgovorno (predvsem s preverjanjem primarnih virov, brez vnašanja avtorsko zaščitenih del v orodja umetne inteligence, s kritičnim vrednotenjem rezultatov, ki so lahko pomanjkljivi, napačni ali neresnični) in sem izključno odgovoren za vsebino avtorskega dela, ki sem ga ustvaril;
   b) da je pisno zaključno delo študija rezultat lastnega dela več kandidatov in izpolnjuje pogoje, ki jih Statut UL določa za skupna zaključna dela študija ter je v zahtevanem deležu rezultat mojega samostojnega dela in da sem orodja umetne inteligence uporabljal odgovorno (predvsem s preverjanjem primarnih virov, brez vnašanja avtorsko zaščitenih del v orodja umetne inteligence, s kritičnim vrednotenjem rezultatov, ki so lahko pomanjkljivi, napačni ali neresnični) in sem izključno odgovoren za vsebino avtorskega dela, ki sem ga ustvaril;
2. da sem pridobil vsa potrebna dovoljenja za uporabo podatkov in avtorskih del v pisnem zaključnem delu študija in jih v pisnem zaključnem delu študija jasno označil;
3. da sem pri pripravi pisnega zaključnega dela študija ravnal v skladu z etičnimi načeli in, kjer je to potrebno, za raziskavo pridobil soglasje etične komisije;
4. da soglašam z uporabo elektronske oblike pisnega zaključnega dela študija za preverjanje podobnosti vsebine z drugimi deli s programsko opremo za preverjanje podobnosti vsebine, ki je povezana s študijskim informacijskim sistemom članice;
5. da na UL neodplačno, neizključno, prostorsko in časovno neomejeno prenašam pravico shranitve avtorskega dela v elektronski obliki, pravico reproduciranja ter pravico dajanja pisnega zaključnega dela študija na voljo javnosti na svetovnem spletu preko Repozitorija UL;
6. da sem od založnikov, na katere sem predhodno izključno prenesel materialne avtorske pravice na člankih, pridobil potrebna soglasja za vključitev člankov in elektronsko obliko disertacije. Soglasja UL omogočajo neodplačno, neizključno, prostorsko in časovno neomejeno hranjenje avtorskega dela v elektronski obliki in reproduciranje ter dajanje disertacije na voljo javnosti na svetovnem spletu preko Repozitorija UL.
7. da dovoljujem objavo svojih osebnih podatkov, ki so navedeni v pisnem zaključnem delu študija in tej izjavi, skupaj z objavo pisnega zaključnega dela študija.
8. da dovoljujem uporabo mojega rojstnega datuma v zapisu COBISS.

V: Ljubljani
Datum: 16. 10. 2025

Podpis študenta: Peter Lombergar

Digitally signed by Peter Lombergar
Date: 2025.10.20 12:50:46 +02'00'

[1] Obkrožite varianto a) ali b).

Zahvala

Najprej se iskreno zahvaljujem svojemu mentorju izr. prof. dr. Boru Kosu za vso pomoč, podporo, številne plodne razprave ter predvsem za potrpežljivost in mentorstvo med doktorskim študijem.

Iskrena zahvala gre tudi prof. dr. Damijanu Miklavčiču, ker mi je odprl vrata v svet znanosti, omogočil delo na zanimivih projektih ter nudil podporo in spodbudne besede.

Zahvaljujem se tudi vsem sodelavcem iz Laboratorija za biokibernetiko za prijetno in spodbudno delovno okolje, zanimive razprave in pomoč, kadar je bila potrebna.

Nenazadnje se iz srca zahvaljujem staršem Katji in Robertu, bratu Leonu ter moji ljubezni Zali, ki so mi ves čas stali ob strani, verjeli vame in me podpirali na tej poti.

Abstract

Electroporation is a biophysical phenomenon in which high-voltage electric pulses transiently increase cell membrane permeability. Depending on the electric field intensity and exposure duration, this process can result in either reversible or irreversible cell damage, giving it broad applications in food processing and medicine. In pulsed electric field (PEF) food treatments, irreversible electroporation is used to inactivate microorganisms while preserving food quality. In pulsed field ablation (PFA), it enables targeted destruction of cardiac tissue without the collateral thermal damage typical of conventional ablation methods. Although classified as "non-thermal", the use of high voltages and large numbers of pulses in these applications can cause significant ohmic heating. Understanding the interplay between electrical and thermal effects is therefore essential to improve the safety and efficacy of electroporation-based treatments. This dissertation addresses this challenge by developing and validating two numerical frameworks for PEF and PFA applications.

The first framework advances the modeling of continuous-flow PEF treatment chambers. A validated pulse-resolved numerical model was developed that improves upon conventional duty-cycle approximations by simulating each electrical pulse individually. This provides critical insights into transient temperature fluctuations that are otherwise missed, enabling more precise predictions of temperature dynamics. Additionally, a novel particle-level exposure analysis was introduced to evaluate the electrical and thermal doses experienced by individual particles along their trajectories. This analysis reveals the statistical distribution of exposures across the product, offering a direct measure of treatment homogeneity and a link to real-world process outcomes.

The second framework focuses on intracardiac PFA through two complementary studies. An *in vitro* study addressed the key safety concern of bubble formation by developing a numerical model of a bipolar PFA catheter, validated with high-speed camera recordings. The model accurately captured localized heating around sharp electrode edges, allowing it to distinguish between bubble formation from thermal mechanisms (boiling and degassing) and electrochemical reactions. This provided critical insights for designing safer pulse protocols and electrode geometries to minimize gas release. A subsequent comprehensive *in vivo* study modeled PFA in healthy and infarcted porcine ventricles, incorporating realistic ventricular geometry, cardiac tissue anisotropy, blood flow, and scar tissue distribution. By comparing

simulations with cardiac MRI, this work determined the *in vivo* lethal electric field threshold (LET) for ventricular myocardium for the first time. The models also confirmed the predominantly non-thermal nature of PFA, with less than 2% of the lesion volume attributed to thermal damage, and demonstrated that PFA can effectively ablate through dense scar tissue, a critical insight for treating ventricular arrhythmias.

In summary, this dissertation contributes two experimentally validated numerical frameworks that advance the understanding of electroporation-based treatments, providing valuable tools to improve the safety and efficacy of PEF and PFA technologies.

Keywords: Electroporation, Pulsed Electric Field (PEF) treatment, Pulsed Field Ablation (PFA), Numerical modeling, Cardiac ablation, Ohmic heating, Lethal electric field threshold, Thermal damage

Izvleček

Elektroporacija je biofizikalni pojav, pri katerem kratki visokonapetostni električni pulzi povzročijo prehodno povečanje prepustnosti celične membrane, kar lahko vodi v reverzibilno ali ireverzibilno poškodbo celic. Pogosto se uporablja v prehranski industriji kot metoda obdelave s pulzirajočim električnim poljem (PEF) in v medicini za ablacijo srčnega tkiva s pulzirajočim električnim poljem (PFA). Čeprav obe metodi veljata za »ne-termični«, lahko uporaba visokih napetosti in velikega števila pulzov povzroči znatno omsko segrevanje. Razumevanje medsebojnega vpliva električnih in toplotnih učinkov je zato ključno za izboljšanje varnosti in učinkovitosti tehnologij, ki temeljijo na elektroporaciji. Ta disertacija ta izziv naslavlja z razvojem in validacijo dveh sklopov numeričnih modelov za aplikacije PEF in PFA.

V prvem delu disertacije smo z namenom natančnejšega vpogleda v porazdelitev temperature med PEF obdelavo razvili in validirali numerični model, ki z eksplicitnim modeliranjem vsakega električnega pulza posebej nadgrajuje obstoječe pristope. S tem omogoča podroben vpogled v prehodna nihanja temperature v pretočni komori, ki jih obstoječi pristopi spregledajo, ter tako omogoča bolj natančne napovedi dviga temperature. Poleg tega smo razvili in predstavili novo analizo izpostavljenosti na nivoju delcev, ki ovrednoti celotno izpostavljenost vsakega delca ali celice električnemu polju in temperaturi vzdolž njihove poti. Takšna analiza omogoča neposredno merjenje homogenosti obdelave in nudi potencialno povezavo z dejanskimi izidi PEF obdelave, kot sta učinkovitost procesa in kakovost produkta.

Drugi del disertacije se osredotoča na znotrajsrčno PFA skozi dve dopolnjujoči se študiji. V okviru prve *in vitro* študije smo preučili pomemben varnostni vidik nastajanja mehurčkov med znotrajsrčno PFA z razvojem numeričnega modela bipolarnega PFA katetra, validiranega s posnetki hitre kamere. Model je natančno zajel lokalizirano segrevanje okoli ostrih robov elektrod in omogočil razlikovanje med termičnimi (vrenje in razplinjenje) ter elektrokemijskimi mehanizmi nastajanja mehurčkov. Pridobljena spoznanja so ključna za načrtovanje varnejših pulznih protokolov in geometrij elektrod. V okviru druge obsežne *in vivo* študije pa smo razvili modele PFA v zdravih in infarktnih prašičjih ventriklih z upoštevanjem realistične geometrije, anizotropije tkiva, pretoka krvi in brazgotinastega tkiva. S primerjavo simulacij in slik srca z magnetno resonanco smo prvič določili *in vivo* prag elektroporacije za srčno mišico. Modeli so potrdili pretežno netermično naravo PFA, saj je bil delež toplotno poškodovanega tkiva manjši

od 2 %. Prav tako so pokazali, da PFA lahko učinkovito deluje skozi gosto brazgotinasto tkivo, kar je klinično pomemben vpogled za zdravljenje ventrikularnih aritmij.

Če povzamemo, ta disertacija prispeva dva eksperimentalno potrjena sklopa numeričnih modelov, ki izboljšujeta razumevanje elektroporacijskih tehnologij ter zagotavljata pomembna orodja za izboljšanje varnosti in učinkovitosti PEF in PFA tehnologij.

Ključne besede: Elektroporacija, Obdelava s pulzirajočim električnim poljem (PEF), Ablacija s pulzirajočim električnim poljem (PFA), Numerično modeliranje, Srčna ablacija, Ohmsko segrevanje, Prag elektroporacije, Toplotne poškodbe

Table of contents

ABSTRACT **I**

IZVLEČEK **III**

RAZŠIRJEN POVZETEK V SLOVENŠČINI **IX**

I. Uvod ix

I.i. Elektroporacija ix

I.ii. Elektroporacija v prehranski industriji in numerično modeliranje ix

I.iii. Ablacija srčnega tkiva z ireverzibilno elektroporacijo in numerično modeliranje x

I.iv. Namen doktorske disertacije xi

II. Napredni modeli pretočnih komor za obdelavo s pulzirajočim električnim poljem xiii

III. Model nastajanja mehurčkov med srčno ablacijo s pulzirajočim električnim poljem xvii

IV. Model in vivo ablacije s pulzirajočim električnim poljem v zdravem in infarktnem prašičjem ventriklu xix

V. Izvirni prispevki k znanosti xxi

1. INTRODUCTION **1**

1.1. Electroporation - the phenomenon 1

1.2. Numerical modeling of pulsed electric field treatment chambers 1

1.3. Numerical modeling of pulsed field ablation of cardiac tissue 2

1.4. Aims of the dissertation 3

2. ADVANCED MODELS OF CONTINUOUS-FLOW PULSED ELECTRIC FIELD (PEF) TREATMENT CHAMBERS **7**

2.1. Background 7

2.2. Methods 8

2.2.1. Experimental setup and measurements 8

2.2.2. PEF Treatment chamber geometries 12

2.2.3. Pulse protocols and PEF treatment parameters 15

2.2.4. Pulse-resolved numerical model of continuous flow PEF treatment chamber 17

2.2.5. Comparison of pulse-resolved model with the duty cycle model 23

2.2.6. Particle-level exposure to electric field and temperature 24
2.3. Results 26
2.3.1. Calculated temperature distribution in PEF treatment chambers 26
2.3.2. Pulse-resolved model vs experiments 28
2.3.3. Comparing pulse-resolved against duty cycle model 34
2.3.4. Particle-level exposure to electric field and temperature 38
2.4. Discussion 44
2.4.1. Pulse-resolved model validation 44
2.4.2. Pulse resolved vs duty cycle modeling approach 44
2.4.3. Particle-level exposure to electric field and temperature 46
2.4.4. Limitations 47
2.5. Conclusions 48

3. MODEL OF BUBBLE FORMATION DURING INTRACARDIAC PULSED FIELD ABLATION (PFA) 51

3.1. Background 51
3.2. Methods 52
3.2.1. Pulse protocols 52
3.2.2. High-speed camera experiments 54
3.2.3. Numerical model 56
3.3. Results 59
3.3.1. Model output 59
3.3.2. Numerical model vs high-speed camera experiments 61
3.4. Discussion 68
3.4.1. Monophasic vs Biphasic pulse protocols 68
3.4.2. Limitations 69
3.5. Conclusions 69

4. MODEL OF *IN VIVO* INTRACARDIAC PULSED FIELD ABLATION (PFA) IN HEALTHY AND INFARCTED SWINE VENTRICLES 71

4.1. Background 71
4.2. Methods 72
4.2.1. Numerical model of PFA in healthy left ventricle 72

4.2.2. Numerical model of PFA in infarcted left ventricle 82
4.3. Results 83
4.3.1. Electric field distribution and Lethal Electric Field Threshold 83
4.3.2. Temperature increases during PFA and thermal damage 86
4.3.3. Ablation through fibrotic scar 89
4.4. Discussion 91
4.4.1. Lethal electric field threshold 91
4.4.2. Electric field in blood 91
4.4.3. Thermal damage 92
4.4.4. PFA in infarcted LV 92
4.4.5. Limitations 92
4.5. Conclusions 93
5. GENERAL CONCLUSIONS 95
6. ORIGINAL CONTRIBUTIONS TO SCIENCE 99
7. REFERENCES 101

Razširjen povzetek v slovenščini

I. Uvod

I.i. Elektroporacija

Izpostavitev celic ali tkiva kratkim električnim pulzom z dovolj visoko amplitudo, da dosežemo prehodno povečanje prepustnosti celične membrane, imenujemo elektroporacija [1]. Če je izpostavitev membrane električnemu polju dovolj kratka in ne preveč intenzivna, obnovitev membrane pa dovolj hitra, da celica ostane živa, je elektroporacija reverzibilna, v nasprotnem primeru pa pretirana izpostavljenost električnemu polju povzroči celično smrt in je elektroporacija ireverzibilna [2].

Pomembna lastnost elektroporacije je njena univerzalnost, saj lahko do nje pride pri vseh vrstah celic in v vseh različnih celičnih konfiguracijah [3]. Prav zaradi te univerzalnosti se elektroporacija danes uporablja na različnih področjih: v medicini [4], [5], biotehnologiji [6], okoljevarstvu [7], [8] in prehranski industriji [9], [10].

I.ii. Elektroporacija v prehranski industriji in numerično modeliranje

Na področju prehranske industrije se namesto izraza elektroporacija pogosto uporablja izraz obdelava s pulzirajočim električnim poljem (angl. **PEF** – Pulsed Electric Field treatment). Ena najpomembnejših aplikacij PEF obdelave v prehranski industriji je deaktivacija mikrobov preko mehanizma ireverzibilne elektroporacije (sokovi [11], mleko [12], vino [13]). PEF obdelava velja za ne-termično metodo konzerviranja hrane, zato je privlačnejša od običajnih termičnih metod, saj bolje ohrani senzorične, prehranske in funkcionalne lastnosti hrane [14], [15].

Ključna komponenta sistema za PEF obdelavo je elektroporacijska komora (angl. treatment chamber), kjer je obdelovanec izpostavljen električnim pulzom. Sestavljena je iz vsaj dveh elektrod in vmesnega izolacijskega materiala v različnih geometrijskih konfiguracijah, ki privedejo do različnih porazdelitev električnega polja v komori. Ločimo statične elektroporacijske komore (angl. static treatment chamber) in pretočne elektroporacijske komore (angl. continuous-flow treatment chamber). Prve so v prvi vrsti namenjene laboratorijskim poskusom, pretočne komore pa je mogoče enostavno vključiti tudi v industrijske procese. Najbolj uporabljene oblike pretočnih komor so linearna (angl. parallel plate), obročna (angl.

colinear) in koaksialna (angl. coaxial), pri čemer ima vsaka svoje prednosti in slabosti pri PEF obdelavi [9], [16].

Numerične simulacije na področju PEF lahko po Gerlach et al. [17] razdelimo v dve skupini. Prva skupina se osredotoča na simulacije električnega polja v različnih pretočnih komorah, pri čemer ne upošteva pretoka tekočine in segrevanja. Cilj teh simulacij je izboljšati homogenost električnega polja v pretočnih komorah [18], [19]. Druga skupina simulacij, ki je bolj relevantna za predlagano disertacijo, pa se osredotoča na sklopljene simulacije električnega polja, pretoka tekočine in segrevanja [20], [21], [22], [23], [24], [25]. Namen teh simulacij je preučiti, kako ohmsko gretje obdelovanca zaradi električnega toka skupaj s prenosom toplote s konvekcijo in prevajanjem določa porazdelitev temperature v pretočni komori. V večini obstoječih del je uveljavljen pristop »duty cycle« metoda, pri kateri na elektrode predpišemo konstantno napetost kot robni pogoj, stacionarni vir ohmskega gretja pa pomnožimo z delovnim ciklom pulznega protokola (angl. duty factor), da upoštevamo pulzno dovajanje energije. Čeprav ta metoda skrajša čas računanja, ne daje informacij o temperaturi in električnem polju v pretočni komori med posameznimi električnimi pulzi.

Boljše poznavanje električnega polja in temperaturnega profila v pretočnih komorah med PEF obdelavo je pomembno, saj lahko lokalni dvigi temperature znotraj pretočne komore (kot posledica nehomogenosti električnega polja ali pretoka tekočine) vplivajo na kakovost hrane. Če je dvig temperature prevelik, lahko PEF tehnologija izgubi svoje prednosti kot metoda ne-termične obdelave hrane.

I.iii. Ablacija srčnega tkiva z ireverzibilno elektroporacijo in numerično modeliranje

Na področju medicine je ena najbolj obetavnih aplikacij ireverzibilne elektroporacije ablacija srčnega tkiva, ki jo imenujemo tudi ablacija s pulzirajočim električnim poljem (angl. **PFA** – Pulsed Field Ablation). Glavna prednost PFA je ablacija z ne-termično metodo, ki ohranja živce, glavne krvne žile in druga občutljiva tkiva [26], [27].

Ablacija srčnega tkiva se uporablja za zdravljenje atrijskega plapolanja, atrijske fibrilacije in ventrikularnih aritmij. Cilj ablacije je uničiti aritmogeno tkivo in ustvariti trajne poškodbe tkiva (t.i. lezije), ki zajemajo celotno debelino tkiva in so med seboj povezane [28]. PFA se uveljalvla kot nova ne-termična tehnika za srčno ablacijo, ki velja za varnejšo v primerjavi s tehnikami termične ablacije, kot je radiofrekvenčna ablacija (angl. **RFA** – Radio Frequency Ablation) [17]. PFA se izvaja z uporabo miniaturnih katetrov različnih oblik in razporeditev elektrod

(monopolarna, bipolarna), ki povzročajo različne globine lezij. Glede na debelino ciljnega srčnega tkiva (pljučna vena ~ 2 mm, stena levega prekata ~ 10 mm), so nekatere oblike katetrov in razporeditve elektrod bolj primerne kot druge, pri čemer točkasti katetri z monopolarnimi elektrodami povzročijo najgloblje lezije. Pri monopolarni razporeditvi elektrod so aktivne elektrode nameščene blizu ciljnega tkiva s povratno potjo do oddaljene disperzivne (povratne) elektrode, ki je lahko druga elektroda ali niz elektrod, nameščenih kjerkoli drugje v srcu ali venskem ožilju [29].

Čeprav je še v začetni fazi, se je literatura o numeričnem modeliranju PFA v zadnjih letih hitro razširila. Večina študij se osredotoča na modeliranje porazdelitve električnega polja za napoved velikosti lezije [30], [31], [32], [33], [34], medtem ko nekatere že modelirajo tudi dvig temperature med PFA in možnost toplotnih poškodb [35], [36].

Poleg tega obstaja obsežna literatura, o modeliranju segrevanja in možnih toplotnih poškodb med elektroporacijo tkiva [37], [38], [39], [40]. Vendar ti modeli niso bili razviti za srčna tkiva, zato ne vključujejo hlajenja tkiva in elektrod zaradi pretoka krvi ter morebitne irigacije katetra, kar oboje vpliva na temperature med PFA. Za raziskovanje hlajenja tkiva in elektrod s pretokom krvi in irigacijo katetra je lahko v pomoč literatura o modeliranju dviga temperature med RFA [41], [42], [43], [44].

Cilj PFA je doseči zadostno jakost električnega polja v ciljnem območju, da dosežemo želeno globino lezije, z minimalnim dvigom temperature (minimalnim tveganjem toplotnih poškodb). Za dosego tega cilja je potrebno podrobno poznavanje temperature in porazdelitve električnega polja med PFA. Zato, je nadaljnji razvoj numeričnih modelov za PFA pomemben za pomoč pri optimizaciji varnosti in učinkovitosti ablacije.

I.iv. Namen doktorske disertacije

Ireverzibilna elektroporacija se pogosto uporablja kot netermična alternativa termičnim metodam obdelave hrane ali ablacije. Glavna prednost elektroporacije v primerjavi s termičnimi metodami je mehanizem celične smrti, ki pri elektroporaciji ni termične narave, s čimer naj bi se izognili morebitnim stranskim učinkom termičnih metod. Vendar to ni nujno res, saj se za dosego ireverzibilne elektroporacije pogosto uporabljajo protokoli z visoko napetostjo in velikim številom pulzov, ki lahko povzročijo znatno omsko gretje in dvig temperature v tkivu ali obdelovani hrani. Pri obdelavi hrane lahko visoke temperature vplivajo na njeno kakovost, pri ablaciji srčnega tkiva pa lahko bistveno vplivajo na varnost postopka. Razumevanje

medsebojnega vpliva električnih in toplotnih učinkov je zato ključno za izboljšanje varnosti in učinkovitosti tehnologij, ki temeljijo na elektroporaciji. Temeljni cilj te disertacije je nasloviti ta izziv z razvojem in validacijo kompleksnih numeričnih modelov, ki omogočajo natančno napoved porazdelitve električnega polja in temperature ter zagotavljajo pomembne informacije o parametrih, ki vplivajo na varnost in učinkovitost obdelave s PEF in PFA.

V skladu s tem sta bila opredeljena naslednja dva cilja:

Prvi cilj je bil izboljšati numerično modeliranje pretočnih komor za obdelavo s PEF. To smo dosegli z dvema prispevkoma. Najprej smo razvili in validirali časovno odvisen numerični model pretočnih komor za PEF obdelavo, ki nadgrajuje obstoječe modele segrevanja v komori, z eksplicitnim modeliranjem vsakega električnega pulza posebej. Nov model omogoča podroben vpogled v prehodna nihanja temperature na različnih lokacijah znotraj komore, ki jih obstoječi pristopi zanemarjajo, in tako omogoča natančnejše napovedi dinamike temperature. Poleg tega smo razvili in predstavili analizo, ki ovrednoti celotno izpostavljenost vsakega delca ali celice električnemu polju in temperaturi vzdolž njihove poti v komori, s čimer določimo ključne metrike izpostavljenosti in njihovo statistično porazdelitev za celoten produkt. Ta analiza omogoča neposredno vrednotenje homogenosti obdelave in nudi potencialno povezavo z dejanskimi izidi PEF obdelave, kot sta učinkovitost procesa in kakovost produkta, ter tako ponuja celovitejše in zmogljivejše orodje za optimizacijo PEF procesa..

Drugi cilj je bil razviti nove numerične modele za napovedovanje porazdelitve električnega polja in temperature med srčno ablacijo s PFA, da bi pridobili ključne vpoglede za izboljšanje varnosti in učinkovitosti kliničnega postopka. Ta cilj smo naslovili z dvema ločenima, a dopolnjujočima se študijama. Prva je bila *in vitro* študija, ki je raziskala mehanizme nastajanja mehurčkov med PFA. V okviru te študije je bil razvit numerični model bipolarnega PFA katetra v fiziološki raztopini, ki omogoča natančen izračun segrevanja okoli ostrih robov elektrod in termičnih mehanizmov nastajanja mehurčkov (razplinjevanje in vrenje) ter tako omogoča načrtovanje varnejših pulznih protokolov in geometrij elektrod. Druga je bila obsežna *in vivo* študija znotrajsrčne PFA v zdravih in infarktnih prašičjih ventriklih. V okviru te študije smo razvili podrobne modele *in vivo* PFA v ventriklih, s katerimi smo določili prag elektroporacije za srčno tkivo v ventriklih, pridobili vpogled v dvig temperature med dovajanjem električnih pulzov in morebitne toplotne poškodbe tkiva ter raziskali klinično pomembno vprašanje, ali lahko PFA povzroči poškodbe ob prisotnosti brazgotinastega tkiva.

II. Napredni modeli pretočnih komor za obdelavo s pulzirajočim električnim poljem

Poznavanje dviga temperature v pretočni komori med obdelavo s pulzirajočim električnim poljem (PEF) je pomembno, saj lahko lokalni dvigi temperature znotraj pretočne komore zaradi nehomogenosti električnega polja ali pretoka tekočine vplivajo na kakovost produkta in življenjsko dobo naprav. V večini obstoječih del je uveljavljen pristop »duty cycle« metoda, pri kateri na elektrode predpišemo konstantno napetost kot robni pogoj, stacionarni vir ohmskega gretja pa pomnožimo z delovnim ciklom pulznega protokola (angl. duty factor), da upoštevamo pulzno dovajanje energije. Čeprav ta metoda skrajša čas računanja, ne daje informacij o dogajanju v pretočni komori med vsakim posameznim električnim pulzom.

V prvem delu te študije smo zato razvili in validirali časovno odvisen model, ki z modeliranjem vsakega pulza posebej natančneje opiše dvig temperature v pretočnih komorah. V programskem okolju COMSOL smo izdelali sklopljen model, ki vključuje pretok tekočin, prenos toplote in časovno odvisno električno polje. Model smo uspešno validirali z eksperimentalnimi meritvami temperature in električnega toka v linearni in obročni pretočni komori za različne pulzne protokole in pretoke tekočin.

Ključna prednost novega časovno odvisnega pristopa je, da lahko razkrije prehodna nihanja temperature med aplikacijo električnih pulzov, ki jih obstoječi modeli ne upoštevajo. Primerjavo med validiranim časovno odvisnim modelom in »duty cycle« metodo, za linearno in obročno pretočno komoro lahko vidimo na Slika 0-1. Kot je prikazano na Slika 0-1, »duty cycle« metoda dobro opiše povprečne temperature na različnih lokacijah v komori, vendar popolnoma zgladi prehodna temperaturna nihanja, ki so prisotna med aplikacijo električnih pulzov. Čeprav so ta nihanja za naše eksperimentalno validirane protokole relativno majhna (< 1°C), zaradi nizkih dovedenih energij, lahko razlika med modeloma postane pomembna pri protokolih z višjimi dovedenimi energijami, ki se uporabljajo za PEF obdelavo v prehranski industriji. Z našim časovno odvisnim modelom smo zato izračunali dvig temperature tudi za hipotetični "visokoenergijski" PEF protokol, ki je povzročil znatna temperaturna nihanja v vročih točkah z razponom več kot 10 °C. V tem industrijsko bolj relevantnem primeru je »duty cycle« metoda podcenila najvišjo temperaturo za znatnih 8 °C. Takšna razlika je pomembna, saj lahko povišane temperature privedejo do toplotnih poškodb obdelanega produkta in povečajo tveganje za propadanje elektrod ter iskrenje. Zato pri PEF protokolih, kjer se

pričakujejo velika temperaturna nihanja, časovno odvisen pristop zagotavlja natančnejšo oceno temperature v pretočni komori in nudi boljše orodje za optimizacijo procesa, nadzor kakovosti ter zagotavljanje varnosti opreme.

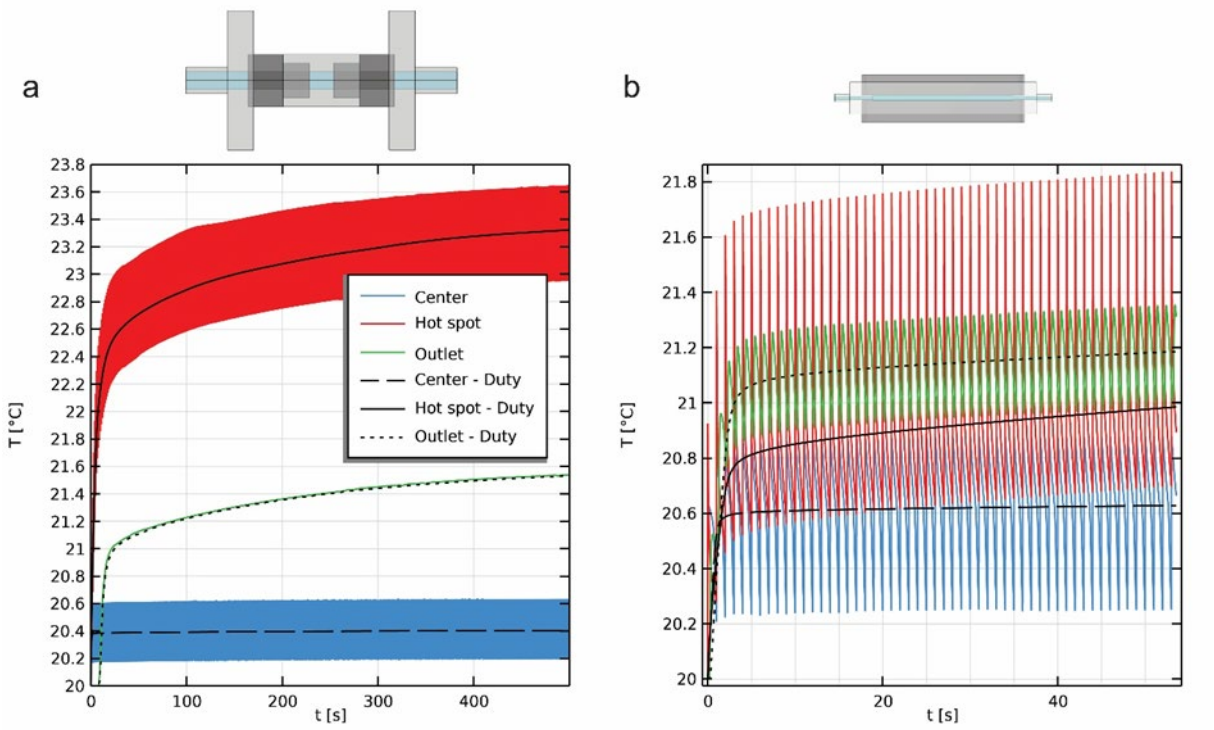

Slika 0-1: Primerjava časovno odvisne metode z "duty cycle" metodo. Temperature, izračunane na treh različnih lokacijah (center, vroča točka, izhod) v (a) obročni in (b) linearni pretočni komori. Pulzni protokol: 100 µs, 1 Hz, F = 20 ml/min, T_i = 20 °C in U = 1000 V (linearna komora) in U = 4000 V (obročna komora). Slika je prirejena iz [45].

Numerični modeli električnega polja in temperature v pretočnih komorah omogočajo vpogled v prostorske in časovne porazdelitve, ne odgovorijo pa na vprašanje, kaj na svoji poti skozi komoro dejansko »doživi« posamezen delec ali celica. Med PEF obdelavo delci oziroma celice potujejo po različnih tokovnicah z različnimi hitrostmi, zato so izpostavljeni zelo različnim električnim in toplotnim obremenitvam (različno število prejetih pulzov, različne najvišje dosežene temperature ipd.).

V drugem delu te študije smo razvili in predstavili analizo, ki ovrednoti celotno izpostavljenost posameznega delca ali celice električnemu polju in temperaturi vzdolž njegove poti skozi komoro. Analizo izpostavljenosti smo uvedli v COMSOL-u kot razširitev časovno odvisnega modela PEF pretočnih komor in tudi »duty-cycle« modela. Najprej smo na podlagi študije pretoka izračunali trajektorije delcev. Nato smo vzdolž teh trajektorij z enakimi časovnimi

koraki kot v sklopljeni elektro-termični simulaciji, numerično interpolirali trenutne vrednosti električnega polja in temperature ter za vsak delec zgradili celoten časovni potek izpostavljenosti električnemu polju in temperaturi. Na Slika 0-2 lahko vidimo, izpostavljenost različnih delcev temperaturi in električnemu polju. Za preglednost smo prikazali pet delcev z reprezentativnimi tokovnicami, izbranimi po percentilih volumetričnega pretoka (0, 50, 75, 90 in 99 %). Kot lahko vidimo, delci na različnih tokovnicah prejmejo opazno različne električne in toplotne obremenitve.

Na podlagi zgodovine izpostavljenosti lahko za vsak delec določimo ključne metrike izpostavljenosti (npr. skupni čas izpostavljenosti nad izbranim pragom polja in najvišjo doseženo temperaturo) ter njihovo porazdelitev za celoten produkt. Takšna analiza omogoča neposredno merjenje homogenosti obdelave in vzpostavlja povezavo z dejanskimi izidi PEF procesa (npr. učinkovitost mikrobne inaktivacije, toplotne poškodbe produkta), zato predstavlja uporabno orodje za optimizacijo geometrije komor, pretokov in pulznih protokolov.

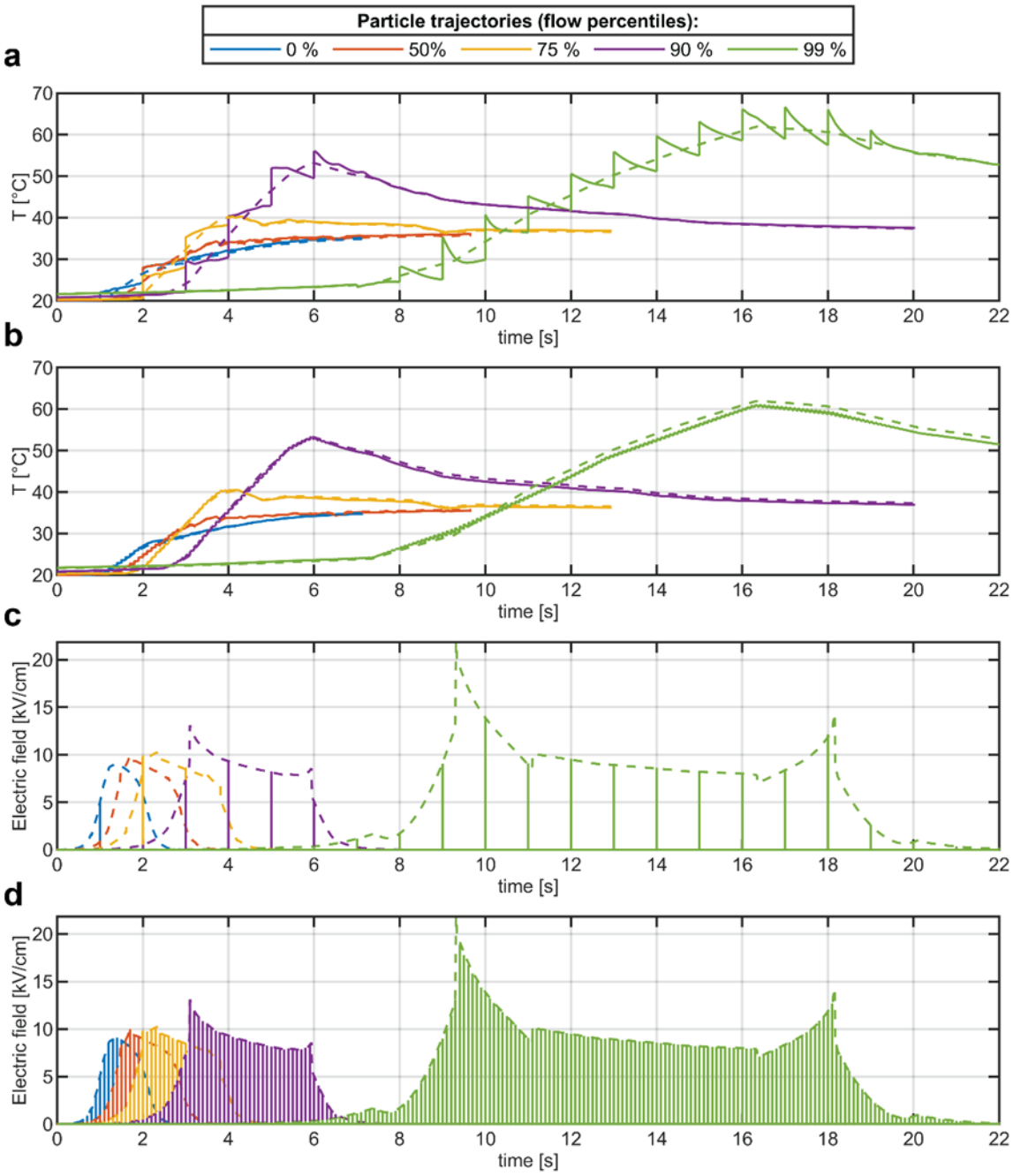

Slika 0-2: Izpostavljenost reprezentativnih delcev temperaturi (zgornja dva grafa) in električnemu polju (spodnja dva grafa) med pretokom skozi PEF komoro. Prikazani so rezultati za pet trajektorij, ki ustrezajo percentilom volumetričnega pretoka (0 %, 50 %, 75 %, 90 % in 99 %) za dva pulzna protokola: 100 µs pri 1 Hz in 10 µs pri 10 Hz. Polne črte predstavljajo časovno odvisno metodo, črtkane črte pa "duty cycle" metodo. Višji percentili predstavljajo počasneje gibajoče se delce, ki so bližje steni komore.

III. Model nastajanja mehurčkov med srčno ablacijo s pulzirajočim električnim poljem

Z naraščajočo uporabo ablacije s pulzirajočim električnim poljem (PFA) za zdravljenje srčnih aritmij postaja razumevanje in obvladovanje morebitnih varnostnih tveganj ključnega pomena. Ena pomembnih skrbi je sproščanje plinskih mehurčkov med postopkom, ki nastanejo na stiku med katetrom in krvjo ter se sprostijo v krvni obtok in organe, kot so ledvice, pljuča ali možgani, kar lahko povzroči zaporo koronarnih arterij ali možgansko kap.

Nastanek mehurčkov je lahko posledica treh mehanizmov: **vrenje** – sproščanje plina v obliki vodne pare, **razplinjenje** – sproščanje plina zaradi manjše topnosti plina pri povišani temperaturi medija, in **elektroliza** – sproščanje plina zaradi elektrokemijskih reakcij na elektrodah.

Za raziskovanje nastanka mehurčkov je bila izvedena *in vitro* študija, ki je združila numerično modeliranje in eksperimente s hitro kamero (10.000 sličic na sekundo) za različne pulzne protokole. Geometrija numeričnega modela je posnemala eksperimente s hitro kamero in je vključevala model bipolarnega PFA katetra v fiziološki raztopini, ki je posnemala električno prevodnost krvi. Cilj modela je bil čim bolj natančen izračun segrevanja tekočine ob dovajanju električnih pulzov in določitev volumna mehurčkov kot posledice razplinjenja in vrenja.

S pomočjo numeričnega modela smo izračunali, da do največjega segrevanja tekočine pride ob robovih elektrod, kar se je dobro ujemalo z lokacijo pojava mehurčkov na posnetkih s hitro kamero. Z modelom smo prav tako pravilno napovedali začetek pojava mehurčkov, povezanih z vrenjem, na posnetkih s hitro kamero. Na Slika 0-3, lahko vidimo primerjavo modela in posnetkov za bifazni pulznih protokol z visokim delovnim ciklom. Pri tem protokolu kratko, a intenzivno dovajanje električne energije povzroči hitro segrevanje na robovih elektrod, kjer so mehurčki jasno vidni. Izračuni kažejo, da je volumen mehurčkov zaradi vrenja dva reda velikosti večji od razplinjenja, kar se ujema tudi s hitrim kolapsom mehurčkov na posnetku.

S primerjavo različnih protokolov je študija pokazala, da pri visokofrekvenčnih bifaznih protokolih mehurčki nastajajo pretežno zaradi vrenja. Pri monofaznih protokolih pa velik delež mehurčkov nastane zaradi elektrokemijskih reakcij. Mehurčki, nastali zaradi vrenja, se hitro sesedejo, medtem ko so mehurčki ki nastanejo z elektrolizo, bolj obstojni. Te ugotovitve kažejo, da so za zmanjšanje sproščanja plina med srčno ablacijo najprimernejši bifazni pulzni protokoli z nizkim delovnim ciklom (kratki pulzi in dolge pavze med pulzi), ki preprečujejo prekomerno

segrevanje, pri zasnovi geometrije elektrod pa se je potrebno izogibati ostrim robovom, da se zmanjša visoka lokalna gostota toka in segrevanje ob robu elektrod.

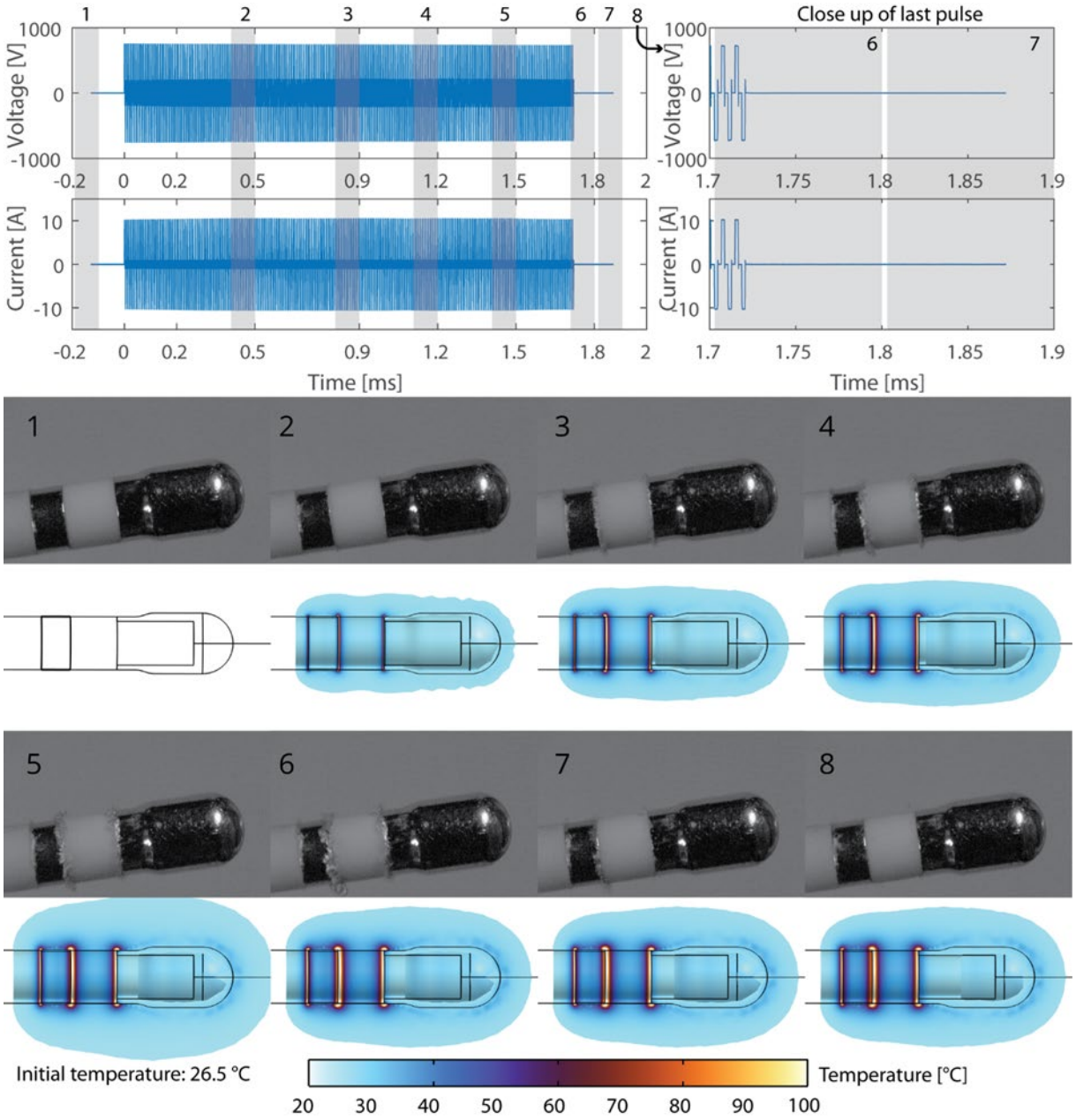

Slika 0-3: Bifazni protokol z visokim delovnim ciklom (2-2-2-500) pri sobni temperaturi. Zgornja grafa prikazujeta izmerjeno napetost in električni tok na osciloskopu med dovajanjem električnih pulzov. Slike so prikazane v dveh vrsticah prva vrstica prikazuje sličice iz posnetkov s hitro kamero v različnih časovnih točkah, pod vsako sličico pa je prikazana ustrezna napovedana porazdelitev temperature iz numeričnega modela za isto časovno točko, pri čemer je prikazano samo območje kjer se temperatura poveča vsaj za 1°. Številka slike ustreza časovni točki, označeni na meritvah toka in napetosti, trajanje izpostavljenosti vsakega posnetka je označeno s sivo obarvanim območjem. Slika je prirejena iz [46].

IV. Model *in vivo* ablacije s pulzirajočim električnim poljem v zdravem in infarktnem prašičjem ventriklu

Širitev uporabe ablacije s pulzirajočim električnim polje (PFA) iz zdravljenja atrijskih aritmij na zdravljenje aritmij v ventriklih prinaša nove izzive, vključno s potrebo po ustvarjanju globljih lezij v debelejših stenah ventriklov ter učinkovito ablacijo ob prisotnosti brazgotinastega tkiva.

Za podrobno preučitev teh izzivov je bila izvedena obširna študija, ki je povezala *in vivo* poizkuse na prašičjih srcih ter napredne numerične modele. In vivo del raziskave je bil izveden v Sunnybrook centru v Torontu, kjer je bila PFA aplicirana tako v zdrave kot v kronično infarktne prašičje ventrikle, lezije pa so bile določene s slikanjem srca z magnetno resonanco (MR) in histološko analizo. Za podporo *in vivo* delu smo razvili podrobne numerične modele. Za zdrave ventrikle je bil uporabljen shematski model za izračun porazdelitve električnega polja in temperature, ki je vključeval idealizirano geometrijo levega in desnega ventrikla, anizotropijo srčnega tkiva ter pretok krvi. Z modelom smo nato določili prag elektroporacije z iskanjem vrednosti električnega polja, pri kateri se je izračunani volumen lezije ujemal z volumnom, izmerjenim na kontrastnih MR slikah. Pri simulaciji PFA v infarktnih ventriklih je bil glavni cilj izračun razporeditve električnega polja v srčnem tkivu ob prisotnosti brazgotinastega tkiva, zato smo za model uporabili eksaktno geometrijo ventrikla, specifično za posamezno žival, in porazdelitev brazgotinskega tkiva, pridobljeno s kontrastnimi MR slikami.

V študiji smo prvič določili *in vivo* prag elektroporacije za srčno tkivo v ventriklih. Na Slika 0-4 lahko vidimo izračune praga elektroporacije za različno število dovedenih vlakov pulzov in različne časovne točke po ablaciji, ob katerih smo določili volumen lezij. Rezultati kažejo, da je prag elektroporacije odvisen od števila vlakov pulzov in od časa, ko po ablaciji določimo/izmerimo lezijo na MR slikah. Na primer 7 dni po ablaciji je izračunana mediana praga elektroporacije znašala od 725 V/cm za en pulzni vlak do 394 V/cm za 16 pulznih vlakov. Te ugotovitve zagotavljajo pomembne podatke za načrtovanje in napovedovanje izidov PFA pri zdravljenju ventrikularnih aritmij.

S pomočjo modela smo potrdili tudi netermično naravo PFA; za najvišji odmerek (16 vlakov) je bilo izračunano, da toplotne poškodbe predstavljajo manj kot 2 % celotnega volumna lezije, kar se skladno z odsotnostjo termičnega odtisa na MR slikah.

Pomembno je tudi, da sta tako numerični model kot kasnejša histološka analiza pokazala, da lahko PFA učinkovito prodre in ustvari transmuralne lezije skozi gosto poinfarktno brazgotino, kar je ključno za klinični vpogled v zdravljenje aritmij v infarktnih srcih.

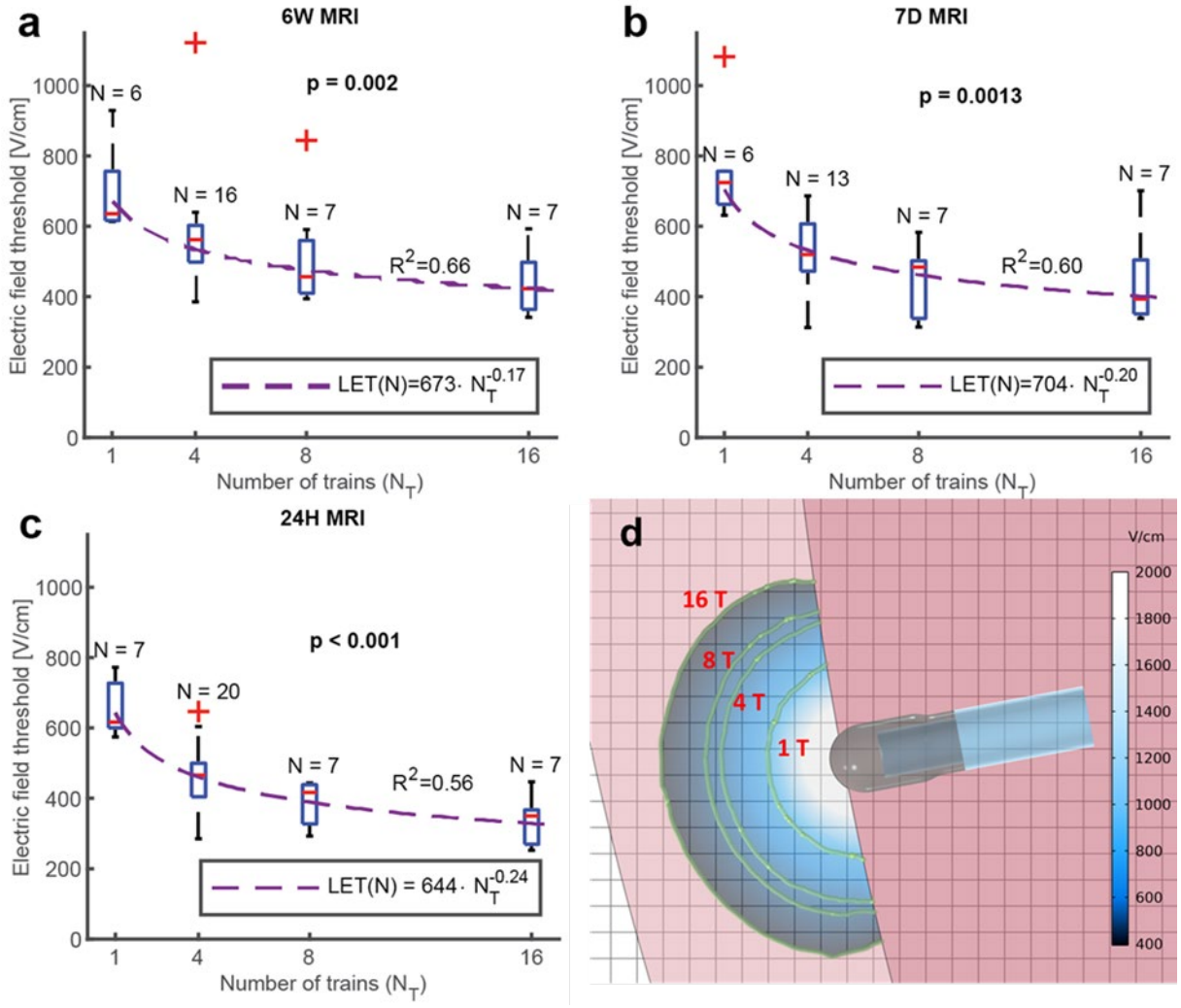

Slika 0-4: Prag elektroporacije (angl. LET – lethal electric field threshold) je bil izračunan s primerjavo numeričnega modela in volumna lezij, določenega s kontrastnimi MR slikami za različne časovne točke po ablaciji ter različno število dovedenih vlakov pulzov: a) po 6 tednih je bila mediana LET 636, 562, 457 in 423 V/cm za 1, 4, 8 in 16 vlakov; b) po 7 dneh je bila mediana LET 725, 520, 484 in 394 V/cm za 1, 4, 8 in 16 vlakov; c) po 24 urah je bila mediana LET 617, 466, 417 in 350 V/cm za 1, 4, 8 in 16 vlakov. d) Izračunana porazdelitev električnega polja v srčnem tkivu v primeru srednje posteriorne lezije je prikazana z zelenimi krivuljami, ki predstavljajo mediano praga LET, izračunanega za lezije 7 dni po ablaciji za različno število vlakov, kot je označeno na posameznih konturah. Slika je prirejena iz [47].

V. Izvirni prispevki k znanosti

Napredni numerični modeli pretočnih komor za obdelavo s pulzirajočim električnim poljem (PEF)

Natančno modeliranje porazdelitve električnega polja in temperature je pomembno orodje pri optimizaciji obdelave s pulzirajočim električnim poljem (PEF). V okviru tega prispevka smo razvili in validirali časovno odvisen numerični model pretočnih komor za PEF obdelavo, ki nadgradi obstoječe modele segrevanja v komori, ki uporabljajo t.i. »duty cycle« metodo, z eksplicitnim modeliranjem vsakega električnega pulza posebej. Nov pristop omogoča podroben vpogled v prehodna nihanja temperature na različnih lokacijah znotraj komore, ki jih obstoječi pristopi zanemarijo, in tako omogoča bolj natančne napovedi dinamike temperature.

Poleg tega smo razvili in predstavili tudi analizo, ki ovrednoti celotno izpostavljenost vsakega delca ali celice električnemu polju in temperaturi vzdolž njihove poti v komori, s čimer določimo ključne metrike izpostavljenosti in njihovo statistično porazdelitev za celoten produkt. Takšna analiza omogoča neposredno vrednotenje homogenosti obdelave in nudi potencialno povezavo z dejanskimi izidi PEF obdelave, kot sta učinkovitost procesa in kakovost produkta, ter tako ponuja celovitejše in zmogljivejše ogrodje za optimizacijo PEF procesov.

Numerični model nastajanja mehurčkov med srčno ablacijo s pulzirajočim električnim poljem (PFA)

V okviru tega prispevka smo izvedli *in vitro* študijo, ki je raziskala mehanizme nastajanja mehurčkov med znotrajsrčno ablacijo s pulzirajočim električnim poljem (PFA). V tej študiji je bil razvit numerični model bipolarnega PFA katetra v fiziološki raztopini, ki je bil validiran s posnetki s hitro kamero. Model omogoča natančen izračun segrevanja okoli ostrih robov elektrod in termičnih mehanizmov nastajanja mehurčkov (razplinjevanje in vrenje). Študija je pokazala, da pri monofaznih pulznih protokolih prevladuje elektrokemično nastajanje mehurčkov, medtem ko pri visokofrekvenčnih bifaznih protokolih prevladuje nastajanje mehurčkov zaradi vrenja tekočine. Rezultati so pokazali, da so za zmanjšanje sproščanja plina med srčno ablacijo optimalni bifazni pulzni protokoli s kratkimi pulzi in dolgimi pavzami med pulzi, pri zasnovi elektrod pa se je treba izogibati ostrim robovom, da zmanjšamo visoko lokalno gostoto električnega toka in segrevanje ob robovih elektrod.

Numerični modeli *in vivo* srčne ablacije s pulzirajočim električnim poljem (PFA) v zdravih in infarktnih ventriklih

Razvili smo podrobne numerične modele za *in vivo* ablacijo s pulzirajočim električnim poljem (PFA) v zdravih in infarktnih ventriklih, pri čemer smo upoštevali natančno geometrijo ventriklov, anizotropijo srčnega tkiva, pretok krvi in porazdelitev brazgotinskega tkiva. Modeli so omogočili določitev *in vivo* praga elektroporacije za srčno tkivo in vpogled v segrevanje med dovajanjem električnih pulzov in morebitne toplotne poškodbe tkiva. Z modeli smo raziskali tudi zmožnost PFA, da ustvari poškodbe ob prisotnosti brazgotinastega tkiva, kar je pomembno za klinični vpogled v zdravljenje aritmij v infarktnih srcih. Razviti modeli se lahko uporabljajo za določanje oblike in velikosti lezij ter morebitnih toplotnih poškodb za različne katetre.

1. Introduction

1.1. Electroporation - the phenomenon

Exposure of cells to short electrical pulses of sufficiently high amplitude to cause a transient increase in cell membrane permeability is called electroporation [1]. If the exposure of the cell to an electric field is short enough and not too intense, and the membrane and cell recovery sufficiently rapid for the cell to remain viable, electroporation is termed reversible. Otherwise, excessive exposure to the electric field results in cell death, and the electroporation is termed irreversible [2].

An important feature of electroporation is its universality. It can occur in all cell types and in any cell arrangement [3]. Because of this universality, electroporation is considered a platform technology [48] and is applied in medicine [4], [5], biotechnology [6], environmental applications [7], [8], and the food industry [9], [10].

1.2. Numerical modeling of pulsed electric field treatment chambers

In the food industry electroporation is often referred to as pulsed electric field (**PEF**) treatment. One of the most important applications of PEF treatment in the food industry is microbial inactivation through the mechanism of irreversible electroporation (juices [11], milk [12], wine [13]). PEF is considered a non-thermal food preservation method, which makes it potentially superior to conventional thermal methods because it can better preserve the sensory, nutritional, and functional properties of food [14], [15].

A key component of the PEF treatment system is the treatment chamber, where the product is exposed to electrical pulses. It consists of at least two electrodes and insulating material between them in different geometrical configurations, resulting in different electric field distributions in the chamber.

There are two types of treatment chambers: static and continuous-flow. Static treatment chambers are primarily intended for laboratory experiments, while continuous-flow treatment chambers can be easily integrated into industrial processes. The most common forms of continuous-flow treatment chambers are parallel plate, colinear, and coaxial, each with its own advantages and drawbacks during the PEF process [9], [16].

Numerical simulations in the field of PEF treatment can be divided into two groups according to Gerlach et al. [17].

The first group focuses on simulations of the electric field in different treatment chambers, ignoring fluid flow and heating. The objective of these simulations is to improve the uniformity of the electric field inside the treatment chamber [18], [19].

The second group focuses on the coupled simulations of the electric field, fluid flow, and heating [20], [21], [22], [23], [24], [25]. These simulations aim to investigate how ohmic heating of the product, caused by electric current flow, interacts with heat transfer through convection and conduction to determine the resulting temperature distribution in the treatment chamber. Most existing studies employ the *"duty cycle" approach*, in which a constant voltage is applied as a boundary condition and the steady-state ohmic heating source is multiplied by a duty factor to account for pulsed energy delivery (see section 2.2.5). While this method greatly reduces computation time, it averages the thermal load and thereby masks transient temperature fluctuations that occur during and between pulses.

Knowledge of the electric field and temperature profile in the treatment chambers during PEF treatment is important because local temperature increases within the flow chamber (due to the electric field and/or fluid flow inhomogeneity) can affect the quality of the food. If the temperature rise is large enough, PEF technology may lose its advantages as a method of non-thermal food processing.

1.3. Numerical modeling of pulsed field ablation of cardiac tissue

In the field of medicine, one of the most promising applications of irreversible electroporation is cardiac tissue ablation, also known as pulsed field ablation (**PFA**). The main advantage of PFA is tissue ablation through a non-thermal mechanism, which preserves nerves, major blood vessels, and other sensitive tissues [26], [27].

Cardiac tissue ablation can be used for the treatment of atrial flutter, atrial fibrillation, and ventricular arrhythmias. The goal of ablation is to destroy the underlying arrhythmogenic tissue and create transmural and contiguous lesions [28]. PFA is rapidly gaining in popularity as a novel non-thermal technique for cardiac ablation and is considered safer than thermal ablation techniques such as radiofrequency ablation (RFA) [27] and cryoballoon ablation [49]. PFA is performed using catheters of various shapes and electrode arrangements (monopolar, bipolar) resulting in different lesion depths. Depending on the thickness of the targeted cardiac tissue

(pulmonary vein ~ 2mm, left ventricular wall ~ 10 mm) different catheter and electrode arrangements are more suitable than others, with focal catheters in a monopolar electrode arrangement producing the deepest lesions. In a monopolar electrode arrangement, the active electrode(s) are placed near the targeted tissue with a return path to a distant dispersive (return) electrode, which could be another electrode or a set of electrodes placed elsewhere in the heart or venous vasculature [29].

Although still in its early stages, the literature on numerical modeling of PFA has expanded rapidly in recent years. Several studies focus on modeling the electric field distribution to predict lesion size or estimate lethal electric field thresholds (LETs) [30], [31], [32], [33], [34]. In parallel, recent studies have begun to model temperature rise during PFA and evaluate the potential for thermal damage [35], [36].

Additionally, there is an established body of literature on modeling heating and possible thermal damage during tissue electroporation [37], [38], [39], [40]. However, these models were developed for non-cardiac tissues and do not include convective cooling of the tissue and electrodes by intracardiac blood flow or catheter irrigation, both of which influence the temperature distribution during PFA. To represent these cooling effects, the literature on modeling temperature distribution during RFA is helpful [41], [42], [43], [44].

The goal of PFA is to achieve sufficient electric field strength in the target tissue to produce the desired lesion depth with minimal temperature rise (minimal risk of thermal damage). Achieving this goal requires detailed knowledge of temperature and electric field distribution during PFA. Therefore, further development of numerical models for PFA is important to help with maximizing both the safety and efficacy of the treatment.

1.4. Aims of the dissertation

Irreversible electroporation is often used as a non-thermal alternative to thermal treatments of food or thermal ablations. The main advantage of electroporation over thermal methods is that its cell-killing mechanism is non-thermal, and therefore it does not have the side effects associated with thermal methods. However, high-voltage and high-pulse-number protocols are often required to achieve irreversible electroporation, which can result in significant ohmic heating and temperature increases in the tissue or treated products. In food processing, high temperatures can affect food quality, and in cardiac tissue ablation, high temperatures can significantly impact treatment safety. Understanding the interplay between electrical and

thermal effects is therefore essential to improve the safety and efficacy of electroporation-based treatments. The overarching aim of this dissertation is to address this by focusing on the development and validation of complex numerical models that can accurately predict electric field and temperature distributions and provide important information on the parameters affecting the safety and efficacy of both PEF and PFA treatments.

Accordingly, two primary aims were pursued:

The first aim was to advance the numerical modeling of continuous-flow PEF treatment chambers. This was achieved through two main contributions. The first was to move beyond the limitations of existing duty cycle models by developing a pulse-resolved numerical model. This validated framework improves upon conventional approximations by simulating each electrical pulse individually, providing critical insights into transient temperature fluctuations that are otherwise smoothed out by the duty cycle approach. Overlooking these transient temperature fluctuations could lead to underestimation of potential thermal damage to the product as well as the associated risk of equipment deterioration. The second contribution was to develop and introduce particle-level exposure analysis, a novel framework that evaluates the electrical and thermal doses experienced by each treated cell or particle, as well as the statistical distribution across the entire product. This analysis provides a direct measure of treatment homogeneity and can reveal the fractions of the product at risk of being under-treated (compromising efficacy) or over-treated (compromising quality), serving as a powerful tool for process optimization.

The second aim was to develop novel numerical models to predict electric field and temperature distributions during cardiac PFA, with the goal of providing crucial insights to improve the safety and efficacy of the clinical procedure. This aim was addressed through two distinct but complementary studies. The first was an *in vitro* study on the mechanism of bubble formation during intracardiac PFA, which can affect treatment safety. In this study, a numerical model of a bipolar PFA catheter in saline solution was developed and validated against high-speed camera recordings from the experiments. This model accurately captured heating around sharp electrode edges and the thermal mechanisms of bubble formation (degassing and boiling), informing the design of safer pulse protocols and electrode geometries. The second study was a comprehensive *in vivo* study of intracardiac PFA in healthy and infarcted swine ventricles. In

the scope of this study, detailed numerical models were developed and used to determine the *in vivo*

lethal electric field threshold (LET) for ventricular myocardium, to gain insight into temperature distribution during PFA and potential thermal damage in tissue, and to investigate the clinically critical question of whether PFA can effectively ablate through heterogeneous and dense scar tissue.

2. Advanced models of continuous-flow pulsed electric field (PEF) treatment chambers

This chapter addresses the first aim of the thesis by developing and validating a pulse-resolved numerical model to study electric field and temperature distribution in continuous-flow PEF treatment chambers. Compared to existing coupled simulations of electric field, fluid flow, and heating, this model improves accuracy by modeling each electrical pulse separately, allowing precise calculation of transient temperature. A condensed version of this work was previously published in a peer-reviewed journal [45].

Additionally, we develop and present a particle-level exposure analysis that can be used as an extension to both the new pulse-resolved model and the more commonly employed duty-cycle model and enables evaluation of the temperature and electric field exposure experienced by individual particles or cells as they flow through the treatment chamber.

2.1. Background

Accurately predicting the temperature distribution during PEF treatment is important, as excessive local heating can compromise product quality and cause the technology to lose its non-thermal advantage. Coupled numerical simulations of the electric field, fluid flow, and heating are an essential tool for this purpose, with the *duty cycle* approach being the standard method in existing literature. Instead of modeling each electrical pulse, this method uses a constant voltage as a boundary condition. And to simulate the temperature increase, the steady state ohmic heating source is then multiplied by a duty factor (see section 2.2.5) to relate it to the pulsating heat source, making the simulations more computationally efficient. However, this efficiency comes at a cost. By averaging the thermal load, the duty cycle approach masks the transient temperature fluctuations that occur during and between individual pulses. This can lead to an underestimation of peak temperatures in hotspots, potentially failing to predict thermal damage to the product or risks to equipment integrity.

The first objective of this chapter, is to develop and validate a pulse-resolved numerical model that simulates each electrical pulse separately, providing a more accurate representation of both temperature and electric field dynamics inside the treatment chamber.

While a pulse-resolved model provides accurate, time-varying distributions of the electric field and temperature inside the treatment chamber, a complete understanding of the PEF treatment

requires evaluating what the moving product actually experiences. PEF processes are often characterized by parameters based on average residence time of the product, such as treatment time and total specific energy input (see 2.2.3). However, due to the nature of fluid flow, the actual trajectory of any given particle or cell can vary significantly, resulting in a wide distribution of received electrical and thermal doses. To accurately assess outcomes such as microbial inactivation and product quality, it is important to move beyond these bulk averages and quantify treatment homogeneity/heterogeneity. Evaluating the full statistical distribution of exposures across the entire particle population provides this essential information.

Therefore, the second objective of this chapter is to introduce and demonstrate a particle-level exposure analysis. This framework is used to calculate the unique treatment history, i.e. exposure to electric field and temperature, for each individual particle, allowing us to quantify the distribution of exposures and treatment homogeneity/heterogeneity, which could provide an important link to real-world PEF process efficacy and safety.

2.2. Methods

2.2.1. Experimental setup and measurements

This section describes the experimental setup used to validate the pulse-resolved numerical model of continuous-flow PEF treatment chambers.

Figure 2-1 shows the complete experimental setup. In all experiments, 0.18 % (w/v) NaCl solution served as the product surrogate/analogue, as its electrical conductivity at 25 °C (0.352 S/m, calculated using the model described in [50]) is very close to that of fresh orange juice at 25 °C (0.343 S/m [51]). We obtained the 0.18 % saline solution by diluting a commercial 0.9 % NaCl solution (B. Braun, Melsungen, Germany) with a topical irrigation solution (Aqua by B. Braun, Melsungen, Germany), in a 1:4 ratio.

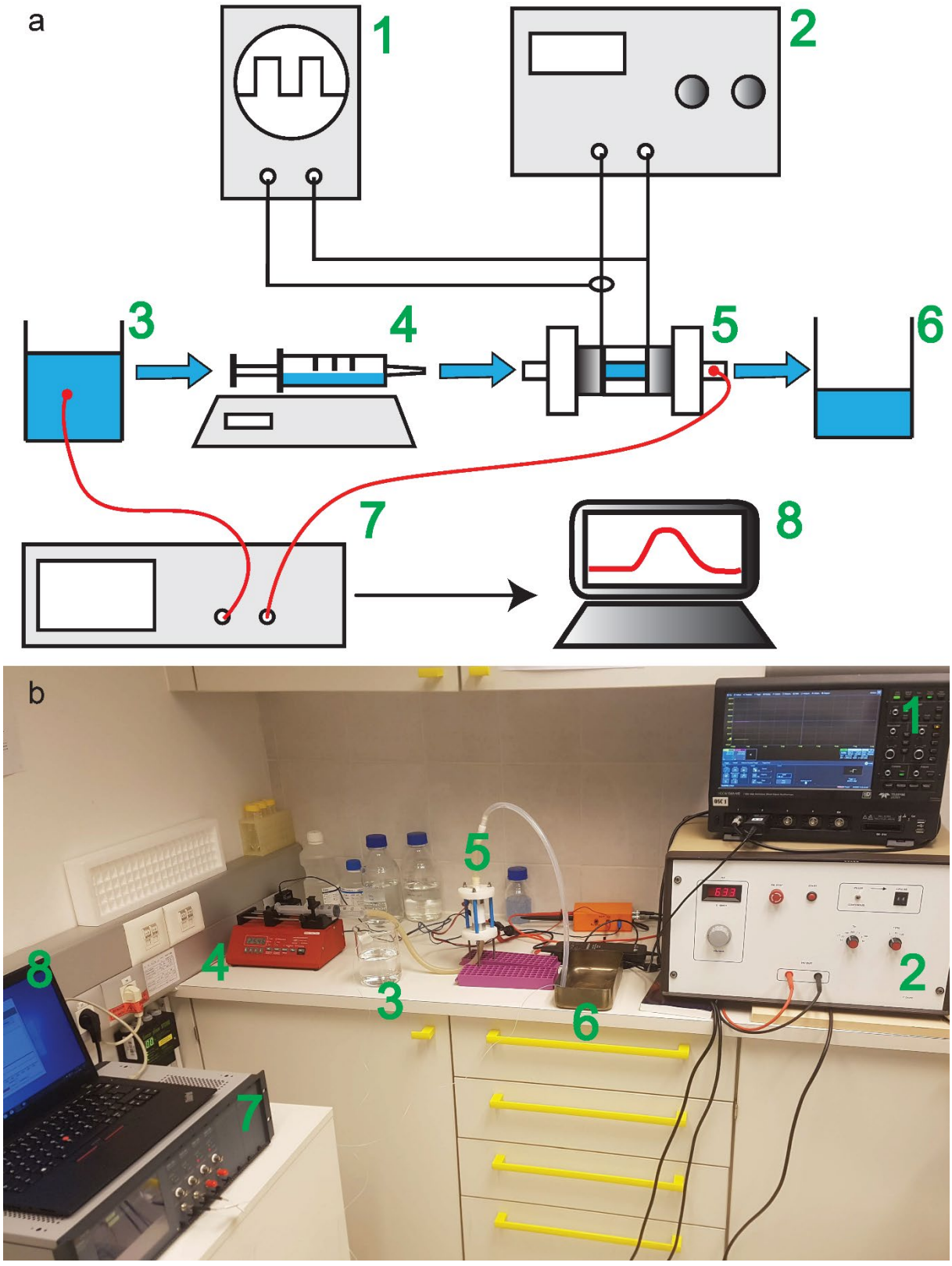

Figure 2-1: a) Schematic representation of the experimental setup: oscilloscope (1), pulse generator (2), 0.18 % NaCl solution (3), syringe pump (4), continuous-flow treatment chamber (5), waste reservoir (6), optical thermometer (7) with temperature sensors in red, and computer (8). b) Photo of the experimental setup. Figure adapted from [45].

Saline solution was pumped using an Aladin-1000 syringe pump (World Precision Instruments, USA) with a 50 ml BD Plastipak plastic syringe. The pump allows a maximum syringe volume of 60 ml and a maximum pumping rate of 35.3 ml/min.

Two continuous-flow treatment chambers were used in the experiments: a colinear treatment chamber [52] and a parallel plate treatment chamber [53], both kindly provided by Gianpiero Pataro (University of Salerno, Fisciano, Italy), hereafter referred to as the *colinear* and *parallel plate* treatment chambers, respectively (Figure 2-2). During the experiments, the treatment chambers were oriented vertically, with the saline solution pumped upward against gravity to allow any gas bubbles that formed at the electrodes during pulse application to exit the chamber.

Masterflex 96410-16 silicone tubing with an inner diameter of 3.1 mm (Cole-Parmer, USA) was used to connect the syringe pump to the inlet and outlet of the parallel plate treatment chamber and to a waste reservoir. For the colinear treatment chamber, silicone tubing from a local manufacturer with an inner diameter of 12 mm was used.

A new plastic syringe was used for each experiment, and the silicone tubing was rinsed with distilled water before and after each experiment. After each experiment, the treatment chambers were rinsed with distilled water, disassembled, the electrodes polished, cleaned with 70 % ethanol, rinsed again, and reassembled.

Unipolar square wave pulses were applied using a pulse generator developed and described in [54]. To generate square-shaped pulses, the “Bruno” pulse generator uses a high-voltage switch consisting of optically controlled transistors connected in series. The maximum output voltage of the pulse generator is 5000 V, and the maximum output current is 100 A. Possible pulse lengths are 10 µs, 50 µs, 100 µs, 500 µs, 1 ms, 5 ms, and 10 ms, with pulse repetition frequencies of 1 Hz, 10 Hz, and 100 Hz, either as a discrete number of pulses (between 1 and 99) or with continuous pulse delivery.

Voltage and current were recorded in sequential capture mode with a LeCroy HDO6104A-MS digital oscilloscope (Teledyne LeCroy, USA) using a 100 MHz high-voltage differential probe (LeCroy HVD3605A) and a 100 MHz current probe (LeCroy CP031A).

During each application of the pulse protocol, the temperature at the outlet of the chamber was recorded using an OpSens PSC-D-N-N optical thermometer equipped with four PSR-G1-10-100ST single-channel modules (OpSens Solutions Inc., Canada) and an OpSens OTG-MPK5 fiber optic temperature sensor. The optical sensor used has a response time of less than 225 ms

and an accuracy of ± 0.3 °C over its operating range of 20–150 °C. The recorded signals were processed using SoftProSense software from OpSens. To improve the signal-to-noise ratio, a running average filter with a kernel size of 10 was applied to all measurements. The sensor was positioned at the outlet at the location marked in Figure 2-2, panels c and f. The temperature of the 0.18 % NaCl solution used for the experiments and the environment (room temperature) were monitored as references.

The electrical conductivity of the NaCl solution was measured using the SevenCompact conductometer (Mettler Toledo, USA) before performing the experiments.

2.2.2. PEF Treatment chamber geometries

Figure 2-2 shows the two continuous-flow treatment chambers used in the experiments and represented in the numerical model: a colinear chamber and a parallel-plate chamber, with detailed dimensions used to create the 3-D geometries in the numerical model. The red dots indicate the approximate position of the temperature sensor during the experiments.

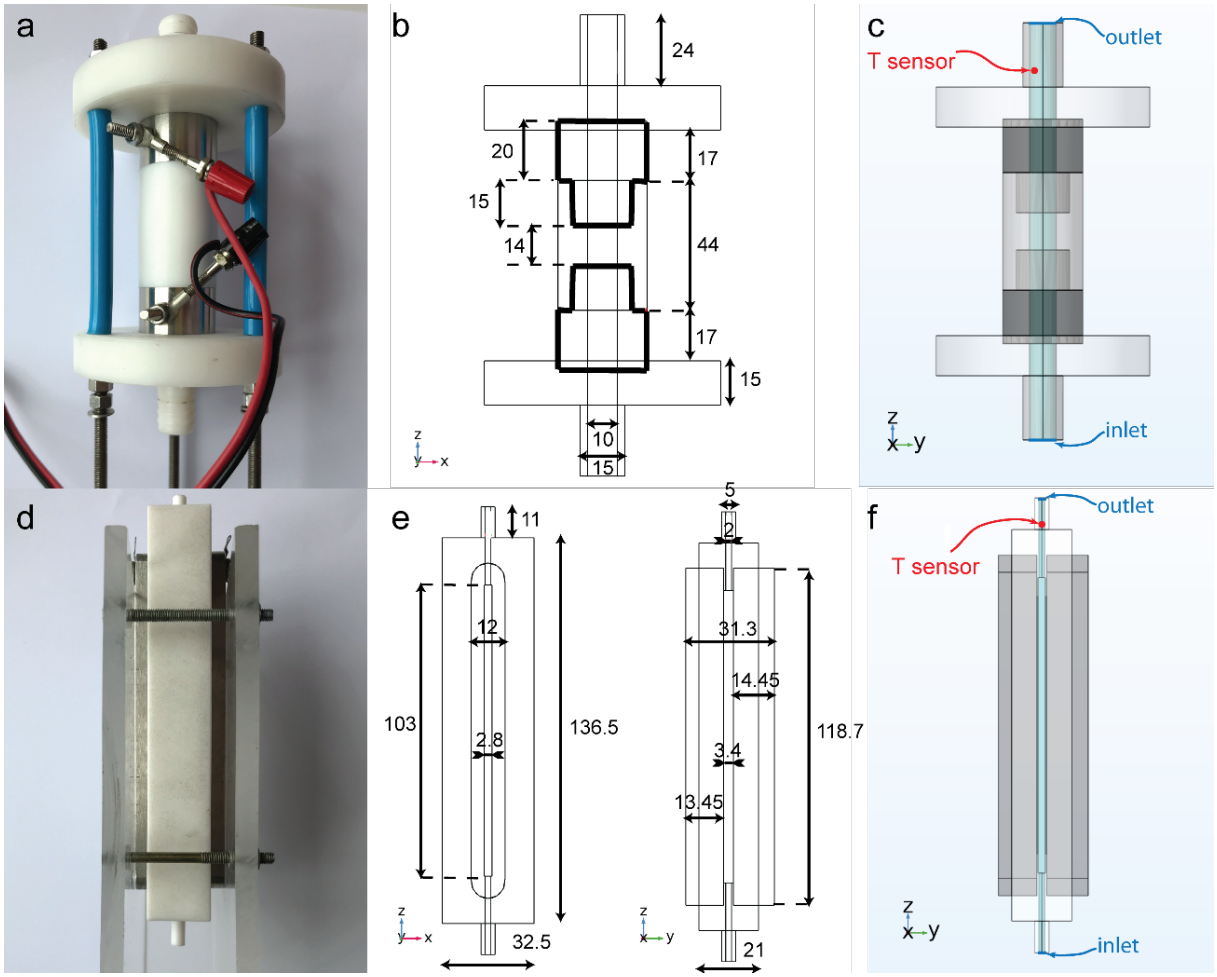

Figure 2-2: Continuous-flow treatment chambers used in the experiments and in the numerical model: a) photo of the colinear treatment chamber; b) detailed geometry of the colinear treatment chamber with measurements (in mm); c) 3-D geometry of the colinear treatment chamber used in the numerical model (electrodes are colored in gray); d) photo of the parallel plate treatment chamber; e) detailed geometry of the parallel plate treatment chamber with measurements (in mm); f) 3-D geometry of the parallel plate treatment chamber used in the numerical model (electrodes are colored in gray). The red dots in c) and f) indicate the approximate position of the temperature sensor during the experiments. Figure adapted from [45].

The Colinear treatment chamber consists of a Teflon holder and two stainless steel electrodes with an inter-electrode distance (L) of 14 mm, reduced from the original 15 mm, likely due to material degradation from frequent use. The chamber has an inner diameter of 10 mm, resulting in a treatment volume ($V_{\text{treatment}}$) of 1.1 ml, which is the active part of the chamber.

The parallel plate treatment chamber originally consisted of a Teflon holder and two stainless steel electrodes with an initial inter-electrode distance (L) of 2.5 mm, and a treatment volume width and length of 2.8 mm and 103 mm, respectively. However, due to liquid leakage, likely caused by repeated assembly and disassembly, the chamber was slightly modified for our experiments. Silicone rubber gaskets were placed between the electrodes, and the entire chamber was compressed between two acrylic glass plates. With the addition of the silicone gaskets, the new inter-electrode distance (L) became 3.4 mm, and the electrode surface area decreased from 288 mm² to 219 mm², as the compressed gaskets expanded laterally and partially covered the interface between the electrode and the liquid. These changes were incorporated into the numerical model, resulting in an irregularly shaped treatment volume ($V_{\text{treatment}}$) of 0.826 ml (further detailed in Figure 2-3).

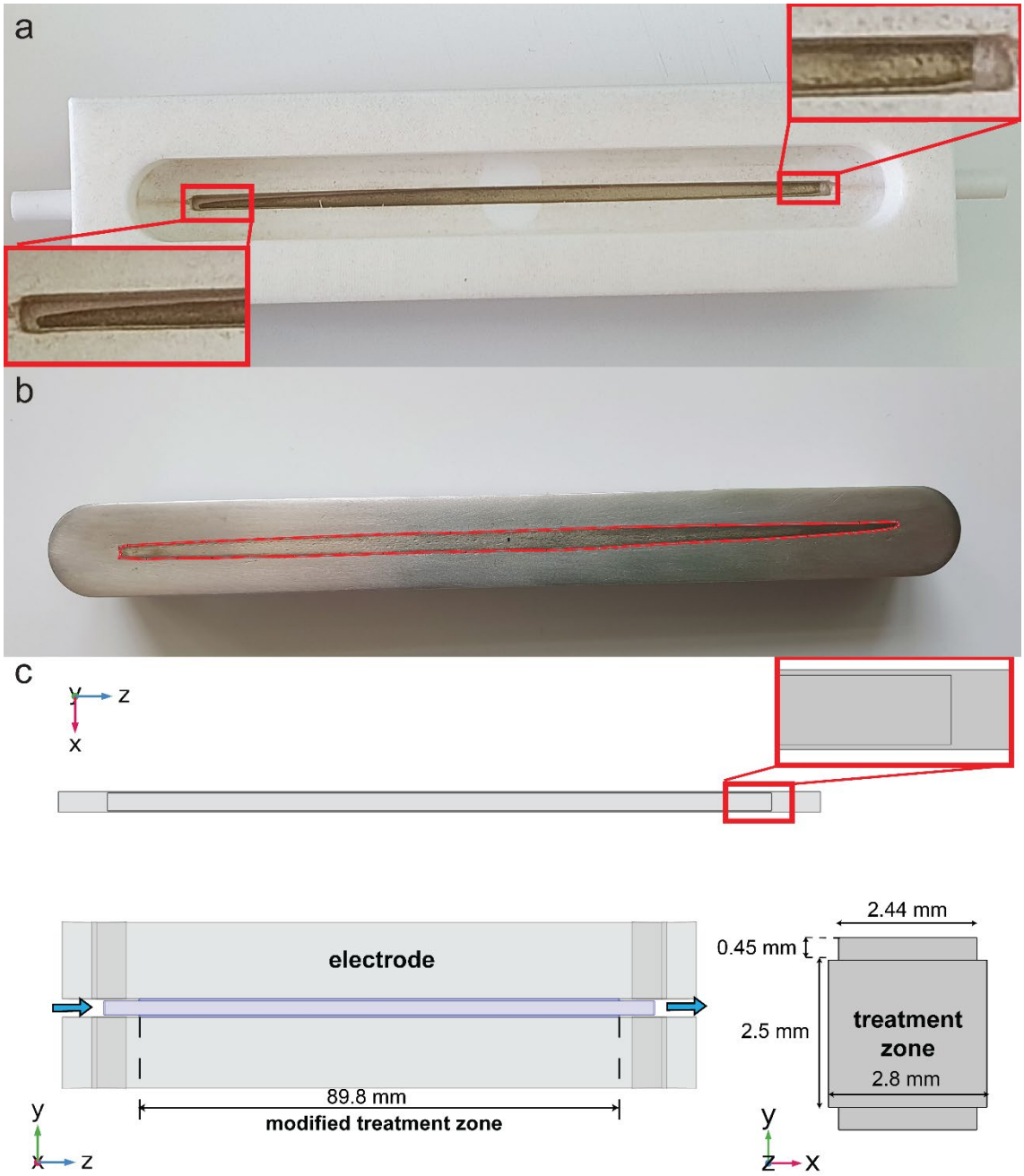

Figure 2-3: Effect of gaskets on the electrode surface area and treatment volume, and how these were incorporated into the model. a) Disassembled parallel plate treatment chamber after the experiments - gaskets obstruct the interface between the electrode and the liquid. b) The new reduced electrode surface area determined with ImageJ is 219 mm² (76% of the original value, 288 mm²). c) New modified electrode surface area and treatment volume in the numerical model; reduced electrode surface area was approximated by a rectangle, by multiplying the length (103 mm) and width (2.8 mm) of the original/unobstructed electrode surface area by a factor of 0.87 ($\sqrt{0.76}$). The treatment volume in the numerical model was modified by adding a cuboid with the new surface area (89.8 mm × 2.44 mm) and the thickness of the gasket (0.45 mm) on each side to the original treatment volume. The modified treatment volume was calculated as follows: $V_{treatment}$ = (89.8× 2.8× 2.5) mm³ + 2× (89.8× 2.44× 0.45) mm³ = 826 mm³ = 0.826 ml. Figure adapted from [45].

2.2.3. Pulse protocols and PEF treatment parameters

The pulse protocols used in the experiments and simulations are listed in Table 2-1 along with the main PEF treatment parameters according to [55]. An example of the pulse shape is shown in Figure 2-4.

We used two types of pulse application in the experiments: a fixed number of pulses and continuous pulse delivery. We chose protocols with a fixed number of pulses, to simplify the experiments and simulations. However, for practical use of continuous flow treatment chambers, evaluating continuous pulse delivery is crucial. Therefore, we used two continuous pulse delivery protocols for each treatment chamber in our experiments, focusing on achieving steady-state conditions (i.e., a constant outlet temperature).

The pulse protocols in the simulations mirror the pulse protocols used in the experiments. We also added two additional higher energy PEF protocols for the colinear chamber that are closer to the electric fields and energies used on an industrial scale – shaded gray in Table 2-1.

Pulse protocols are listed as:

$$N \times \tau, \qquad f \tag{2.1}$$

where N is the total number of pulses delivered. For continuous pulse delivery, the abbreviation "*cont.*" is used. τ stands for the pulse width, which is full width of the pulse at half maximum value, for a square-shaped pulse [56]. f is the pulse repetition frequency.

The volumetric flow rate (F) was selected based on the treatment volume ($V_{\text{treatment}}$) of the chamber and the limitations of the Aladin-1000 syringe pump. The peak voltage (U) was chosen within the limits of the pulse generator, high voltage probe, and current probe, to avoid dielectric breakdown (sparking or arcing) and damage to the voltage/current probes.

To better compare the results of different experiments and studies, it is useful to define the "voltage to distance" ratio (VDR) as the peak voltage (U) divided by the distance between the electrodes (L) (equation 2.2):

$$VDR = \frac{U}{L} \tag{2.2}$$

The VDR can be considered a good estimate of the electric field strength in the treatment volume for a parallel plate electrode configuration, but not for a colinear electrode configuration

due to the non-uniform distribution of the electric field. To estimate the electric field in the treatment volume more accurately, we can use results from numerical simulations.

Table 2-1: Pulse protocols and main PEF treatment parameters used in experiments and simulations.

Treatment chamber	Pulse protocol	F [ml/min]	U [V]	VDR [V/cm]	n	t [µs]	W_T [kJ/kg]
Colinear	10 × 100 µs, 1 Hz	10	4000	2860	6.6	660	15.6
		20			3.3	330	7.8
	cont. 100 µs, 1 Hz	20			3.3	330	7.8
	64 ×10 µs, 10 Hz	10			64**	640**	15.1**
		20			33	330	7.8
	cont. 10 µs, 10 Hz	20			33	330	7.8
Colinear*	cont. 100 µs, 1 Hz	33.3	14000	10000	2	200	71
	cont. 10 µs, 10 Hz				20		
Parallel Plate	10 × 100 µs, 1 Hz	10	1000	2940	5	500	14.0
		20			2.5	250	7.0
	cont. 100 µs, 1 Hz	20			2.5	250	7.0
	64 × 10 µs, 10 Hz	10			50	500	14.0
		20			25	250	7.0
	cont. 10 µs, 10 Hz	20			25	250	7.0

* Hypothetical high energy protocols – simulation only

** $N < n$, total number of pulses (N) is smaller than calculated number of pulses applied (n).

In continuous pulse application mode, the number of applied pulses (n) to the product is not set directly by the user as in batch treatment, but is determined by the pulse frequency (f) and the residence time (t_r) of the product in the treatment chamber. The residence time depends on the flow rate (F) and the treatment volume of the chamber ($V_{treatment}$). The number of applied pulses (n) can be calculated according to equation 2.3:

$$n = t_r \cdot f = \frac{V_{treatment}}{F} \cdot f \qquad 2.3$$

The treatment time (t) is defined as the number of applied pulses (n) to the product, multiplied by the pulse width (equation 2.4):

$$t = n \cdot \tau \qquad 2.4$$

W_T stands for the total specific energy input and can be calculated by multiplying the specific energy per pulse (W) by the number of applied pulses (n) (equation 2.5):

$$W_T = W \cdot n \qquad 2.5$$

W represents the electrical energy that the treated product receives per pulse and is determined by integrating the recorded current and voltage waveforms over time for a representative pulse (equation 2.6):

$$W = \frac{1}{m}\int_0^\infty U(t)\cdot I(t)dt = \frac{1}{v\cdot\rho_{H_2O}}\int_0^\infty U(t)\cdot I(t)dt \qquad 2.6$$

It is important to note that the residence time (t_r), which is used to calculate the number of applied pulses (n) to the product (equation 2.3) and consequently the total specific energy input (W_T), represents the average residence time of the product in the treatment volume (the active part of the chamber). This means that the number of pulses applied, the treatment time, and the total specific energy all represent average values received by the product. Depending on the trajectory of specific cells or particles within the treatment chamber, these values can vary substantially. For example, in the case of a parabolic velocity profile, the residence time of the product flowing along the walls of the treatment volume is longer than that of the product flowing in the middle of the channel.

We analyze this trajectory-level variability via particle-level exposure analysis and report the resulting exposure distributions in Sections 2.2.6 and 2.3.4.

2.2.4. Pulse-resolved numerical model of continuous flow PEF treatment chamber

COMSOL Multiphysics (version 6.0, COMSOL AB, Sweden) was used to develop the pulse-resolved numerical model of continuous-flow PEF treatment chambers.

2.2.4.1. Model geometry

The exact 3D geometries for both treatment chambers were created based on the measurements shown in Figure 2-2, panels c and f.

2.2.4.2. Simulation workflow

The simulation workflow was as follows: First, the fluid flow through the chamber was solved using a stationary study. The solution from the flow study was then used in the subsequent coupled, time-dependent study (one-way coupled), in which the electric field and temperature distribution were solved simultaneously (bidirectionally coupled).

A fully coupled solver with the automatic damped Newton method was used for the stationary study, while a fully coupled solver with the constant damped Newton method was used for the coupled time-dependent study. In the time-dependent study, time steps of 1/100 of the pulse

period ($t_p = f^{-1}$) were set as output times, and the method of intermediate time steps in the solver was selected. This method ensures that the time-dependent solver takes at least one time step in each sub-interval of the required output times.

2.2.4.3. Fluid flow

The fluid flow through the treatment chamber was assumed to be laminar (the Reynolds numbers for the colinear and parallel plate treatment chambers at a flow rate of 20 ml/min are 42 and 212, respectively) and incompressible. The Laminar Flow interface in COMSOL was used to model the fluid flow, where the incompressible form of the continuity equation (2.7) for conservation of mass and the Navier–Stokes equation (2.8) for conservation of momentum were solved:

$$\nabla(\rho \boldsymbol{u}) = 0 \qquad 2.7$$

$$\rho\left(\frac{\partial \boldsymbol{u}}{\partial t} + \boldsymbol{u} \cdot \nabla \boldsymbol{u}\right) = -\nabla p + \nabla \cdot (\mu(\nabla \boldsymbol{u} + (\nabla \boldsymbol{u})^T) \qquad 2.8$$

Here, $\boldsymbol{u}$ is the fluid velocity, p is the fluid pressure, ρ is the fluid density, and μ is the fluid dynamic viscosity. The fluid density was determined at a reference pressure of 101.3 kPa and a reference temperature of 20°C.

The volumetric flow rate was set as the boundary condition at the inlet, and a fully developed flow option was chosen in COMSOL, forcing the flow at the inlet toward the solution for a fully developed channel flow (parabolic velocity profile). At the outlet, a zero-pressure boundary condition was specified, and at the inner walls of the flow channel, a non-slip boundary condition (i.e., the velocity is set to zero) was specified. The positions of the inlet and outlet boundary conditions within the geometry of each chamber can be seen in Figure 2-2, panels c and f.

2.2.4.4. Electric field distribution

To model the electric field in the chamber during pulse delivery, the Electric Currents interface in COMSOL was used, where the continuity equation (2.9) for the conservation of charge was solved:

$$\nabla \cdot (\sigma \nabla V(t)) = 0 \qquad 2.9$$

where V is the electric potential and σ is the electric conductivity.

An electric potential boundary condition was applied at the electrodes. The voltage at the ground electrode was set to zero and a time-dependent voltage was set at the active electrode. At all other boundaries around the flow channel, including the inlet and outlet, an electric insulation (i.e., no electric current flows through the boundary) was set as the boundary condition.

To model the electrical pulses of the different protocols used in this study as accurately as possible, the voltage recorded by the oscilloscope was used in the model. For each pulse protocol and treatment chamber, a representative pulse was selected from the voltage recording, first filtered using a Butterworth filter, then suitably decimated using MATLAB (MathWorks, USA) and imported into COMSOL (Figure 2-4). The imported waveform served as the basis for an analytical function with a periodic extension, where the pulse period ($t_p = f^{-1}$) was specified for each pulse protocol to transform the representative pulse into a pulse protocol comprising multiple pulses. The analytical function describing the time-varying voltage for a given pulse protocol was then used as the boundary condition for the active electrode.

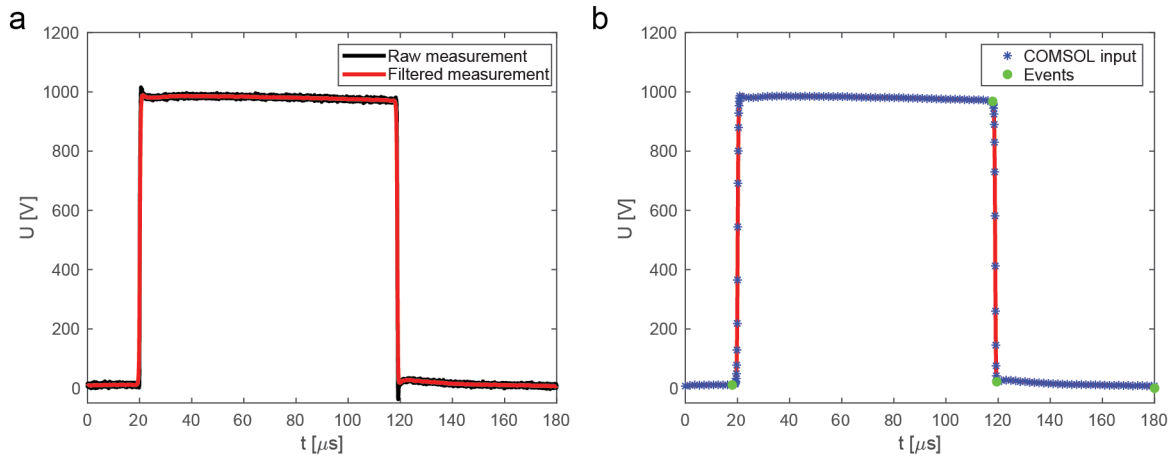

Figure 2-4: Representative unipolar square-wave pulses as applied and measured in experiments and used in the model. (a) Recorded voltage signal for a representative pulse from the 10 × 100 µs pulse protocol for the parallel plate treatment chamber, along with the corresponding filtered and decimated signal. (b) Individual pulse points (blue asterisks) imported into the numerical model, with event points (green dots) used to accurately model the time-varying voltage. Figure adapted from [45].

To ensure that COMSOL's time-dependent solver accurately models each square-wave electrical pulse, the Events interface was used. This interface forces the solver to take additional time steps and reinitialize the dependent variables at the specified event times. To accurately represent the pulses used in our study, four event points with a period equal to the pulse period

(t_p) were defined at the critical points of the representative square-shaped pulse (green dots in Figure 2-4). For an idealized square-shaped pulse, only two event points are needed: one at the beginning of the rising edge and one at the beginning of the falling edge of the pulse.

The Events interface provides an efficient and accurate way to model the transient behavior of the solution to the partial differential equation (e.g., electric potential for the conservation of charge equation and temperature for the heat transfer equation) when the solution/dependent variable (e.g., electric potential in the charge conservation equation) or the load/source term (e.g., ohmic heating in the heat transfer equation) changes on a time scale significantly shorter than that of the entire simulation. This approach avoids the need to significantly reduce the solver's time step size, thereby preventing a substantial increase in simulation time.

2.2.4.5. Temperature distribution

To model the temperature in the treatment chamber, the Heat Transfer in Solids and Fluids interface in COMSOL was used, where the heat equation (2.10) for the conservation of energy was solved:

$$\rho c_P \left(\frac{\partial T}{\partial t} + \boldsymbol{u} \cdot \nabla T\right) - \nabla \cdot (k \nabla T) - Q = 0 \qquad 2.10$$

here ρ is the density, c_P is the heat capacity at constant pressure, k is the thermal conductivity, $\boldsymbol{u}$ is the fluid velocity field and Q is the heat source (load).

To model the heating of the fluid during pulse application, we used the Electromagnetic Heating Multiphysics coupling interface in COMSOL, which couples the heat equation for conservation of energy with the continuity equation for conservation of charge and adds a resistive (ohmic) heating source to the heat equation. In our model, a time-dependent (ohmic) heating source was used:

$$Q(t) = Q_{ec}(t) = \sigma(T) E(t)^2 \qquad 2.11$$

$\sigma(T)$ is the temperature-dependent electric conductivity of the NaCl solution and $E(t)$ is the time-varying electric field distribution in the treatment volume, which was calculated together with the temperature distribution in a coupled time-dependent study. For the convection term in the heat equation, the solution from the previous fluid flow study was used as the fluid velocity field.

The following boundary conditions were specified. At the outer surface of the treatment chamber, a thermal insulation boundary condition was used (no heat flux across the boundary),

as there is negligible contribution of natural convection to heat dissipation from the treatment chamber surface. At the inlet of the treatment chamber (Figure 2-2, panels c and f), an inflow boundary condition with an upstream temperature was specified. For the upstream temperature and the initial temperature of the treatment chamber, the temperature of the fluid measured within the outlet of the treatment chamber just before pulse application was specified (T_i, see Figure 2-9).

2.2.4.6. Material properties

The material properties at room temperature (20°C) for the treatment chamber and the fluid (saline solution) can be found in Table 2-2 and Table 2-3 respectively.

Table 2-2: Material properties at room temperature (20°C) for the treatment chambers

Element/Material	k [W/mK]	c_P [J/kgK]	ρ [kg/m^3]
Electrodes/Stainless steel	14	500	7760
Insulator/Teflon	0.27	2150	2150

Table 2-3: Material properties at room (and inlet) temperature (20°C) for the fluid

Element/Material	k [W/mK]	c_P [J/kgK]	ρ [kg/m^3]	σ [S/m]	μ [kg/ms]
Fluid/0.18% $NaCl_{(aq)}$*	0.594	4187	998	0.316	0.001

*water with modified electrical conductivity

The temperature-dependent material properties for the Teflon holder/insulator (Figure 2-2, panels c and f, white) and stainless-steel electrodes (Figure 2-2, panels c and f, gray) as well as the 0.18 % saline solution were taken from the COMSOL Material Library using the materials Teflon (polytetrafluoroethylene), 2101 duplex stainless steel and water respectively. For the 0.18 % saline solution, temperature-dependent electrical conductivity was calculated using the model described in [50]. The calculated temperature-dependent electrical conductivity of the 0.18 % saline solution is shown in Figure 2-5.

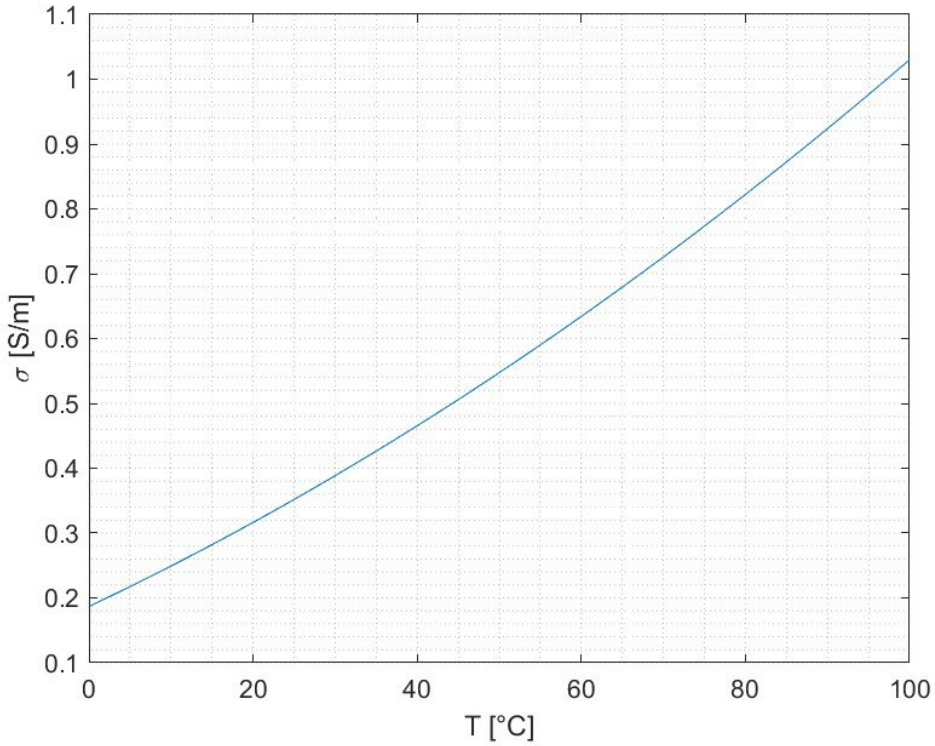

Figure 2-5: Electrical conductivity of 0.18% NaCl used in the model, calculated according to the equations described in [50]. Figure adapted from [45].

The validity of the temperature-dependent electrical conductivity model was tested for the 0.18% saline solution at room temperature (20–23°C) and at higher temperatures (60–70°C) using a conductometer. The deviation of the model from the measurements was found to be less than 1%.

2.2.4.7. Finite element mesh

The finite element mesh was primarily constructed from tetrahedral elements. Prismatic elements were used for the boundary layers along the flow channel, and in the case of the parallel plate treatment chamber, pyramid elements were also used to create a transition between tetrahedrons and prisms. The final mesh was selected based on the required resolution of the temperature change in the hot spots and the simulation time. It consisted of 22110 elements (17286 tetrahedrons, 4824 prisms) for the colinear treatment chamber and 139510 elements (116318 tetrahedrons, 19828 prisms, and 3363 pyramids) for the parallel plate treatment chamber. Results of mesh independence study are shown in Figure 2-6.

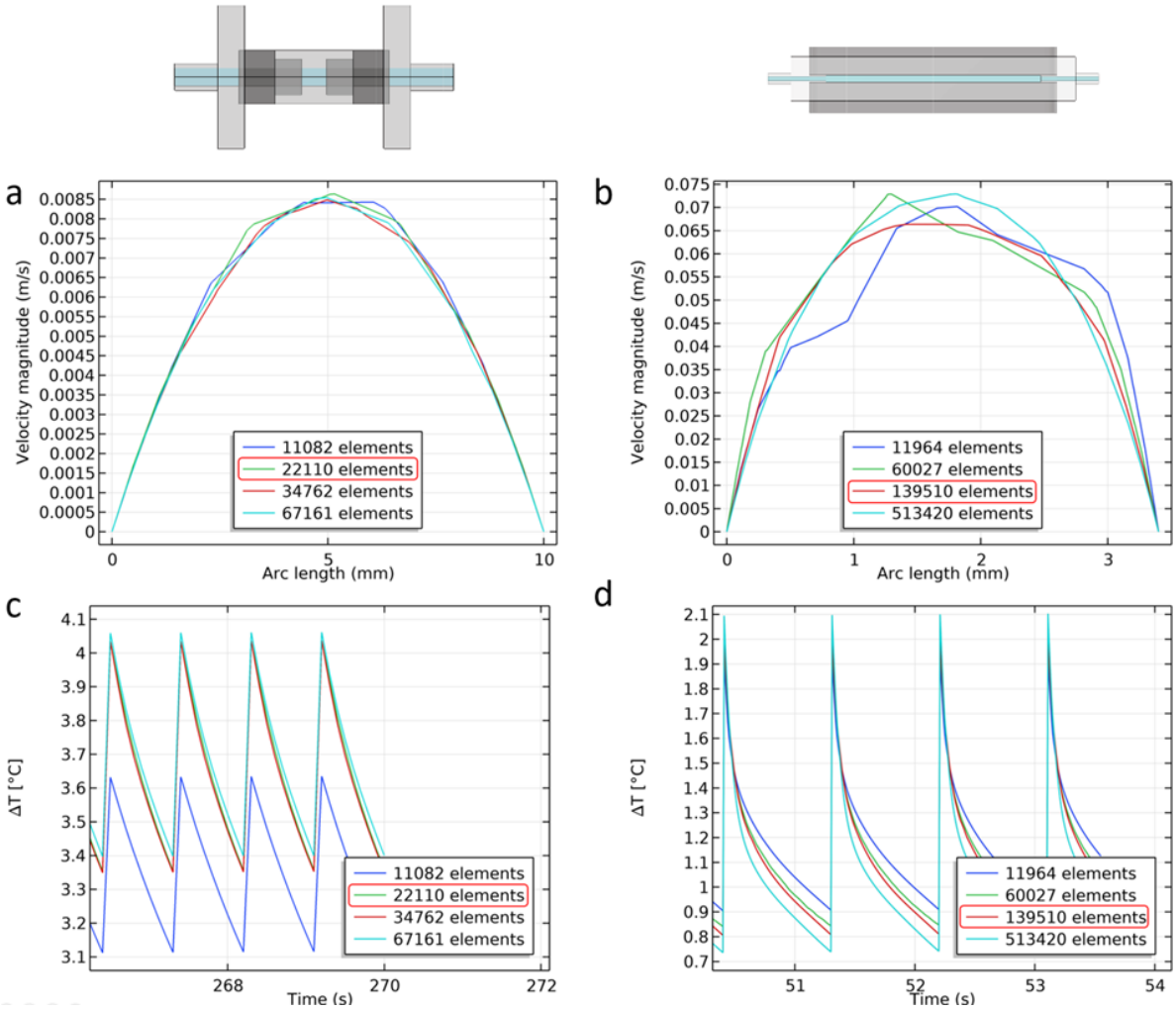

Figure 2-6: Mesh independence study. Simulated fluid flow velocity profiles across the center of the chamber using meshes with different numbers of elements for colinear (a) and parallel plate (b) treatment chambers at a flow rate of 20 ml/min. Simulated temperature changes evaluated at the hot spot using meshes with different numbers of elements for colinear (c) and parallel plate (d) treatment chambers for the continuous pulse application protocol: 100 µs, 1 Hz, F = 20 ml/min, and U = 4000 V (colinear) or U = 1000 V (parallel plate). The mesh used in the numerical model is circled in red. Figure adapted from [45].

2.2.5. Comparison of pulse-resolved model with the duty cycle model

To compare and investigate the differences between our pulse-resolved numerical modeling approach and the commonly used duty cycle approach, we adapted the pulse-resolved model described in 2.2.4 to use the duty cycle approach and ran simulations for both treatment chambers and different PEF protocols.

The same finite element meshes, output times, solver configurations, physics and boundary conditions were used for the duty cycle model as described in section 2.2.4. The only difference from the pulse-resolved approach was the use of a time-invariant voltage as the boundary

condition for the active electrode and the multiplication of the (now) stationary ohmic heat source (Q) by the duty factor ($duty$=$\tau \cdot f$):

$$Q = duty \cdot Q_{ec} = \tau \cdot f \cdot \sigma E^2 \qquad 2.12$$

where τ is the pulse width, f is the pulse repetition frequency, E is the electric field distribution in the treatment volume and σ is the electrical conductivity of the medium.

To ensure the same energy input for both modeling approaches, we used idealized square-wave pulses (instead of a representative pulse from the voltage recording) with a rise and fall time of one hundredth of the pulse width in the pulse-resolved model.

2.2.6. Particle-level exposure to electric field and temperature

To assess the exposure of individual particles (representing cells) to temperature and electric field along their trajectory in the treatment chamber, we extended the pulse-resolved model of continuous flow PEF chambers (described in 2.2.4) and the duty cycle model (described in 2.2.5) by integrating particle tracing functionality in COMSOL Multiphysics.

2.2.6.1. Workflow

The particle-level exposure analysis is an extension of the pulse-resolved and duty cycle models described in sections 2.2.4 and 2.2.5. To calculate particle trajectories and exposure to the electric field and temperature, a special time-dependent study using particle tracing in fluid flow was implemented in COMSOL Multiphysics. This study reused the results from the fluid flow, temperature, and electric field simulations. Particle trajectories were calculated based on the fluid flow solution, using the same time steps as the coupled electro-thermal time-dependent study to ensure accurate interpolation of the temperature and electric field values that the particles are exposed to along their paths.

2.2.6.2. Colinear treatment chamber and laminar pipe flow equations

Particle-level exposure analysis was implemented only for the colinear treatment chamber. The same model geometry and mesh were used as described in section 2.2.4.

This geometry was selected because the flow channel in the colinear chamber is a perfect cylinder, and the laminar pipe flow has analytic solutions for the velocity profile. The axial velocity for fully developed laminar flow in the colinear chamber depends on the radius *r* and can be expressed as:

$$u(r) = 2\bar{u} \cdot (1 - r^2/R^2) \quad 2.13$$

where R is the inner radius of the flow channel in the colinear chamber, and $\bar{u}$ is the average velocity, which can be calculated as:

$$\bar{u} = \frac{F}{\Pi R^2} \quad 2.14$$

The residence time of a particle flowing at a certain velocity can be calculated as:

$$t_r = \frac{L}{u(r)} \quad 2.15$$

where L is the length of the treatment volume, defined as the distance between the electrodes in the colinear chamber. The average residence time can be calculated as:

$$\bar{t_r} = \frac{L}{\bar{u}} \quad 2.16$$

Using the above equations, we can derive both the probability density function (PDF) and the cumulative distribution function (CDF) for the velocity:

$$f_u(u) = \frac{u}{2\bar{u}^2}, \qquad 0 \le u \le u_{max} = 2\bar{u} \quad 2.17$$

$$F_u(u) = \int_0^u f_u(u)du = \frac{u^2}{4\bar{u}^2}, \qquad 0 \le u \le u_{max} = 2\bar{u} \quad 2.18$$

and for the residence time (full derivation detailed in [57]):

$$f_{t_r}(t_r) = \frac{\bar{t}_r^2}{2 \cdot t_r^3}, \qquad t_r \ge \frac{\bar{t_r}}{2} \quad 2.19$$

$$F_{t_r}(t_r) = \int_0^{t_r} f_{t_r}(t_r)dt_r = 1 - \frac{\bar{t}_r^2}{4 \cdot t_r^2}, \qquad t_r \ge \frac{\bar{t_r}}{2} \quad 2.20$$

These equations were used to validate the distributions of tracked particle velocities and residence times (see section 2.3.4.1).

2.2.6.3. Particle tracing in fluid flow

To calculate particle trajectories and exposure to the electric field and temperature in the colinear treatment chamber, we used the Particle Tracing in Fluid Flow interface in COMSOL.

We applied the massless approximation for particles, meaning the particles follow the fluid velocity streamlines exactly, without inertia-induced deviations.

We used two different strategies to release the particles:

- **Representative particle trajectories:** We selected five specific particle trajectories based on volumetric flow percentiles. By integrating the volumetric flow radially outward, we identified radii (r_p) where the cumulative total (p) reaches 0 %, 50 %, 75 %, 90 %, and 99 % of the total volumetric flow:

$$p = \frac{F(r_p)}{F} = \frac{\int_o^{r_p} u(r) 2\pi r dr}{\int_o^R u(r) 2\pi r dr} = \frac{2r_p^2}{R^2} - \frac{r_p^4}{R^4} \quad 2.21$$

$$r_p = R\sqrt{1 - \sqrt{1 - p}} \quad 2.22$$

- **Population:** We released 10,000 particles with velocity-weighted probability (proportional to the local velocity magnitude) to ensure the ensemble accurately represents the entire population of cells in the treated product. Particles were tracked until the slowest particle exited the treatment volume (active region).

2.2.6.4. Calculating particle-level exposure to electric field and temperature

Particle-level exposure was evaluated for the two hypothetical higher energy pulse protocols with the same treatment time and total energy input: 100 µs pulses at 1 Hz and 10 µs pulses at 10 Hz, each at delivered voltage of 14 kV, and a flow rate of 2 L/h (for more information, see Table 2-1, shaded gray).

For each particle, we determined exposure to the electric field and temperature by using the calculated particle trajectories to evaluate the electric field and temperature values at the particle's location at each time point.

We also calculated the maximum temperature each particle experienced and the cumulative time the particle was exposed to an electric field above a specified threshold – specifically, the cumulative exposure time above 5 kV/cm. In the case of the duty cycle model, where the electric field is stationary, the calculated cumulative exposure time was multiplied by the duty factor ($duty = \tau \cdot f$) to relate it to the pulse-resolved model.

2.3. Results

2.3.1. Calculated temperature distribution in PEF treatment chambers

Figure 2-7 shows the simulated temperature distribution in the colinear treatment chamber for the 100 µs, 1 Hz continuous pulse application protocol. In Figure 2-7, panel a, the spatial

temperature distribution in the treatment chamber at the end of the last pulse is shown. Notably, the highest temperature rise is predicted at the end of the treatment volume near the electrode edge. This hot spot is caused by the high energy received by the saline flowing through this location. Due to the parabolic flow velocity profile, the product (saline in our case) flowing near the channel walls receives a higher number of pulses, and thus more energy, than the product flowing in the center of the channel, when passing through the treatment volume. As a result, the largest temperature rise is observed for the saline flowing near the channel walls upon exiting the treatment volume. Moreover, the high electric field strength and current density around the electrode edges contribute to the energy load and consequently the temperature rise in this region. In Figure 2-7, panel b, temperature change during pulse application is evaluated at three different locations in the treatment chamber (visible in Figure Figure 2-7, panel a): i) at the hot spot at the end of the treatment volume near the electrode edge; ii) exactly in the middle of the treatment volume; and iii) at the outlet of the treatment chamber. As expected, the temperature rise at the hot spot is much greater than the temperature rise in the middle of the treatment volume. The model also predicts temperature oscillations at the hot spot and in the middle of the chamber, corresponding to the pulse repetition frequency (*f*). These temperature oscillations are, however, not present at the outlet of the treatment chamber, where temperature was measured because the outlet is further from the treatment volume where ohmic heating occurs, and the flow channel acts as a low-pass filter.

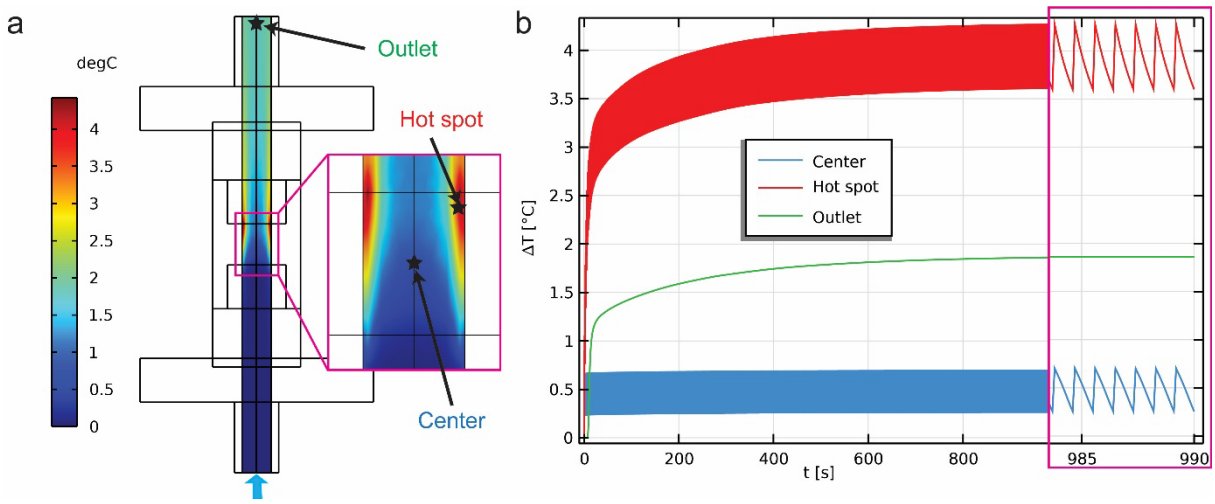

Figure 2-7: (a) Simulated temperature distribution along the longitudinal symmetry plane of the co-linear treatment chamber at the end of the last simulated pulse for the pulse protocol: continuous 100 µs, 1 Hz, U=4000 V, and F=20 ml/min. (b) Temperature change evaluated at three different locations in the chamber (Hot spot, Outlet, Center - visible in (a)) for the same pulse protocol. Figure adapted from [45].

Figure 2-8 shows the simulated temperature distribution in the parallel plate treatment chamber for the 100 µs, 1 Hz continuous pulse application protocol. As in the case of the colinear treatment chamber, the highest temperature rise is predicted at the end of the treatment volume near the electrode edge (Figure 2-8, panel a). However, the differences in temperature rise in at various locations inside the treatment chamber are smaller compared to the colinear treatment chamber. The more homogeneous spatial temperature distribution in the treatment volume of the parallel plate treatment chamber, compared to the colinear chamber can be attributed to a more homogeneous electric field distribution. Temperature oscillations can also be observed at all three evaluated locations in the chamber, including the outlet (confirmed by experiments, Figure 2-10), since the outlet is closer to the treatment volume.

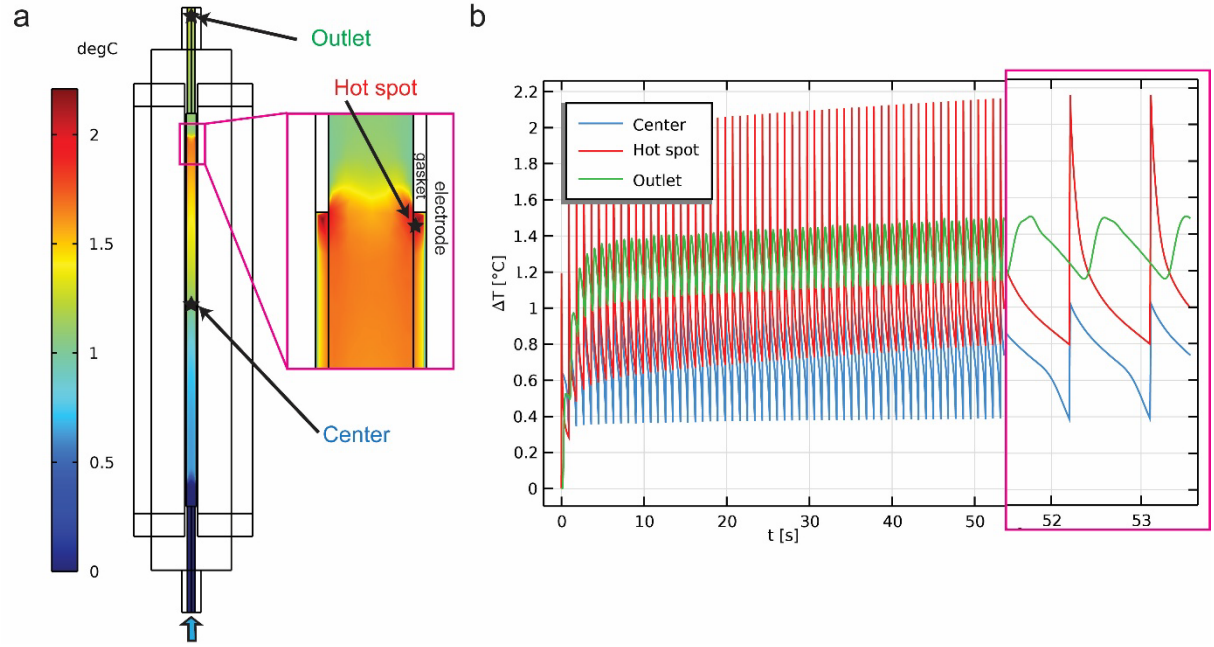

Figure 2-8: (a) Simulated temperature distribution along the longitudinal symmetry plane (through the electrodes) of the parallel plate treatment chamber at the end of the last simulated pulse for the pulse protocol: continuous 100 µs, 1 Hz, U=1000 V and F=20 ml/min. (b) Temperature change evaluated at three different locations in the chamber (Hot spot, Outlet, Center - visible in (a)) for the same pulse protocol. Figure adapted from [45].

2.3.2. Pulse-resolved model vs experiments

The newly developed pulse-resolved model was validated against experimentally measured electrical current and fluid temperature within the outlet channel of the treatment chambers during pulse application.

In the simulation, temperature was evaluated at the approximate position of the temperature sensor (within the outlet of each treatment chamber) during the experiment (Figure 2-2, red dot). Measured temperature data were first filtered with a Butterworth filter, and then the initial temperature of the solution (T_i), before pulse application, was determined from the filtered measurements (Figure 2-9). The initial temperature of the solution was used as the initial value of the temperature in the simulation, as well as the inflow temperature (section 2.3.3). For model validation, this initial temperature was subtracted from both the measured and simulated values.

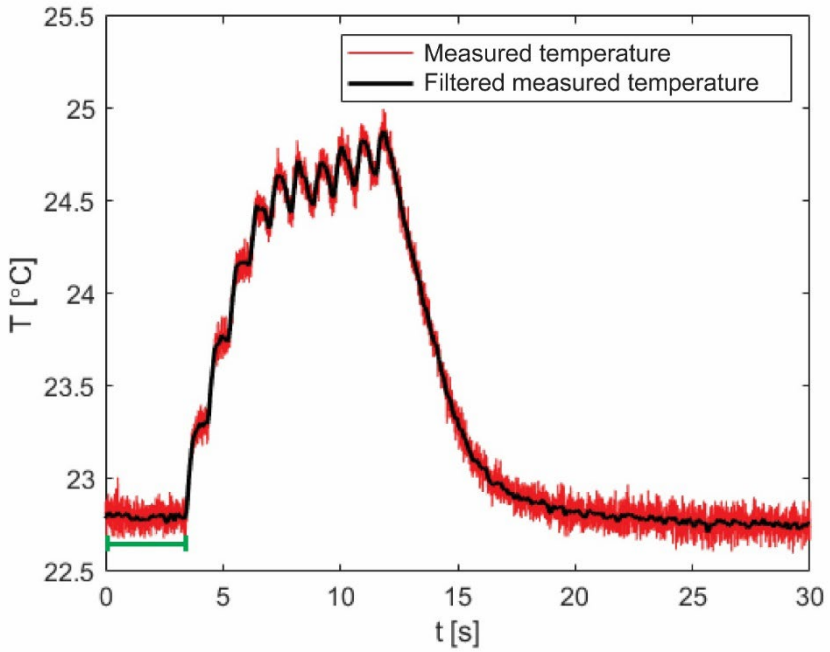

Figure 2-9: Temperature measurement within the outlet of the parallel plate treatment chamber demonstrates the difference between the raw captured temperature signal and the filtered signal with an improved signal-to-noise ratio. The segment marked in green indicates the portion of the signal used to determine the initial, pre-treatment saline temperature (T_i), by numerical averaging across the entire interval. Figure adapted from [45].

Figure 2-10 presents the measured and simulated temperature changes within the outlet of colinear and parallel plate treatment chambers for different pulse protocols.

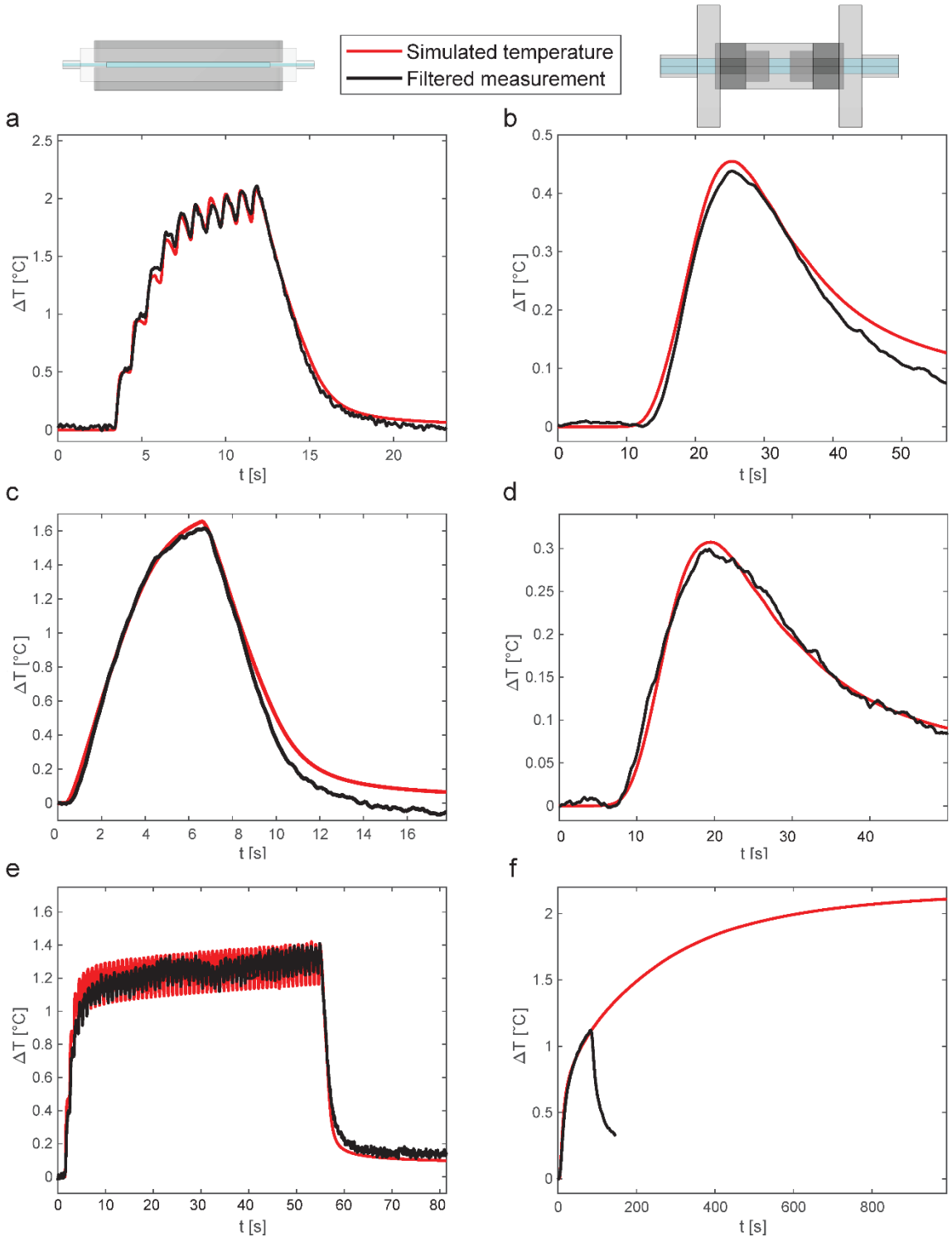

Figure 2-10: Comparison of simulated and measured temperature changes within the outlet of the parallel plate (left column) and colinear (right column) treatment chambers during pulse application for different PEF protocols: (a, b) 10x 100 µs, 1 Hz and F=10 ml min^{-1}, (c, d) 64x 10 µs, 10 Hz and F=10 ml min^{-1}, and (e, f) cont. 100 µs, 1 Hz and F=20 ml min^{-1}. Voltages used were U = 1000 V for the parallel plate chamber (left column) and U = 4000 V for the colinear chamber (right column). Note the different ranges on the x and y axes. Figure adapted from [45].

A good correlation between simulated and measured values can be observed in Figure 2-10 for all pulse protocols in both treatment chambers. For the parallel plate treatment chamber and 100 µs pulses with a 1 Hz pulse repetition frequency (panels a and e), we observe temperature oscillations in both measured and simulated data, corresponding to the pulse repetition frequency (*f*). These oscillations result from heating of the fluid during the pulse duration, causing a temperature increase, followed by a temperature decrease between pulses due to convection and conduction. The agreement between the simulated and measured temperature oscillations demonstrates the model's ability to accurately predict transient temperature variations during and between application of electrical pulses.

For the colinear treatment chamber and 100 µs pulses (panels b and f), these oscillations are not visible within the outlet due to the considerable distance between the outlet/temperature sensor and the treatment volume of the chamber. However, the model indicates that temperature oscillations are present in the treatment volume (Figure 2-7) and could be observed if the fluid temperature were measured inside the treatment volume.

In continuous pulse application, a stationary state was achieved only in the parallel plate treatment chamber (panel e). In the colinear chamber (panel f), the syringe volume was not large enough to run the experiment for a sufficient duration, so the stationary state for the colinear chamber was reached only in the simulation. Overall, good agreement between measured and simulated temperature changes within the outlet of both chambers can be observed. The average root mean square error (RMSE) between the model and measurements is 0.05 °C, and the maximum absolute error is 0.24 °C, which is below the accuracy of the temperature sensors used (± 0.3 °C). See Table 2-4 for RMSE and maximum error for each PEF protocol.

Table 2-4: Average root mean square error (RMSE) and maximum absolute error between the calculations from the model and the measurements

Treatment chamber	Pulses applied	*F* [ml/min]	*U* [V]	RMSE [°C]	Max abs error [°C]
Colinear	10 × 100 µs, 1 Hz	10	4000	0.026	0.0521
		20		0.0132	0.0234
	cont. 100 µs, 1 Hz	20		0.0286	0.0662
	64 ×10 µs, 10 Hz	10		0.0093	0.0325
		20		0.0168	0.0415
	cont. 10 µs, 10 Hz	20		0.1433	0.2414
Parallel Plate	10 × 100 µs, 1 Hz	10	1000	0.0460	0.1287
		20		0.0475	0.1629
	cont. 100 µs, 1 Hz	20		0.0601	0.2385
	64 × 10 µs, 10 Hz	10		0.08	0.1395
		20		0.0285	0.0567
	cont. 10 µs, 10 Hz	20		0.0797	0.1724

Figure 2-11 shows measured and simulated current for the parallel plate (left column) and colinear (right column) treatment chambers for a representative 10 µs and 100 µs pulses.

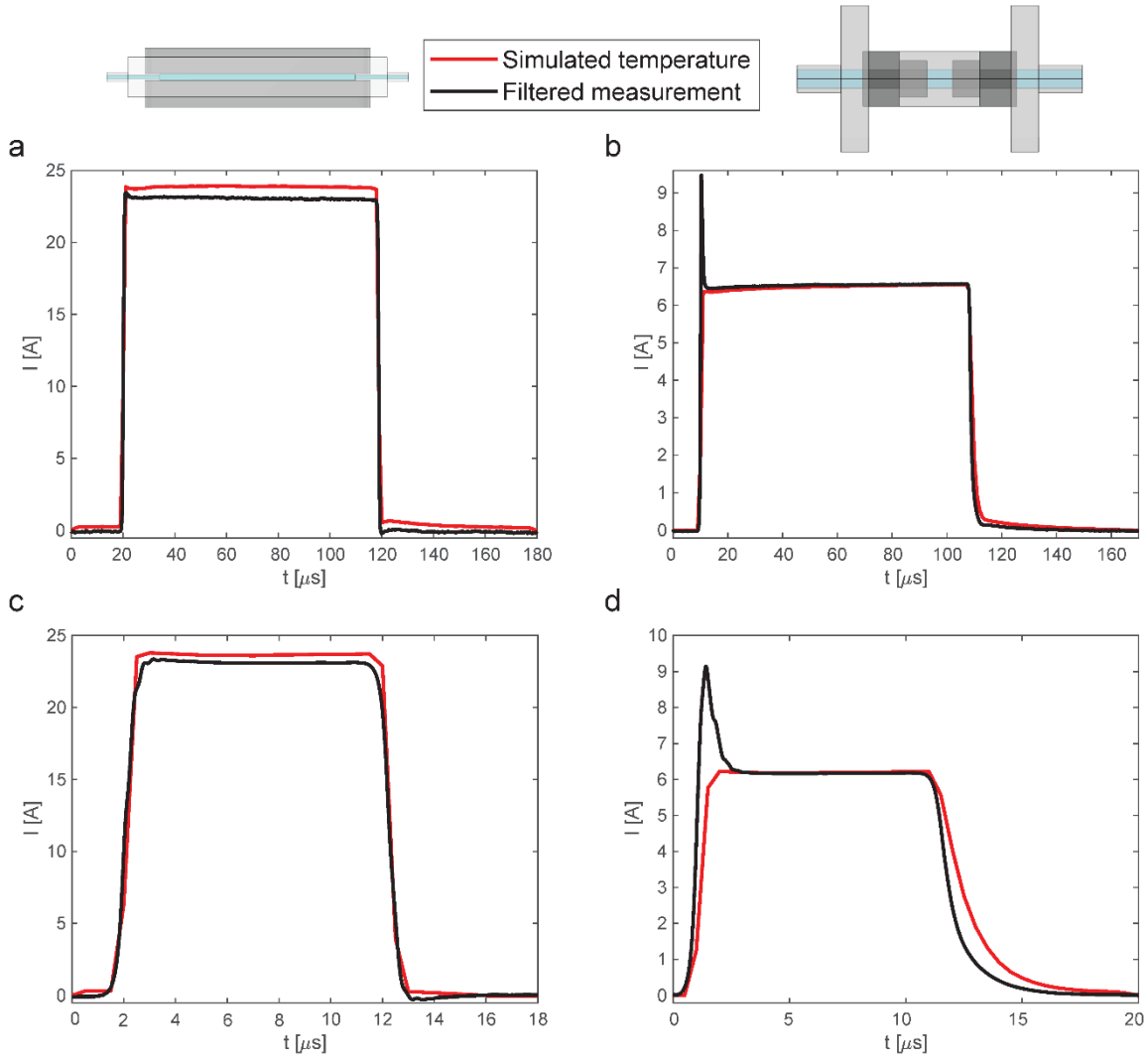

Figure 2-11: Comparison of simulated and measured electrical current for the parallel plate (left column) and colinear (right column) treatment chambers for a representative pulse from different PEF protocols: (a, b) 10x 100 µs, 1 Hz and F=10 ml/min, and (c, d) 64x 10 µs, 10 Hz and F=10 ml/min. The voltages used were U = 1000 V for the parallel plate chamber (left column) and U = 4000 V for the colinear chamber (right column). Note the different ranges on the x and y axes. Figure adapted from [45].

For the parallel plate treatment chamber, there is good agreement between the shapes of the measured and the simulated current for both 10 and 100 µs pulse durations (Figure 2-11, panels a and c). The amplitude of the simulated current is slightly higher than that of the measured current. This may be due to underestimation of the effective electrode surface area, that is, overestimation of the area of the electrodes obstructed by gaskets (Figure 2-3). The calculated RMSE between simulated and measured current for the parallel plate chamber is 0.8 A for the 100 µs pulse, and 0.7 A for the 10 µs pulse.

For the colinear chamber, there is good agreement between the amplitude of the measured and simulated current for both the 10 µs and 100 µs pulses (panels b and d). However, there is a difference in current shape: the measured current for the colinear chamber shows a current peak that is not present in the simulated current, since the numerical model does not account for the capacitive current.

Regarding the difference in the current peak (or lack thereof in the case of the parallel plate chamber) between the two types of chambers (compare panels a and b), it should be noted that the estimated capacitance of the parallel plate chamber is higher than that of the colinear chamber. Therefore, we would expect to see a larger capacitive current peak in the parallel plate chamber. However, many factors influence the capacitive current and its amplitude. First, the capacitive current equals the derivative of the voltage change over time, multiplied by the chamber capacitance. In our case, the rise time for the parallel plate chamber is almost twice as long as that for the colinear chamber. Also, the voltage amplitude is four times higher in the colinear chamber. This means the derivative of the voltage change during rise time is considerably higher in the case of the colinear treatment chamber. Second, the resistive current amplitude is about four times lower in the colinear chamber, so the capacitive current contribution is more pronounced for the colinear chamber compared to the parallel plate chamber, where it is practically absent.

An interesting detail observed in the case of the colinear chamber and the 100 µs pulse (panel b) is a small increase in current over the duration of the pulse. This occurs because heating of the fluid in the treatment volume increases the electrical conductivity of the saline, which consequently decreases the electrical resistance of the chamber.

The calculated RMSE between simulated and measured current for the colinear chamber is 0.4 A for the 100 µs pulse and 0.9 A for the 10 µs pulse.

2.3.3. Comparing pulse-resolved against duty cycle model

To compare the newly developed pulse-resolved model to the commonly employed duty cycle model, first the continuous 100 µs, 1 Hz PEF protocol used in experiments (Table 2-1), was modeled for both treatment chambers with the pulse-resolved approach (described in section 2.2.4) and the duty cycle approach (described in section 2.2.5).

2.3.3.1. PEF protocols used in experiments

Figure 2-12 shows the comparison of calculated temperatures evaluated at the three different locations for both treatment chambers and modeling approaches.

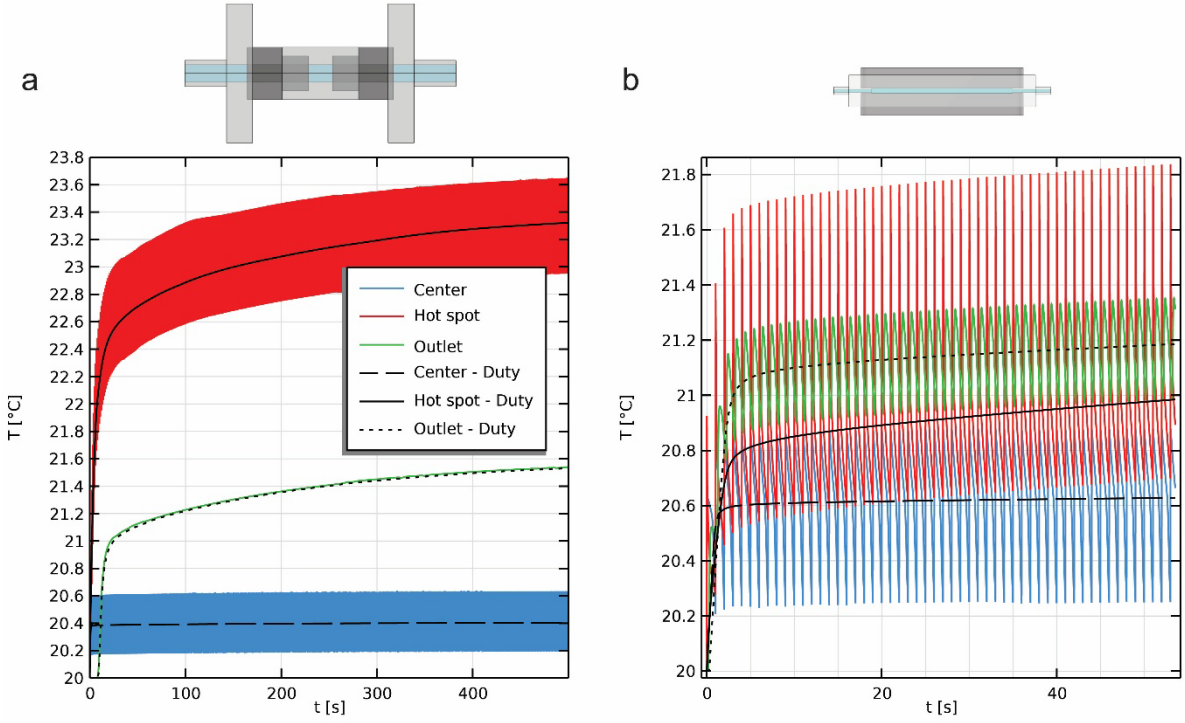

Figure 2-12: Comparison of the pulse-resolved model and the. duty cycle model. Temperatures evaluated at the three different locations in the (a) colinear and (b) parallel plate treatment chambers (Hot spot, Outlet, Center, as shown in Figure 2-7 and Figure 2-8, panel a). Pulse protocol: continuous 100 µs, 1 Hz, F = 20 ml/min, T_i=20°C and U = 1000 V (parallel plate) and U = 4000 V (colinear). Temperatures corresponding to the duty cycle model are indicated by "- Duty" in the legend. Figure adapted from [45].

Figure 2-12 shows that the duty cycle modeling approach for both treatment chambers provides a good representation of the average temperatures at different locations in the chamber. However, it smooths out the transient variations in temperature that occur during and between electrical pulses, i.e. we lose information on the peak temperature at the end of the pulse and the decrease in temperature between pulses. In the case of the outlet temperature in the colinear treatment chamber, where temperature oscillations are not present due to the large distance from the treatment volume, both modeling approaches predict comparable amplitude and temporal dynamics of the temperature rise.

2.3.3.2. Hypothetical, "higher energy" PEF protocols

To further explore and demonstrate the differences between the two modeling approaches, we calculated the temperature in the colinear treatment chamber for two hypothetical "higher energy" PEF protocols (Table 2-1, shaded in gray):

- continuous 100 µs, 1 Hz, U = 14000 V, F = 2 l/h and T_i=*20°C*
- continuous 10 µs, 10 Hz, U = 14000 V, F = 2 l/h and T_i=*20°C*

Both PEF protocols have the same treatment time (t) of 200 µs, a *VDR* of 10 kV/cm, and total specific energy input of $W_T \approx 71\ kJ/kg$, which is closer to the electric fields and energies used at the industrial scale. The only difference between the two PEF protocols is the number of pulses received by the treated product/fluid: $n = 2$ for the 1 Hz protocol and $n = 20$ for the 10 Hz pulse protocol. Since both PEF protocols have the same duty factor ($duty = \tau \cdot f = 0.0001$), we can compare the simulated temperature distribution for each protocol using the pulse-resolved approach against the same simulated temperature distribution using the duty cycle approach. The results of the comparison of the modeling approaches are shown in Figure 2-13.

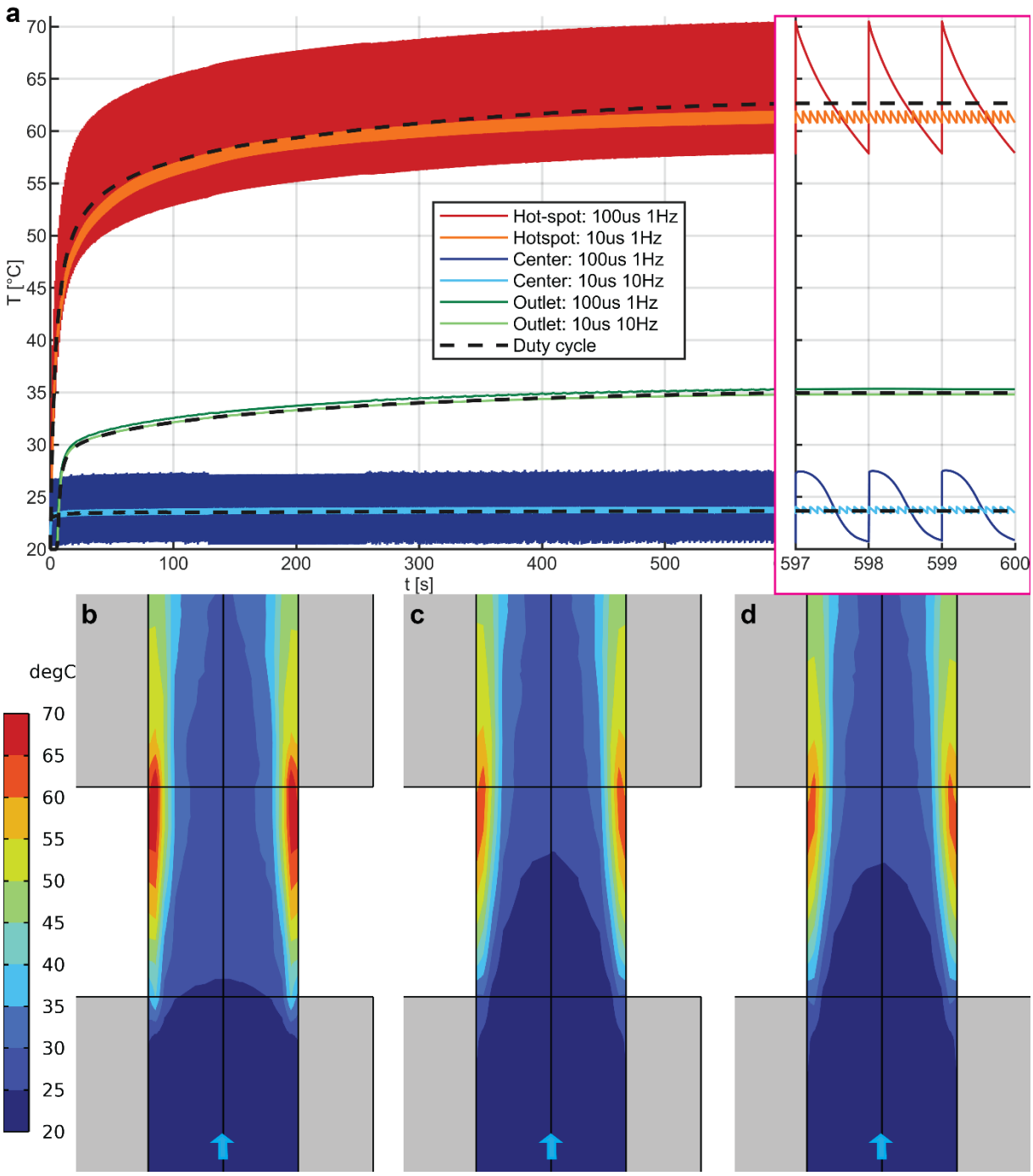

Figure 2-13: Comparison of the pulse-resolved model and the duty cycle approach. a) Simulated temperatures at the three different locations in the colinear chamber (Hot spot, Outlet, Center, as shown in Figure 2-7) for two pulse protocols: 100 µs, 1 Hz and 10 µs, 10 Hz. Solid colored lines represent the pulse-resolved model; dashed black lines represent the duty cycle model (both protocols have the same duty factor of 0.0001). The bottom row shows the spatial temperature distribution in the treatment volume of the colinear chamber at the last simulated pulse (peak temperature) for: b) the pulse-resolved model and 100 µs, 1 Hz pulse protocol, c) the duty cycle model, and d) the pulse-resolved model and 10 µs, 10 Hz pulse protocol.

Figure 2-13, panel a, shows that for the 100 µs, 1 Hz higher energy PEF protocol, the duty cycle approach provides a good representation of the average temperatures at different locations in the chamber. However, the pulse-resolved approach shows large temperature fluctuations (over 10°C peak-to-peak difference), which are not accounted for by the duty cycle approach. This is especially notable in the hot spot, where the pulse-resolved model predicts peak temperatures over 70°C, compared to the duty cycle model, which anticipates temperatures around 62°C (an 8°C difference). Interestingly for the 10 µs, 10 Hz higher energy PEF protocol, which has the same treatment time, VDR and delivered energies, the pulse-resolved approach predicts relatively small temperature fluctuations (less than 2°C peak-to-peak difference in the hot spot). For this PEF protocol the predicted temperatures that the product is exposed to in different parts of the chamber are very similar for both the pulse-resolved and duty cycle approaches.

Examining the temperature distribution in the treatment volume at the end of the last simulated pulse (Figure 2-13, panels b, c and d), we observe that for the 100 µs, 1 Hz higher energy PEF protocol the pulse-resolved approach (panel b) predicts higher temperatures compared to the duty cycle approach (panel c). However, for the 10 µs, 10 Hz higher energy PEF protocol the pulse-resolved approach (panel d) predicts almost identical temperature distribution as the duty cycle approach (panel c).

2.3.4. Particle-level exposure to electric field and temperature

Particle-level exposure was evaluated for the two hypothetical higher energy pulse protocols with the same treatment time and total energy input: 100 µs pulses at 1 Hz and 10 µs pulses at 10 Hz, each at a delivered voltage of 14 kV and a flow rate of 2 L/h (for more information see Table 2-1, protocols shaded in gray). We also compared the pulse-resolved and duty cycle approaches.

2.3.4.1. Particle velocity and residence time distribution – comparison against analytical curves

The velocity of the particles and their residence time in the treatment chamber are two important parameters that affect how many pulses and how much thermal load (energy) the particles receive (see section 2.2.3).

We calculated the velocity and residence time for an ensemble of 10 000 particles, released with velocity-weighted probability to accurately represent the entire population of cells in the treated product.

Because we used massless particles in the simulations that follow the fluid velocity streamlines precisely, and because the laminar pipe flow in the colinear chamber can be described analytically, we can compare the numerically calculated particle velocities and residence time distribution with the analytically calculated curves (described in section 2.2.6.2) to validate the particle tracing functionality in COMSOL.

Figure 2-14 compares the numerically determined histograms for particle velocity and residence time to analytically derived probability density functions (PDF) and cumulative distribution functions (CDF).

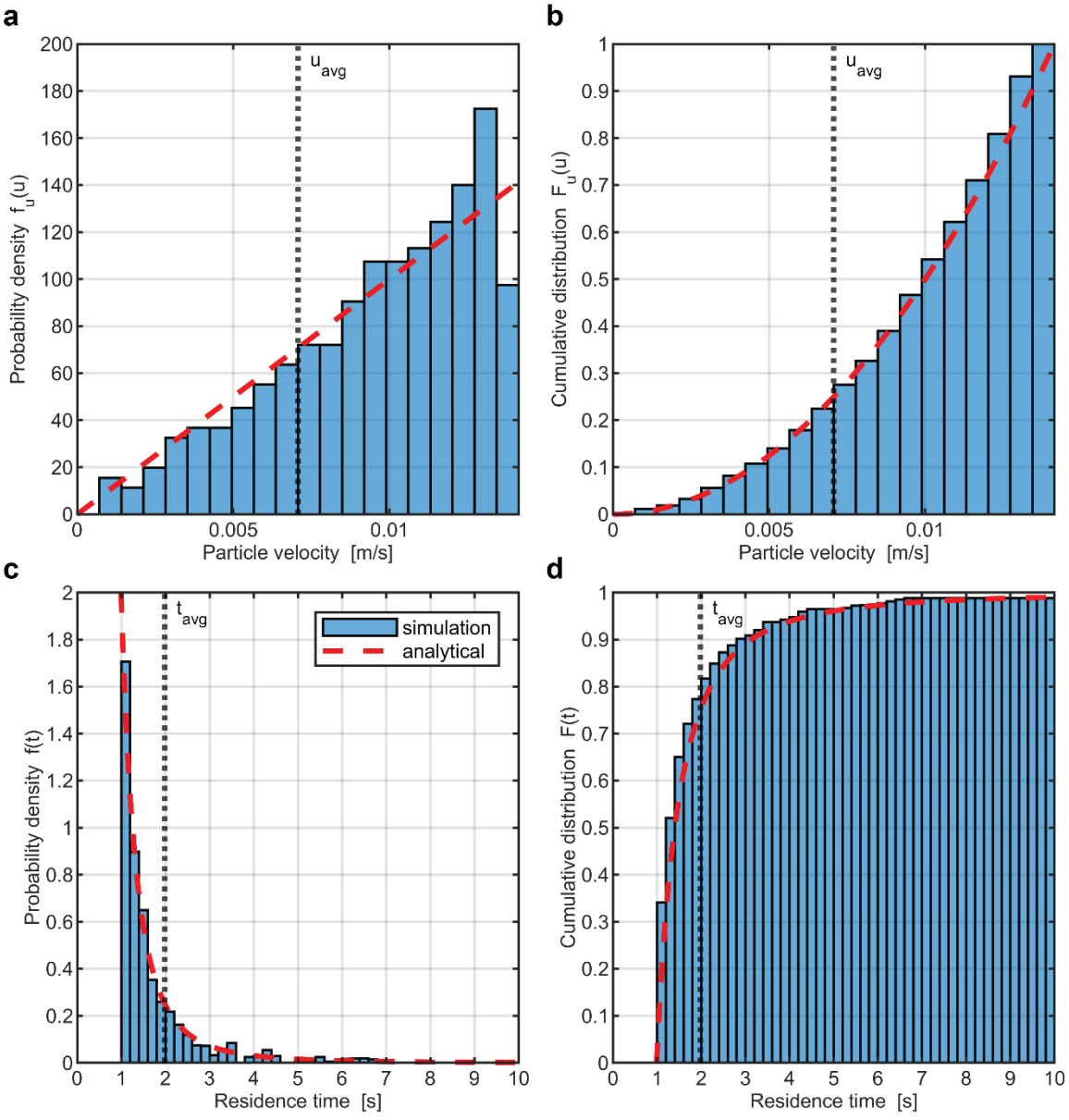

Figure 2-14: Numerically determined histograms for particle velocity (panels a and b) and residence time (panels c and d) compared to analytic PDFs/CDFs (red lines).

As shown in Figure 2-14 the numerically calculated distributions of particle velocity and residence time closely match the analytically predicted PDF and CDF curves.

The calculated average residence time of the particles was 1.89 s, which is close to the analytically calculated value of 1.98 s. The small difference is likely due to finite sampling and the imperfect mesh. From : Numerically determined histograms for particle velocity (panels a and b) and residence time (panels c and d) compared to analytic PDFs/CDFs (red lines)., panel d, we can also see that about 75 % of the particles have shorter residence times than the average residence time, which means that 75 % of the particles or cells in the treated product receive fewer pulses than indicated in Table 2-1 (protocols shaded in gray).

2.3.4.2. Exposure to electric field and temperature – representative particle trajectories

First, we evaluated particle exposure to electric fields and temperature for a few selected particle trajectories. To present representative results without showing the exposure for all 10,000 particles, we selected five trajectories defined by volumetric-flow percentiles. In fully developed laminar pipe flow, axial velocity is maximal at the centerline and decreases smoothly to zero at the wall. By integrating the volumetric flow radially outward, we identified radii at which the cumulative flow fraction reached 0 %, 50 %, 75 %, 90 %, and 99 % of the total volumetric flow (see section 2.2.6.3). A trajectory at the 90 % flow-percentile radius, for example, represents the position where 90 % of the total volumetric flow moves faster (closer to the center) and only 10 % moves more slowly (nearer the wall). Reporting the electric-field and temperature histories for these five trajectories captures the full range of possible exposures—from the shortest residence time and lowest thermal-electric load at 0 % to the longest residence time and highest cumulative dose at 99 %. Figure 2-15 shows particle exposure to electric fields and temperature for five specific particle trajectories corresponding to the 0%, 50%, 75%, 90% and 99% volumetric flow percentiles.

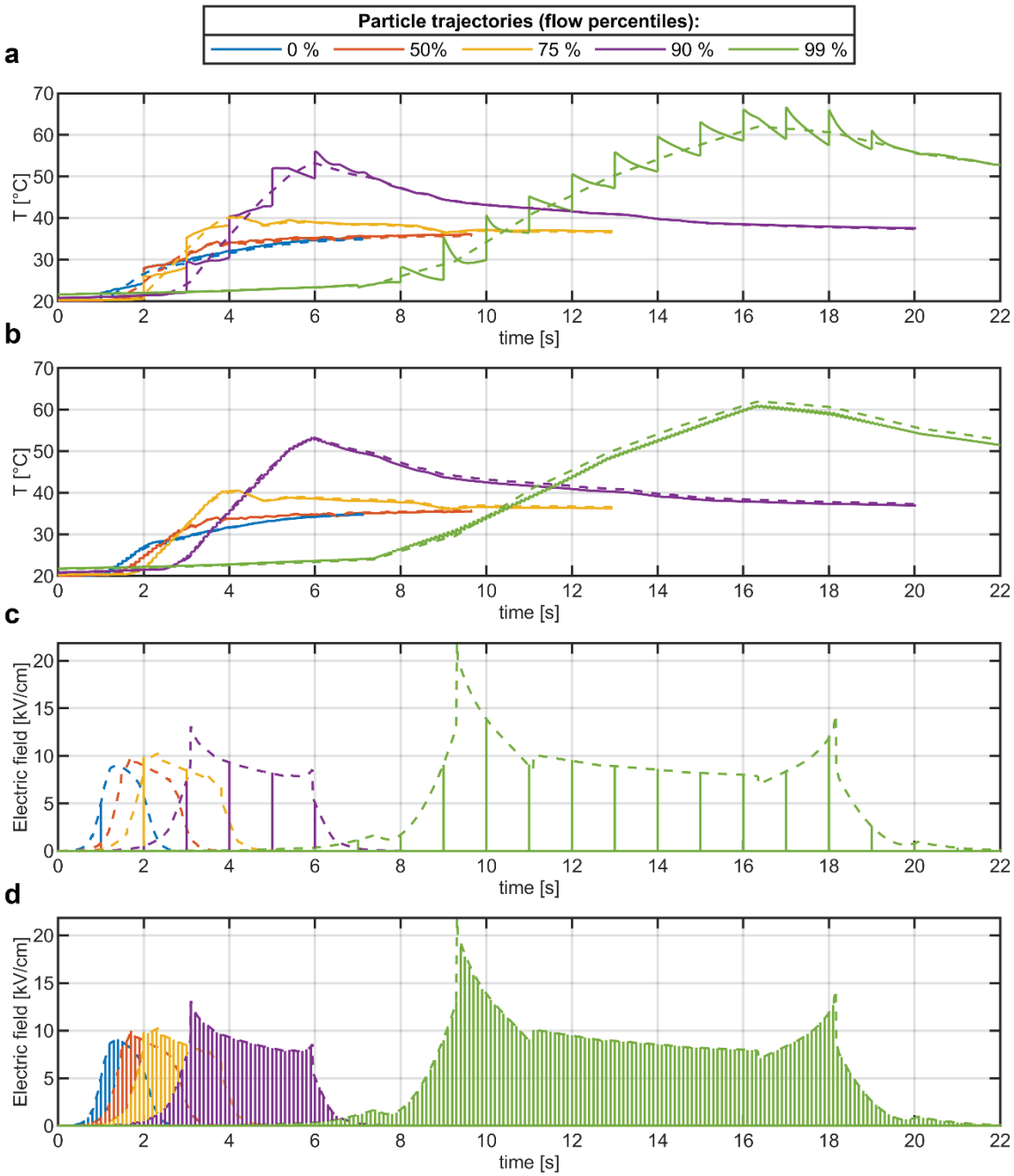

Figure 2-15: Exposure of representative particles to temperature (panels a and b) and electric field (panels c and d) while flowing through the PEF treatment chamber. Results are shown for five particle trajectories corresponding to volumetric flow percentiles (0 %, 50 %, 75 %, 90 %, and 99 %) under two pulse protocols: 100 µs pulses at 1 Hz (panels a and c) and 10 µs pulses at 10 Hz (panels b and d). Solid lines represent the pulse-resolved approach and dashed lines represent the duty-cycle approach. Higher flow percentiles correspond to slower-moving particles that are closer to the wall.

In Figure 2-15, we see that particles flowing closer to the wall (90%, and 99% flow percentile) receive substantially more pulses and are exposed to higher temperatures than particles flowing

closer to the center of the channel (0% and 50% flow percentiles). For example, the particles corresponding to the 99% flow percentile are exposed to temperatures of about 70°C, while 75% of the particles are exposed to temperatures below 40°C.

If we compare the calculated exposure of particles to temperature between the pulse-resolved modeling approach (solid lines) and the duty cycle modeling approach (dashed lines), we can again see that the duty cycle approach works well for10 μs pulses at 10 Hz, where temperature fluctuations are small/negligible.

When we compare the calculated exposure of the particles to the electric field, we see that the duty cycle approach does not capture the discrete nature of the pulse protocols, which is even more pronounced for 100 μs pulses at 1 Hz.

2.3.4.3. Exposure to electric field and temperature – population distributions

Since we can calculate the exposure to different temperatures and electric field strengths for each particle as it flows through the chamber, we can determine various metrics that can affect the efficiency and safety of the treatment. These include the maximum temperature reached by each particle and the cumulative exposure time of each particle above a certain electric field threshold (distinct from the treatment time calculated in 2.2.3), as well as the distribution of these metrics. For the duty cycle modeling approach, where the electric field is stationary, the calculated cumulative exposure time was multiplied by the duty factor to relate it to the to relate it to the pulsating electric field.

Figure 2-16 compares the distribution of maximum particle temperatures and cumulative electric field exposure times above the threshold of 5 kV/cm for the two pulse protocols (10 μs at 10 Hz and 100 μs at 1 Hz) and the two modeling approaches.

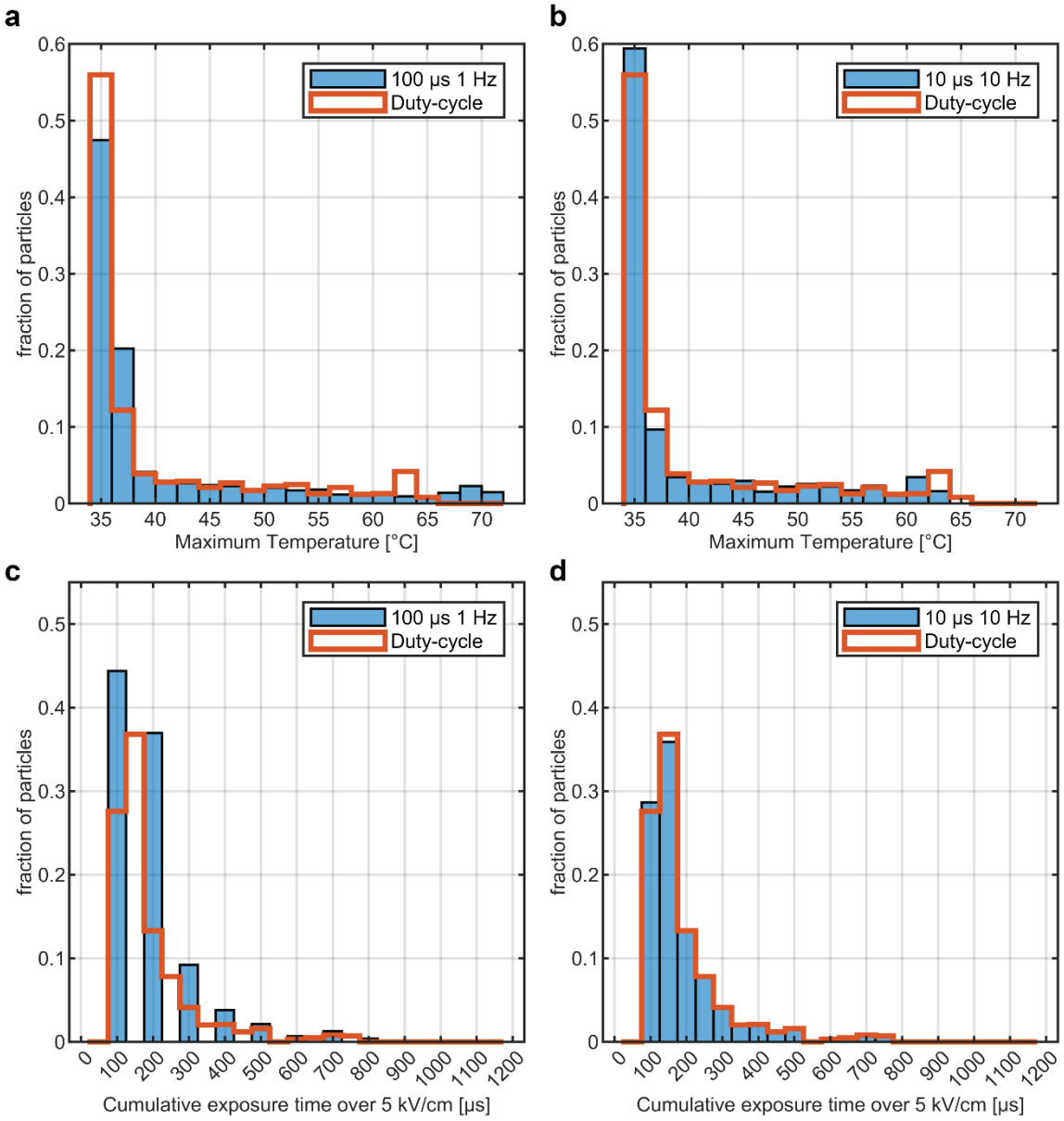

Figure 2-16: Distribution of maximum particle temperature (panels a and b) and cumulative exposure time over 5 kV/cm (panels c and d) for the 100 µs at 1 Hz (panels a and c) and 10 µs at 10 Hz (panels b and d) pulse protocols. Blue bars represent the more detailed pulse-resolved approach, and the red line represents the duty cycle approach (identical for both protocols).

When we examine the distribution of maximum particle temperature and exposure time above 5 kV/cm, we again observe significant differences in the electrical and thermal load that particles or cells experience during PEF treatment in the colinear chamber. Notably, although we report an average treatment time of 200 µs for both protocols and a VDR of 10 kV/cm in Table 2-1 (protocols shaded in gray), we find that for the 100 µs 1 Hz protocol, nearly 50% of the particles have a cumulative exposure time above 5 kV/cm of only 100 µs.

For the 10 µs at 10 Hz pulse protocol, the simplified duty cycle approach predicted particle exposure times and maximum temperature distributions very similar to those obtained with the more detailed pulse-resolved approach. However, this was not the case for the 100 µs 1 Hz pulse protocol. In this case, the duty cycle approach failed to predict the higher maximum temperatures and the discrete distribution of cumulative exposure times.

2.4. Discussion

2.4.1. Pulse-resolved model validation

The pulse-resolved numerical model was successfully validated against experiments by comparing simulated and measured fluid temperatures within the outlet channel of the treatment chambers (Figure 2-10) and simulated and measured electrical current (Figure 2-11). The model reliably predicted the amplitude and temporal dynamics of both temperature rise and electrical current during pulse application for both treatment chambers and across the different treatment protocols used in the experiments. Overall, these results provide confidence in the developed pulse-resolved model and its ability to predict temperature and electric field distribution in the treatment chamber during pulse application independent of the pulse protocol, flow parameters, and treatment chamber design.

2.4.2. Pulse resolved vs duty cycle modeling approach

The presented pulse-resolved approach to modeling temperature distribution in continuous-flow PEF treatment chambers was compared to the duty-cycle approach commonly used in the existing literature on coupled simulations of electric field, fluid flow, and heating.

For lower-energy PEF protocols used in the experiments (Figure 2-12, VDR < 3 kV/cm, W_T under 8 kJ/kg), the duty-cycle approach provides a good representation of average temperatures at various locations within the chamber. However, it smooths transient temperature fluctuations that occur during and between electrical pulses, omitting information about peak temperatures at the end of each pulse. Although these oscillations are relatively large compared to the total temperature increase, they remain small in absolute terms (<1 °C). Therefore, for such lower-energy PEF protocols, predicting temperature with the duty-cycle approach could be considered sufficient, depending on specific application requirements.

Industrial-scale PEF protocols often involve substantially higher energy inputs, electric fields, and fluid flows, resulting in significant temperature increases. To investigate the differences between modeling approaches under these higher-energy conditions, two PEF protocols more

representative of industrial applications were examined (Figure 2-13). Both protocols had the same flow rate (2 l/h), VDR (10 kV/cm), and treatment time (200 µs) resulting in the same specific energy input (71 kJ/kg), but differed only in pulse repetition frequency (1 Hz and 10 Hz) and pulse width (100 µs and 10 µs). For the 100 µs, 1 Hz pulse protocol, the pulse-resolved approach revealed substantial temperature fluctuations, exceeding 10 °C peak-to-peak in hot spots. Specifically, the pulse-resolved model predicted peak temperatures around 70 °C in hot spots, compared to approximately 62 °C predicted by the duty-cycle approach—a notable 8 °C difference. Such discrepancies could be significant, as elevated temperatures in hot spots can lead to potential thermal damage to the treated product and, in extreme cases, local boiling of the medium, resulting in electrode fouling, oxidation, dissolution (etching), and arcing [58]. This would negatively affect product quality and reduce the durability and lifetime of electrodes, chambers, and pulse generators. In contrast, for 10 µs, 10 Hz pulse protocol, the pulse-resolved approach predicted only minor temperature oscillations (below 2°C in hot spots), and both modeling approaches showed good agreement in predicted temporal and spatial temperature distribution (Figure 2-13).

The comparison shows that the magnitude of temperature fluctuations during PEF treatment depends not only on the total energy input (W_T) but also on the pulse width and repetition frequency, which together with flow rates significantly affect the number of pulses received by the product (n) and energy per pulse (W). More specifically, a higher number of pulses received by the product and lower energy per pulse reduce temperature fluctuations at the same delivered energy. Since the duty cycle approach/simplification averages out the temperature fluctuations, for PEF protocols where temperature fluctuations are small, i.e., a large number of pulses received by the product (high pulse repetition frequency relative to flow velocities) and low energy per pulse (short pulse duration), the duty cycle approach is sufficient for describing temperature distribution even if the total delivered energies are high.

From a computational standpoint, simulation times for the duty-cycle approach were approximately three times shorter than those for the pulse resolved approach. Additionally, duty-cycle simulation times could be further reduced by increasing the time-step size without loss of relevant temperature information, which is advantageous for initial feasibility studies or extensive parametric explorations.

2.4.3. Particle-level exposure to electric field and temperature

The particle-level exposure analysis can be used as an extension of both the pulse-resolved model and the more commonly employed duty-cycle model. We first applied this analysis to the colinear treatment chamber, where fully developed laminar pipe flow allows analytical expressions for velocity and residence-time distributions. The strong agreement between our numerically obtained histograms and the analytical curves, as shown in : Numerically determined histograms for particle velocity (panels a and b) and residence time (panels c and d) compared to analytic PDFs/CDFs (red lines)., serves as a reasonable implementation check of the particle tracing setup and paves the way for future studies on more complex geometries.

Standard PEF parameters, such as those recommended for reporting in [55], provide a basic description of the process through metrics like total specific energy input, average treatment time, and electric-field strength. Numerical modeling of the electric-field and temperature distribution then adds important spatial context (for example, indicating were higher fields or temperatures occur within the chamber). However, neither of these approaches can fully indicate how fluid flow, electric field and temperature inhomogeneities translate into the exposures actually experienced by the moving product, particles or cells. The particle-level exposure analysis directly addresses this gap. By tracing particles through the simulated flow and sampling their electric-field and temperature histories, it allows us to derive key exposure metrics, such as the maximum temperature reached by each particle and the cumulative time spent above an electric-field threshold. Most importantly, it reveals the full statistical distribution of these exposures across the entire particle population.

These distributions provide direct insight into treatment homogeneity and could be essential for assessing practical PEF treatment outcomes:

- **Treatment Efficacy** (Microbial Inactivation): The primary goal of PEF is to ensure that the vast majority of microorganisms receive an electrical dose sufficient for inactivation. Our analysis of the cumulative exposure time (Figure 2-16, panels c and d) provides a direct measure of this. For instance, for the 100 µs, 1 Hz protocol, we observe that nearly 50% of particles experience a cumulative exposure time over 5 kV/cm of only 100 µs, while the reported average treatment time is 200 µs and the reported VDR is 10 kV/cm. Such a large under-treated fraction could lead to incomplete

microbial inactivation and compromise food safety, a critical insight that commonly reported PEF treatment parameters would obscure.

- **Product Quality**: The "non-thermal" advantage of PEF is only maintained if temperatures remain below a degradation threshold. The calculated distribution of maximum particle temperatures (Figure 2-16, panels a and b) quantifies this risk directly, allowing for a precise evaluation of the fraction of the product that could be thermally damaged.

This particle-level exposure analysis also further clarifies the comparison between the pulse-resolved and duty-cycle modeling approaches. Consistent with the discussion in section 2.4.2, the duty-cycle approach (approximation) smooths transient temperature fluctuations and can thus underestimate the maximum temperatures to which the particle is exposed to, especially for longer, low-frequency pulses. For the 100 µs, 1 Hz protocol, the pulse-resolved model shows higher maximum temperatures and a more discrete distribution of cumulative exposure times, which the duty-cycle approach does not accurately capture, whereas for the 10 µs, 10 Hz protocol both approaches produce very similar exposure statistics.

Looking forward, this particle-level exposure analysis framework can be used as a powerful *in silico* tool for optimizing the PEF process. For example, we could computationally test modifications to chamber geometry, pulse protocols, or flow rates with the specific goal of narrowing the exposure distributions. The ability to simulate how these changes affect the treatment of the entire particle population provides a clear pathway to designing more robust and efficient PEF systems that maximize treatment uniformity, ensuring both safety and quality.

2.4.4. Limitations

Due to equipment limitations (syringe pump, pulse generator) we did not perform pulse-resolved model validation for the higher energy PEF protocol. Therefore, the modeling study presented in subsection 2.3.3.2 should be understood as purely an *in silico*-study. Although this protocol falls outside the range of PEF parameters within which we validated our model, we believe the results of the calculations can still be considered reasonably accurate, since the physics and boundary conditions used in the validated model (described in section 2.2.4) are still applicable. Flow can still be considered laminar (Re = 71), calculated temperatures in the treatment volume are within the range of the temperature-dependent electrical conductivity model of the saline solution, and a pulse protocol with the same pulse width and frequency as

validated in our study was used. We also checked the validity of the thermal insulation boundary condition at the treatment chamber surface by testing whether natural convection affects the temperature in the fluid volume, and simulation results showed its contribution to be negligible, at least for the observed simulation times.

Regarding the pulse-resolved modeling approach, the main limitation is the computational intensity of the model, which results in long simulation times compared to the duty cycle approach. This can become problematic if we are interested in reaching the stationary state in simulations that require many pulses, or in cases of more complex treatment chamber geometries or large parametric studies.

For particle-level exposure analysis, direct experimental validation of the predicted exposure metrics is inherently challenging and has not yet been performed. However, to build confidence in the numerical approach, the particle tracing method was first verified for the colinear chamber. For the colinear chamber, the model's simulated particle velocity and residence-time distributions showed excellent agreement with analytical solutions for laminar pipe flow, providing confidence in the accuracy of the particle tracing method. A second limitation of the current implementation is the massless particle assumption (no inertia or electrophoretic drift). This approximation is appropriate for cell-sized particles in laminar flow but may not hold for larger particles or in different flow regimes.

2.5. Conclusions

The presented pulse-resolved model of temperature distribution in a continuous flow PEF treatment chamber shows good agreement with experimentally measured electric current and temperature for both treatment chambers and different PEF protocols. This indicates a successful validation of the model and demonstrates its potential for use independent of pulse protocol, flow parameters, and treatment chamber design (geometry, etc.).

The new modeling approach simulates each electrical pulse separately, using either the experimentally measured voltage waveform or ideal square-shaped pulses. This allows analysis of the electrical current, electric field, and temperature distribution in the chamber during, at the end of, and between the application of electrical pulses. Using experimentally measured voltage in the model makes it possible to accurately simulate irregularly shaped electrical pulses with longer rise and fall times.

The pulse-resolved modeling approach provides insight into temperature fluctuations at different spatial locations in the chamber caused by the delivery of pulsed field energy, which are not accounted for in the duty cycle approach. These temperature fluctuations can be considered noteworthy, depending on the PEF protocol. The pulse-resolved modeling approach thus enables more accurate estimation of over- or under-treatment.

In this study, we also introduced particle-level exposure analysis, an extension applicable to both pulse-resolved and the more common duty-cycle models. By calculating the statistical distribution of electric field and temperature exposures for the entire particle population, the analysis provides detailed information on PEF treatment homogeneity. The resulting particle exposure metrics and their distributions can offer an important link to actual PEF treatment outcomes, such as microbial inactivation rates and changes in product quality. Particle-level exposure analysis can therefore serve as a valuable tool for comparing the effects of different chamber geometries, flow rates, and pulse protocols on treatment uniformity, and for building stronger connections between simulation and experimental results.

3. Model of bubble formation during intracardiac pulsed field ablation (PFA)

This chapter addresses the second aim of the thesis. Specifically, it presents a numerical model of electric field and temperature distribution around an ablation catheter in a saline solution, which was used to study heating and possible thermal mechanisms of microbubble formation during intracardiac PFA for different pulse protocols.

The model was developed as part of a larger *in vitro* study published in a peer-reviewed journal [46], in which we examined the effects of different pulse protocols and electrode geometries on the mechanisms of bubble formation and provided key insights for improving the safety of PFA treatment.

3.1. Background

The release of gaseous bubbles during intracorporeal application of electroporation has been previously observed and reported in biomedical applications such as electrochemotherapy [59] and irreversible electroporation [60], raising safety concerns for pulsed field ablation (PFA) when used to treat cardiac arrhythmias [61]. With the rapidly increasing use and adoption of PFA, this issue must be considered. Moreover, as demonstrated for radiofrequency ablation (RFA), heating at the catheter-blood interface can cause gas bubble and coagulum formation that may enter the bloodstream and reach organs such as the kidneys, lungs, or brain, potentially resulting in coronary occlusion, stroke, or silent cerebral events [62], [63].

Bubble formation during PFA can result from both electrochemical and thermal processes occurring near the electrode surface. Charge transfer between the electrodes and the surrounding medium is often unavoidably associated with the application of electrical pulses used to achieve electroporation, leading to redox reactions at the electrodes. If the duration of a single pulse phase is sufficient, the double-layer capacitance can become fully charged, allowing subsequent faradaic charge transfer between the medium and the electrodes. This results in electrolysis, producing gaseous products such as hydrogen, oxygen, and chlorine (when pulses are delivered to an aqueous NaCl solution). In addition, high-voltage and high pulse-number protocols commonly used to achieve ablation with irreversible electroporation can cause significant ohmic heating, resulting in a rapid local temperature rise that may reach the boiling point of water and lead to boiling or degassing of dissolved gases.

Accordingly, three main mechanisms of bubble formation and growth can be identified:

- **Degassing** - release of gas due to lower gas solubility at elevated temperatures of the medium
- **Boiling** - release of gas as water vapor
- **Electrolysis** - release of gas as a product of hydrolysis (water electrolysis at the electrodes) and oxidation of chlorine ions.

The first two mechanisms are thermal, while the third is electrochemical.

To elucidate the complex interplay between treatment parameters, electrode geometry, and bubble formation during intracardiac PFA, we conducted a comprehensive *in vitro* study involving pulsed field delivery into saline [46]. Multiple pulse protocols, two distinct electrode geometries (parallel needle electrodes and a modified RF catheter), two complementary imaging systems (a microscopic camera and a high-speed camera) and an ultrasound-based bubble-loop flow setup to measure bubble quantities and volumes capable of detaching from the catheter and persisting in circulation were employed.

To specifically investigate the thermal mechanisms of bubble formation during intracardiac PFA, we developed a numerical model of a bipolar ablation catheter immersed in saline (mimicking the high-speed camera experiments) that can accurately predict the spatial and temporal temperature distribution and potential boiling during high-voltage pulse application, thereby enabling a detailed examination of boiling and degassing contributions.

The following chapter focuses on the numerical model - its formulation, and the insights it provides by comparing predicted spatial and temporal temperature distributions and calculated contributions of boiling and degassing with observations from high-speed camera recordings - revealing how specific PFA parameters (waveform polarity, duty cycle, electrode geometry) can affect bubble formation during intracardiac PFA.

3.2. Methods

3.2.1. Pulse protocols

In the high-speed camera experiments and numerical model, we used 5 different pulse protocols selected based on the literature. These included both monophasic and biphasic pulses, with varying pulse lengths and inter-pulse delays, thereby altering the duty cycle of the pulse train and the amount of electrical energy delivered. All protocols are listed in Table 3-1, while Figure

3-1 illustrates the nomenclature used to describe the pulse waveforms presented in the table. In addition, we varied the applied voltages and initial saline temperature in the experiments.

Table 3-1: Pulse protocols used in high-speed camera experiments. The pulses are illustrated in Figure 3-1

Protocol name / shorthand	**Positive phase duration [µs]**	**Pause between phases [µs]**	**Negative phase duration [µs]**	**Pause between pulses [µs]**	**Number of pulses in burst (p_N)**	**Number of bursts (G_N)**	**Duration of one pulse train [ms]**	**Duty factor**	**References**
5 kHz monophasic 100 µs – anode on tip "100-100"	100	—	—	100	8	1	1.5	0.5	[64]
5 kHz monophasic 100 µs – reversed polarity, cathode on tip "reversed 100-100"	100	—	—	100	8	1	1.5	0.5	[64]
High duty factor biphasic "2-2-2-2"	2	2	2	2	216	1	1.73	0.5	[65]
Low duty factor biphasic "2-2-2-500"	2	2	2	500	216	1	109	0.008	Original
Low duty factor biphasic – longer pulses "5-5-5-500"	5	5	5	500	80	1	41.2	0.019	[66]

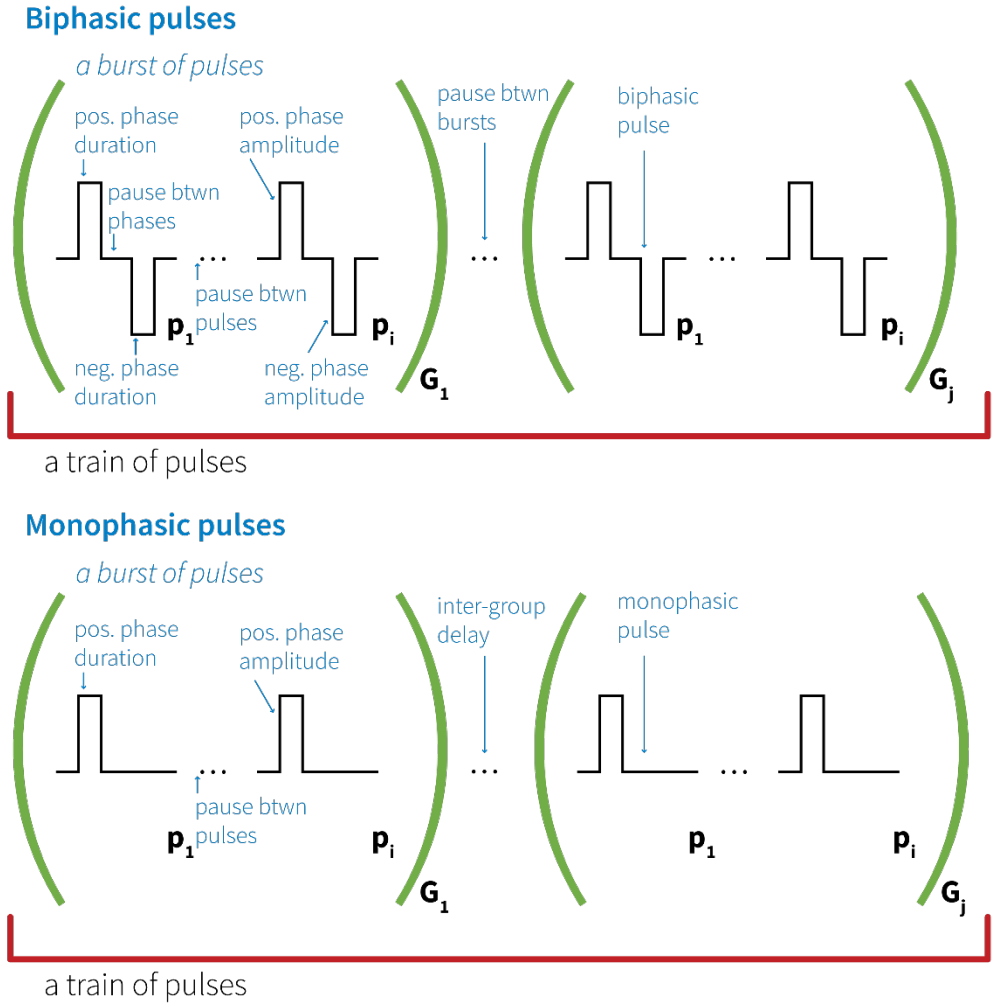

Figure 3-1: Schematic nomenclature illustrating pulse waveforms listed in Table 3-1. Figure adapted from [46].

3.2.2. High-speed camera experiments

High-speed camera experiments were conducted at the THELMA laboratory of the Reactor Engineering Division at Jožef Stefan Institute. A Phantom v1212 high-speed camera (Vision Research, Wayne, NJ, USA) equipped with a Laowa 25 mm f/2.8 2.5–5x Ultra Macro lens (Venus Optics, Hefei, China) was used with a 3:1 magnification. To achieve optimal depth of field, the camera aperture was set to f/16.

Videos were recorded at a frame rate of 10,000 frames per second. Synchronization of the video recordings with electric pulses was managed via a TTL pulse triggered by the measurement oscilloscope. Illumination was enhanced using a white LED back panel supplemented by an additional flexible 6 W LED light source (Kern OZB-A4515, KERN & SOHN GmbH,

Balingen-Frommern, Germany). The exposure duration for each frame was consistently maintained at 98 μs.

The experiments used a modified ContactR catheter (Medtronic, Minneapolis, MN, USA) with a 5-mm tip. Modifications enabled bipolar pulse delivery between the catheter tip and the three integrated ring electrodes typically used for intracardiac electrogram measurements. Figure 3-2 shows both the experimental setup and the detailed schematic of the modified catheter.

The catheter was immersed in a 200 mL beaker filled with a diluted saline solution (0.45% concentration, achieved by mixing physiological saline of 0.9% with deionized water). This reduced saline concentration more closely replicated the conductivity characteristics of blood, ensuring realistic electric current densities comparable to clinical scenarios. The catheter was intentionally positioned closer to the camera lens, within its optimal working distance, rather than being centered in the beaker.

During pulse deliveries, voltage and current were measured using a HDO6104A-MS oscilloscope with HVD3206A differential voltage probe and CP31A current probe (all from Teledyne LeCroy, Chestnut Ridge, NY, USA).

The temperature near the electrode surface was continuously monitored using an optical sensor (within 1 mm of the electrode) connected to an OpSens PSC-D-N optical thermometer equipped with a single PSR-G1-10-100ST module and an OTG-MPK5 fiber-optic temperature probe (OpSens Solutions Inc., Canada).

To assess the influence of reduced gas solubility at elevated temperatures on bubble formation, experiments were conducted at various initial solution temperatures. The saline temperature was adjusted by heating with a hot plate or cooling in an ice bath, in both cases combined with magnetic stirring using a standard laboratory hot-plate stirrer or an ice pack to ensure uniform temperature distribution.

Bubble volumes were quantified using ImageJ software [67], with calibration based on known dimensions of the catheter and direct measurements of bubble diameters.

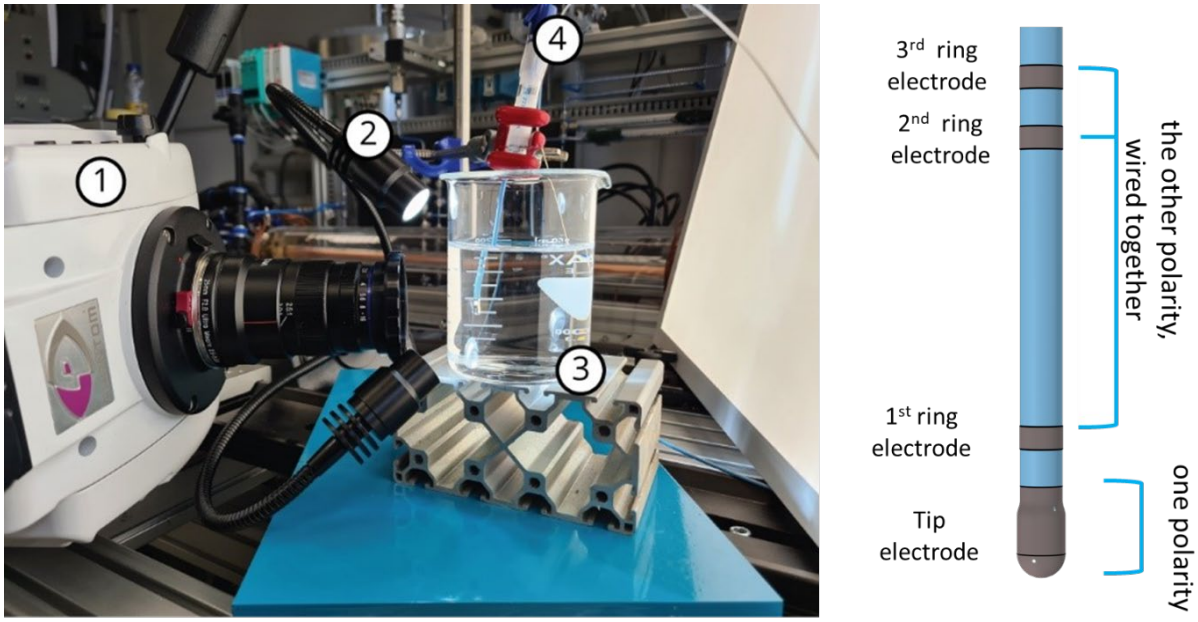

Figure 3-2: High-speed camera experiments. Left: Photograph of the experimental setup with the high-speed camera. Right: Schematic illustration of the ContactR catheter modified for bipolar pulse delivery. Figure adapted from [46].

3.2.3. Numerical model

The numerical model was created in COMSOL Multiphysics (Version 6.1, COMSOL AB, Stockholm, Sweden).

3.2.3.1. Geometry

The model geometry was based on the fast-speed camera experimental setup. An axisymmetric 2-D numerical model of the bipolar ablation catheter immersed in saline was built with the axis of symmetry along the long axis of the catheter. The ablation catheter geometry was constructed based on direct measurements of the catheter and drawings provided by Medtronic.

3.2.3.2. Electric field distribution

The electric field distribution was obtained by solving the charge conservation equation (*3.1*):

$$\nabla \cdot (\sigma \nabla V) = 0 \qquad 3.1$$

where V is the electric potential and σ is the electrical conductivity.

An electric potential boundary condition was applied at the electrodes of the ablation catheter. The voltage at the ring electrodes was set to zero, and the voltage at the tip electrode was set to the average delivered voltage ($\mathbf{U_{avg}}$, Table 3-2) for the specific high-speed camera experiment. At all other boundaries, electric insulation (i.e., zero normal electric current through the

boundary) was specified as a boundary condition. A 5% voltage drop at the ablation catheter electrode was considered to account for voltage loss in the catheter's internal wire resistance.

3.2.3.3. Temperature distribution

To model the temperature increase during pulse application, the Heat Transfer in Solids and Fluids interface in COMSOL was used, where the heat equation (*3.2*) for conservation of energy was solved in a coupled time dependent study:

$$\rho c_P \left(\frac{\partial T}{\partial t} + \boldsymbol{u} \cdot \nabla T\right) - \nabla \cdot (k \nabla T) - Q = 0 \qquad 3.2$$

where ρ is the density, c_P is the heat capacity at constant pressure, k is the thermal conductivity, $\boldsymbol{u}$ is the fluid velocity field and Q is the heat source. In the simulations, the convective term of the heat equation was neglected, as no external flow was present in the experiments and natural convection effects are expected to be negligible over the short time scales of the applied pulse trains.

The heat source (Q) was defined as follows:

$$Q = \text{ONOFF} \cdot \text{duty} \cdot Q_{ec} = \text{ONOFF} \cdot \text{duty} \cdot \sigma(T) E^2 \qquad 3.3$$

Ohmic heating (Q_{ec}) is proportional to the electrical conductivity (σ) and the square of electric field distribution ($\boldsymbol{E}$) and is active only during the application of the pulse train. The electric field distribution ($\boldsymbol{E}$) was obtained by solving the charge conservation equation (*3.1*) in the same time-dependent study (bidirectionally coupled). When solving the charge conservation equation, a constant (instead of time-dependent) electric potential boundary condition was applied to the ablation electrode to reduce computational complexity. To relate the steady ohmic heating source to a pulsating one, the ohmic heating source was multiplied by the duty factor of the PFA waveform ($duty$) to accurately model the heating during the pulse train. Duty factors for the pulse protocols used in this study are reported in Table 3-1.To accurately model the start and end of the applied pulse train, the heating source was multiplied by the $ONOFF$ variable, which was switched ON ($ONOFF = 1$) at the start of the pulse train and OFF ($ONOFF = 0$) at the end of the pulse train. This was implemented using the Events interface in COMSOL, which forces the solver to take additional time steps and reinitialize the dependent variables ($ONOFF$ and T) at the specified event times (start and end of the pulse train).

The initial temperature of the entire model was set to the measured initial temperature of the saline solution (**T_0**, *Table 3-2*). On the outer surface of the model, a thermal insulation boundary condition was used (no heat flux across the boundary).

3.2.3.4. Phase change – Boiling

Since the models showed that the temperatures of the saline were above 100°C for some pulse protocols, boiling of the solution was included in the model. For saline temperatures between 100 and 110°C, a Heaviside phase transition function was incorporated to account for the latent heat of vaporization. The actual generation of bubbles was not included in the model, as this is an ongoing area of research and model validation is still ongoing [65]. Also, unlike most boiling research, which focuses on the boiling of water at the surface of a heated wall, in our case, the water is heated directly due to Joule losses, and the metal electrodes are heated only indirectly through contact with the heated liquid medium. Since we did not model bubble generation, that is, we did not account for the volume increase during phase change (a factor of approximately 1600), the density of the NaCl solution was kept constant during the phase change to satisfy mass conservation in the model.

3.2.3.5. Material properties

To model the NaCl solution, thermal conductivity, the thermal capacity, and density of water were used. The temperature-dependent electrical conductivity for a 0.45% NaCl solution was calculated using the model described in [68]. For the gas phase of the NaCl solution, the thermal conductivity and the thermal capacity of water vapor were used. For the electrical conductivity of the medium, electrical conductivity of 0.45% NaCl solution above 100°C was reduced by 66% to account for the maximum void fraction of close random packing of spherical voids due to vapor formation [69].

The temperature-dependent material properties for the Pt/Ir electrodes were taken from the COMSOL Material Library for Platinum (solid), with the thermal conductivity being adjusted based on the values reported in [70]. For the specific values see Table 4-1.

3.2.3.6. Finite element mesh

The goal of the model was to accurately simulate resistive heating and the temperature of the fluid near the electrode edges, where bubble formation is concentrated. The amount of resistive heating near the electrode rim is proportional to the electrical conductivity and the square of the electric field strength in this region (equation *3.3*).To accurately model resistive heating and

temperatures around the electrode edges, we must model the electric field strength in this region as accurately as possible. To this end, a mesh convergence study was performed for the maximum calculated electric field strength around the electrode edge. Automatic mesh refinement was performed using the local adaptive algorithm in COMSOL. The final model mesh consisted of approximately 6600 triangular elements, resulting in 22379 degrees of freedom (DOF).

It is important to note that the electric field strength, which is the gradient of the electric potential, is theoretically infinite at a sharp edge. This makes it impossible to achieve mesh convergence, since the electric field strength diverges to infinity as the mesh is refined. Because there are no perfectly sharp edges in a realistic geometry, a small radius (~5 µm) was used at the electrode edges of the ablation catheter, resulting in reliable convergence of the maximum electric field strength in the model. Figure 3-3 shows the finite element mesh around the slightly modified sharp electrode edges and the results of the mesh refinement study.

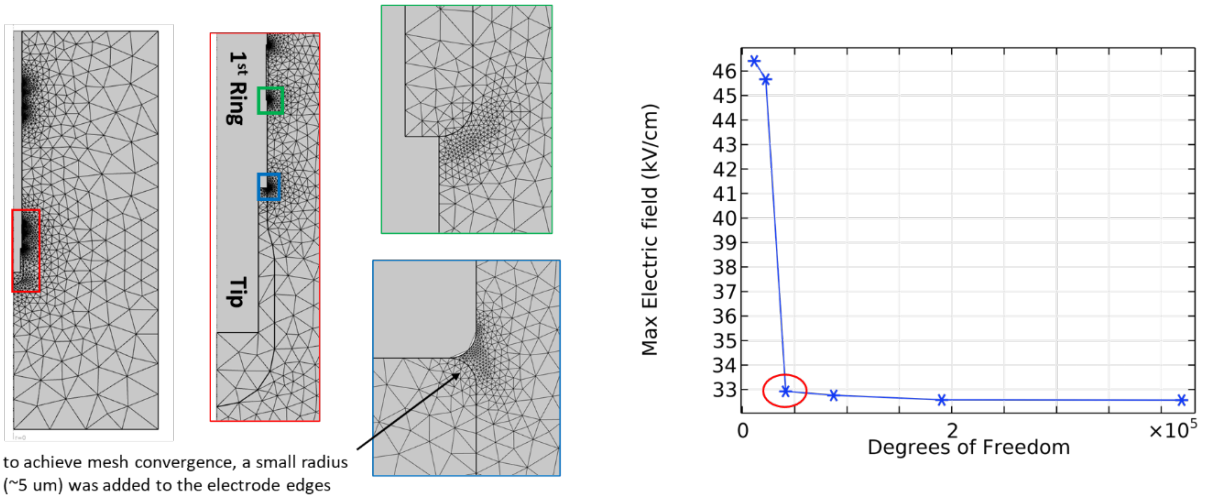

Figure 3-3: Improving the finite element mesh around the sharp electrode edges. On the left, we see finite element mesh with increasingly finer triangular elements around the sharp electrode edges, where a small fillet radius was added. On the right, we see the results of the mesh refinement study, with the red circle denoting the mesh used in the final model.

3.3. Results

3.3.1. Model output

3.3.1.1. Electric field and temperature distribution

The numerical model provides spatial and temporal electric field and temperature distributions around the bipolar PFA catheter (Figure 3-4) for different pulse protocols, delivered energies,

and initial saline temperatures. The model predicts large temperature increases near the edges of the electrodes, which correspond to the locations where bubble formation is observed in the high-speed camera recordings. This is expected, as heating results from Joule losses in the saline solution and current densities are highest around the sharp electrode edges. However, the most pronounced temperature rise occurs at the leading edge of the first ring electrode, which also corresponds to the area with the most bubble formation. This can be attributed to the small distance between the tip and the first ring electrode (2 mm), along with the larger surface area of the tip electrode compared to the ring electrodes.

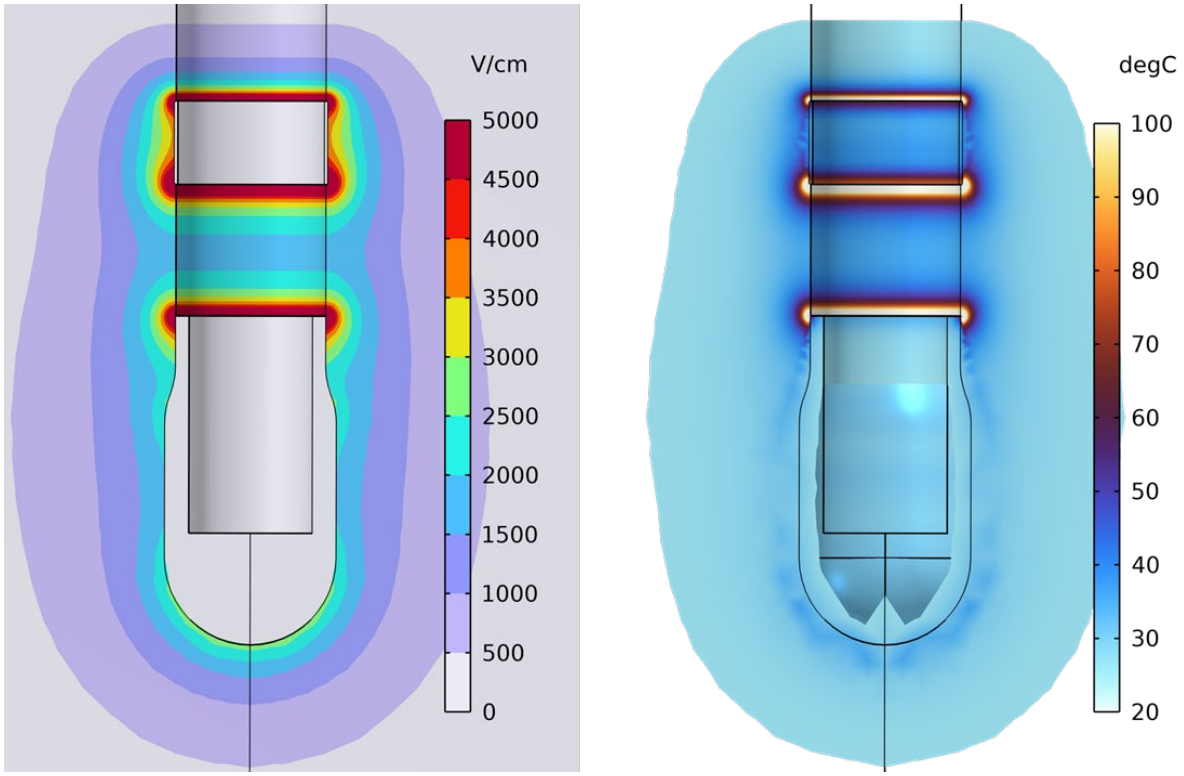

Figure 3-4: Left: Simulated electric field distribution at the start of the pulse train. Right: Simulated temperature distribution at the end of the pulse train, showing only regions with a temperature increase of at least 1 °C. Results correspond to the high-duty-factor biphasic protocol (2-2-2-500) at room temperature (26.5 °C) with an average applied voltage of 734 V (shaded gray in Table 3-2).

With the numerical model, we can calculate the contributions of the two different thermal mechanisms of bubble formation: degassing and boiling.

3.3.1.2. Degassing

We calculated the maximum possible volume of air degassed from the saline (V_{degass}) due to localized temperature increases and the resulting decrease in air solubility [71]. This was done

by integrating the solubility of air as a function of temperature expressed in the form of the Ostwald coefficient [72] over the entire volume of saline in our model. In the integration, we assumed that the solution was saturated with air at atmospheric pressure, meaning the volume of dissolved gas was the maximum possible for the initial temperature of each experiment.

3.3.1.3. Boiling

The volume of steam bubbles (V_{steam}) was calculated by multiplying the volume of steam (gas phase) in the model by the expansion factor for the transition between the liquid and gas phases of water (1600 at 1 atm pressure). This calculation overestimates the actual volume of bubbles because it does not account for the energy required for bubble expansion during the phase change. To determine the time point at which steam bubbles can first be observed in the model (Table 2, t_{sim}), a threshold of 0.1 nl was chosen. This threshold corresponds to the minimal detectable bubble volume in the video, which was 0.16 µl, divided by the expansion factor (1600).

3.3.2. Numerical model vs high-speed camera experiments

The experiments using the high-speed camera and bipolar PFA catheter demonstrated the temporal dynamics of bubble formation during delivery of the high-rate pulse sequences used in the study. By comparing the calculated/ predicted spatial and temporal temperature distributions, as well as the calculated contributions of degassing and boiling, with observations from high-speed camera recordings, we can determine how specific PFA parameters (waveform polarity, duty cycle, electrode geometry) affect bubble formation during intracardiac PFA. The results of the numerical calculations and the data from the high-speed camera experiments for all pulse protocols and experimental conditions are shown in Table 3-2.

*Table 3-2: Pulse protocols, experimental conditions, and results of high-speed camera experiments. The table shows the pulse protocols used in the experiments, the initial temperature of the saline solution (**T_0**), the average measured applied voltage (**U_{avg}**) and current (**I_{avg}**), the total energy delivered (**Energy**), the calculated maximum volume of degassed air (**V_{degass}**), the calculated volume of steam (gas phase of saline) in the model at the end of the pulse train (**V_{steam}**), the moment at which steam bubbles can first be observed in the model (**t_{sim}**), and the moment at which bubbles can first be observed in the high-speed camera recording (**t_{video}**).*

Pulse Protocol	**T_0 [°C]**	**U_{avg} [V]**	**I_{avg} [A]**	**Energy [J]**	**V_{degass} [µl]**	**V_{steam} [µl]**	**t_{sim} [ms]**	**t_{video} [ms]**
5 kHz monophasic anode on tip "100-100"	26.4	190	2.49	0.38	0.02	0.00	-	-
	26.4	380	5.09	1.54	0.07	0.07	-	-
	26.4	473	6.41	2.42	0.10	1.77	1	1
	26.4	564	7.76	3.48	0.15	7.29	0.7	0.8
	56.5	187	3.38	0.50	0.01	0.00	-	-
	54.5	279	4.95	1.10	0.02	0.72	1.2	1
	52	371	6.48	1.91	0.03	4.79	0.7	0.6
	50.5	464	7.67	2.84	0.05	16.34	0.5	0.4
	49	512	8.09	3.30	0.07	24.91	0.4	0.3
5 kHz monophasic cathode on tip "rev. 100-100"	26.4	564	7.80	3.51	0.15	7.32	0.7	0.8
	46	511	8.35	3.40	0.07	19.92	0.5	0.3
High duty factor biphasic 2-2-2-2	26.4	372	5.12	1.59	0.07	0.06	-	-
	26.4	463	6.45	2.49	0.11	1.73	1.2	-
	26.3	554	7.79	3.60	0.15	7.64	0.8	1
	26.5	645	9.12	4.83	0.20	20.11	0.6	0.6
	26.5	734	10.37	6.24	0.26	41.34	0.4	0.4
	75	268	6.44	1.40	0.00	7.29	0.6	0.7
	71	356	8.10	2.36	0.00	21.71	0.4	0.4
Low duty factor biphasic 2-2-2-500	26.4	376	5.20	1.64	0.07	0.00	-	-
	26.4	467	6.44	2.52	0.11	0.00	-	-
	26.4	560	7.78	3.64	0.15	0.00	-	-
	26.4	650	9.15	4.90	0.21	0.00	-	-
	26.4	739	10.54	6.41	0.27	0.00	-	-
	26.4	829	11.99	8.28	0.33	0.64	102.4	-
	26.4	917	13.43	10.25	0.41	12.88	74.8	103
	69	529	12.19	5.28	0.01	34.62	44.5	80
Low duty factor biphasic - longer pulses 5-5-5-500	26.4	461	6.41	2.33	0.10	0.00	-	-
	26.4	644	9.16	4.63	0.19	0.00	-	-
	26.4	822	12.00	7.78	0.30	10.84	25.8	35
	26.4	908	13.44	9.63	0.37	36.59	19	24
	63.5	533	11.28	4.71	0.03	29.41	15	19
	60	535	10.88	4.57	0.03	19.12	18	24

In *Table 3-2* we can see that the time at which bubbles attributable to boiling are first observed in the model (t_{sim}), is in good agreement with the time at which bubbles attributed to boling are first observed in the video (t_{video}) across all pulse protocols and delivered energies. This gives us confidence in our model's ability to correctly predict the onset of bubbles attributed to boiling. We also observe that the calculated volume of steam (V_{steam}) is two orders of magnitude larger than the calculated volume of degassed air (V_{degas}) across all protocols, except for the "Low duty factor biphasic protocol" and low energies, where the model does not predict large enough temperature increases to lead to boiling.

Figure 3-5, Figure 3-6 and Figure 3-7 show the predicted temperature distribution (numerical model) and bubble formation (high-speed camera recording) at different time points during the pulse train for the various pulse protocols used in the experiments (shaded in *Table 3-2*). The oscilloscope recordings of pulses are shown at the top. The duration of exposure for each movie frame is indicated by the gray-shaded area. The stills from the high-speed recording are below, with the number corresponding to the time point indicated on the oscilloscope recording. Below each still, the predicted temperature distribution from the numerical model is shown for the exact same time-points. Note that there are two additional proximal ring electrodes, which are farther from the catheter tip and were not imaged. It is also important to note that the still images (video frames) shown in the figures only partially represent the dynamics observed in the actual videos. Specifically, still images do not capture the dynamics of bubble growth and detachment.

3.3.2.1. Biphasic pulse protocols

Figure 3-5 shows the high duty factor biphasic protocol at room temperature (26.5 °C). The short duration of the pulse train (1.73 ms) and the high duty factor (0.5) lead to rapid heating of the liquid around the electrode edges, where bubbles are clearly visible. The first time point at which bubbles are visible in the high-speed camera recording is the second frame, taken between 0.4 and 0.5 ms after the first pulse. Based on the measurements of bubble diameters in frame 6 (at the end of the pulse train) we estimate the total volume of bubbles to be approximately 3.3 µl.

In the video recordings, it is hard to distinguish between bubbles produced by degassing and those produced by boiling. However, since the predicted maximum volume of degassed air given in *Table 3-2* is an order of magnitude smaller than the volume of bubbles observed in the video, we attribute most of these bubbles to boiling and the resulting steam formation. The

videos also show that these bubbles collapse very rapidly after the end of the pulse protocol, further supporting boiling as the dominant mechanism for their formation.

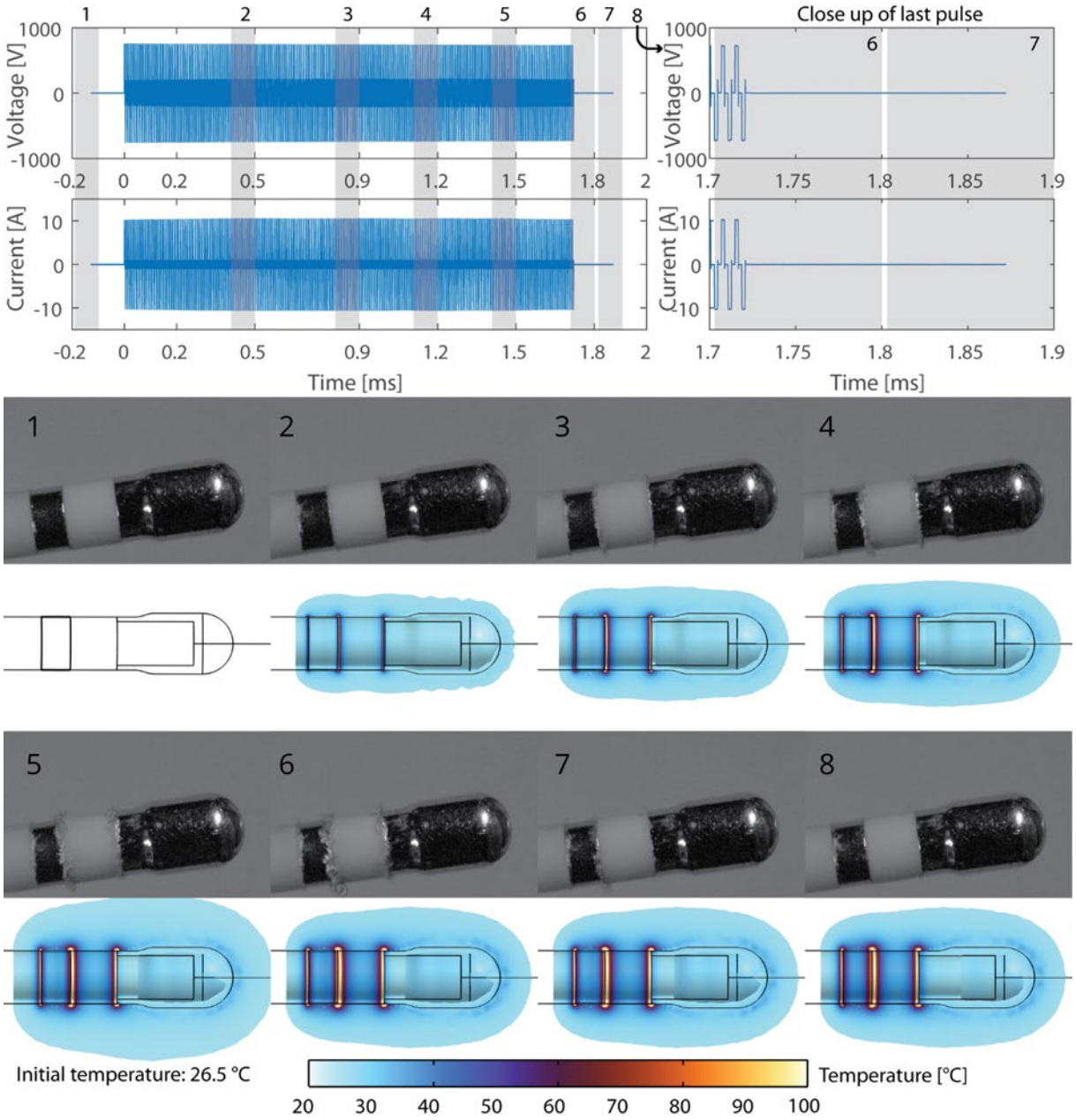

Figure 3-5: High duty factor biphasic protocol (2-2-2-500) at room temperature. The initial temperature of the experiment was 26.5 °C. The selected stills show different time points during the pulse train. The numerical simulation shows only areas with a temperature increase of at least 1 °C. Figure adapted from [46].

Figure 3-6 shows the low duty factor biphasic protocol with longer pulses at an elevated initial temperature of saline (63.5 °C). The longer pulse train duration (41.2 ms) and lower duty factor (0.02) in this protocol resulted in more gradual heating. However, due to the elevated initial

temperature, the model still shows temperatures reaching 100 °C at the electrode edges and predicts boiling. Bubbles are also visible in the high-speed camera recording. Based on measurements of bubble diameters in frame 6 (at the end of the pulse train), we estimate the total bubble volume to be about 1.5 µl. In this case, gas solubility is already very low due to the elevated initial temperature, so the volume of degassed air is negligible (0.03 µl), which means the bubbles seen in the video can be attributed to boiling.

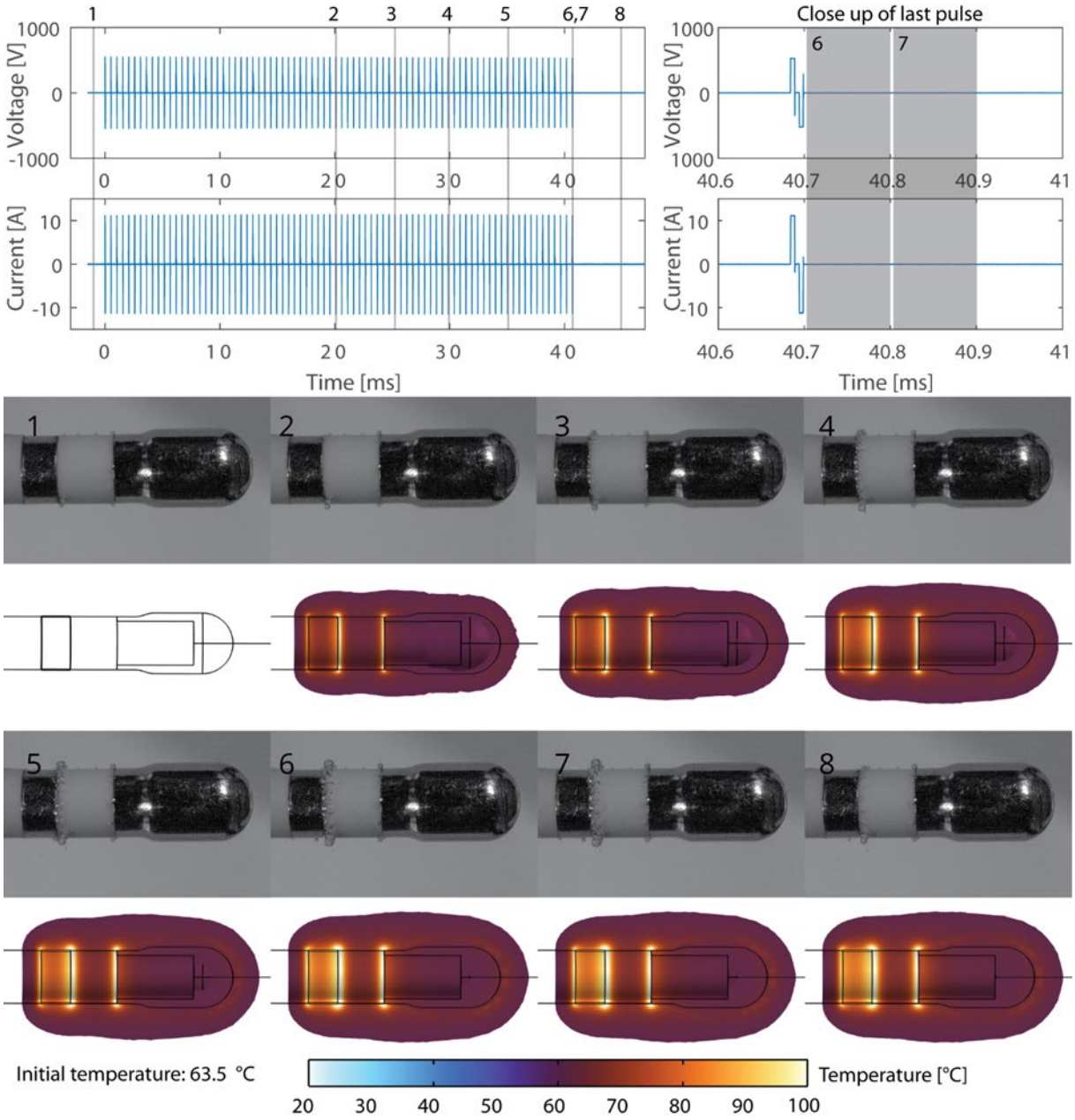

Figure 3-6: Low duty factor biphasic protocol - longer pulses (5-5-5-500) at elevated temperature. The initial temperature was 63.5 °C. The selected stills show different time points during the pulse train, as indicated on the oscilloscope recording. The numerical simulation shows only areas with a temperature increase of at least 1 °C. Figure adapted from [46].

3.3.2.2. Monophasic pulse protocols

Figure 3-7 shows the fast monophasic pulse protocol for two different electrode polarities (protocols 100–100 and reversed 100–100). Similar to the high duty factor biphasic protocol, we again see that the short duration of the pulse train (1.5 ms) and the high duty factor (0.5) lead to rapid heating of the liquid around the electrode edges, where large bubbles are clearly visible.

However, with the monophasic pulse protocol, we also observe small bubbles on the electrode surface, where the model does not predict high temperatures. These bubbles result from electrochemical reactions at the electrodes caused by the monophasic pulses: reduction at the cathode (for saline: hydrogen evolution) and oxidation at the anode (for saline: oxygen and chlorine evolution). These electrochemically generated bubbles persist on the electrode surface even after the end of the pulse train.

When we change the electrode polarities, we see differences in electrochemically produced bubbles. When the anode is the tip, we observed corona discharges near the leading edge of the ring electrode (frame 6). The corona discharges occurred during the last two pulses of the train. During this period, the model predicted boiling near the electrode edges, and significant shock-wave-induced motion can be seen (frames 6–8). With reversed polarity, when the cathode is the tip electrode, no discharges were observed, a larger volume of hydrogen gas covers the tip electrode, and the density of bubbles near the ring electrode is lower.

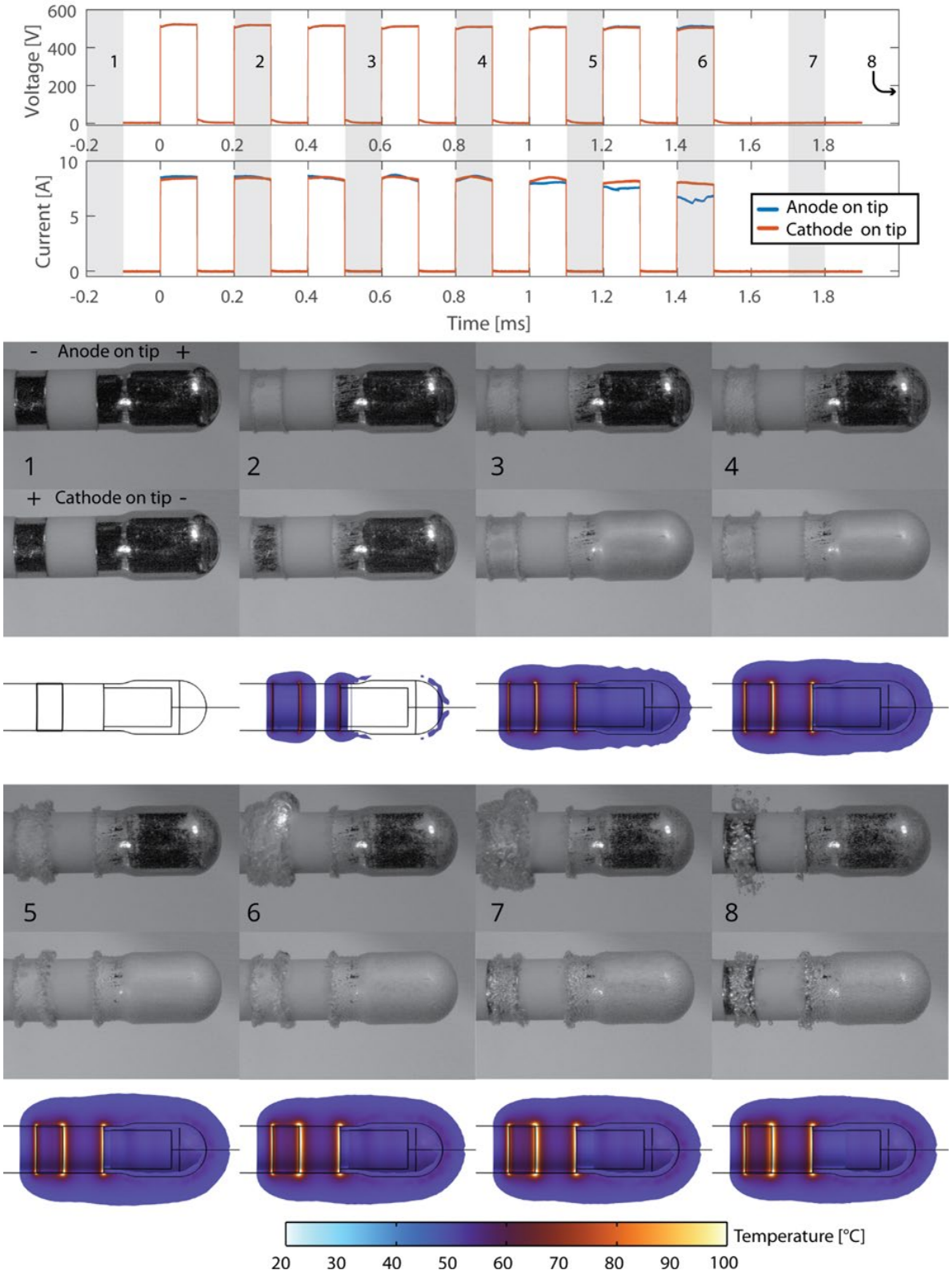

Figure 3-7: Fast monophasic pulse protocols (100-100 and reversed 100-100) at elevated initial temperatures (49 °C for the anode at the tip and 46 °C for the cathode at the tip). The images are arranged in three rows: the first row shows the anode at the tip (100-100), the second row shows the cathode at the tip (rev. 100-100), and the third row presents the numerical simulation of temperature rise during the pulse train. The numerical simulation displays only areas with a temperature increase of at least 1 °C. Figure adapted from [46].

3.4. Discussion

3.4.1. Model validation

Although the model was not directly validated by independent temperature measurements, comparison with high-speed camera recordings provides qualitative evidence of its accuracy. Bubbles attributed to boiling appeared in the experiments at the electrode edges, coinciding with regions where the model predicted the highest temperatures (Figure 3-5, Figure 3-6 and Figure 3-7). Moreover, the model-predicted onset time for boiling (t_{sim}, Table 3-2) showed good agreement with the first appearance of bubbles in the videos (t_{video}, Table 3-2). Together, these results support that the developed model of bubble formation during intracardiac pulsed field ablation can accurately predict the spatial and temporal temperature distribution and boiling onset around the electrodes of the bipolar catheter in saline, supporting its applicability for quantifying the relative contributions of boiling and degassing under different pulse protocols and electrode or catheter geometries.

3.4.2. Monophasic vs Biphasic pulse protocols

In experiments using monophasic pulse protocols, both electrochemical and thermal mechanisms of bubble formation were observed. High-speed camera videos show small bubbles on the electrode surfaces that persist even after the pulse train ends, as well as larger bubbles at the electrode edges that collapse rapidly when pulsing stops. The large, rapidly collapsing bubbles at the electrode edges closely match the numerical model's predicted boiling regions, which are characterized by temperatures approaching 100 °C. These bubbles are therefore predominantly attributed to boiling of the saline medium. In contrast, the persistent bubbles on the electrode surfaces occur in regions where the numerical model predicts lower temperatures, insufficient for boiling, indicating an electrochemical origin. Specifically, monophasic pulse durations are long enough for complete charging of the electrode's double-layer capacitance, which subsequently leads to Faradaic currents and electrolysis.

For biphasic pulse protocols and the employed geometry, boiling is the dominant mechanism of bubble formation. First, no bubbles are observed in the video before the numerical model predicts boiling, indicating that the initially observed bubbles can be attributed to boiling. Degassing would occur in the temperature range between 70 and 90 °C, which coincides with the lowest solubility of oxygen and nitrogen. Second, the predicted volume of degassed air is two orders of magnitude smaller than the predicted volume of steam bubbles. This is due to the

low volume fraction of gas solubility in water or saline—Ostwald's solubility coefficient for air in water is less than 0.02 (volume of gas divided by volume of liquid) at room temperature [71]. For bubbles to form by this mechanism, convection of liquid would be required to bring more gas to the nucleation sites, but such movement is negligible on the timescales of pulse delivery in our case, where there is no external flow.

3.4.3. Limitations

There are several limitations to our study. In terms of the numerical model, actual bubble formation and volume expansion against external pressure (pressure-volume work) were not modeled, which means the predicted volume of steam bubbles is overestimated.

When compared to a realistic scenario in the clinical use of intracardiac PFA, several differences should be noted. First, the catheter was not cooled by external fluid flow, which would reduce temperatures and thus decrease bubble formation. Second, blood is much more complex than saline, so the volumes of gas formation in saline are likely to differ from those in blood. Third, blood plasma has a high protein concentration, which can influence both the process of bubble formation and the persistence of bubbles. In addition, localized hotspots and rapid heating to temperatures near or above 100 °C could cause protein denaturation through mechanisms whose temporal dynamics are poorly understood (thresholds for protein coagulation range from 85 to 98 °C after irradiation with millisecond laser pulses [73]), with unknown effects on bubble formation.

Despite these limitations, our study and the numerical model presented provide valuable insights into the critical points of the catheter geometry where the highest temperature increases are observed (i.e., hotspots) and how different pulse protocols and delivered energies affect the temporal temperature distribution and thermal mechanisms of bubble formation. This information may also be relevant for understanding protein denaturation and potential blood clot formation, and should be considered for high voltage pulse delivery, such as in intracardiac PFA.

3.5. Conclusions

We presented a numerical model that accurately models spatial and temporal temperature distribution and predicts respective contributions of degassing and boiling to bubble formation during high voltage pulse application.

By comparing insights from numerical models with high-speed camera recordings during experiments, we found that bubbles originating from electrochemical reactions are more prevalent in monophasic pulsing protocols, whereas in high-frequency biphasic pulsing protocols, the bubbles are mainly caused by boiling of the medium. Degassing of the liquid due to lower solubility of gases at elevated temperatures does seem to play a role, though a minor one. We also observed that bubbles caused by boiling collapse very rapidly, whereas electrochemically produced bubbles or those produced through degassing appear to have longer lifetimes. Therefore, the treatment protocols best suited to minimizing gas release are biphasic trains of short (µs) pulses with a significant inter-pulse delay (i.e., low duty cycle) to prevent excessive heating. Moreover, electrodes must be designed to avoid high local current densities.

Specifically, the data from our experiments and the numerical model support the use of biphasic waveforms with individual pulse phase lengths short enough to avoid faradaic currents that would lead to electrochemical production of bubbles. In this case, the current would be confined to charging and discharging the double-layer capacitance at the electrodes continuously. The duty cycle of such biphasic protocols must strike a delicate balance between protocol efficiency (in terms of cell damage/ kill) and heat production/ dissipation, a balance that should be determined based on numerically or experimentally supported optimization. Regarding the applicator/ electrode geometry, our study shows that sharp edges should be avoided.

4. Model of *in vivo* intracardiac pulsed field ablation (PFA) in healthy and infarcted swine ventricles

This chapter addresses the second aim of the thesis. Here, we move from *in vitro* studies and models to the more complex *in vivo* studies and models of pulsed field ablation in ventricles. The study was conducted in collaboration with Sunnybrook Research Institute and Medtronic, and the results were published in a peer-reviewed journal [47]. In the scope of this study, we developed two numerical models. First, we created a schematic model of electric field and temperature distribution for PFA in healthy ventricles, which was used to study potential thermal damage during ablation and to determine, for the first time, the *in vivo* lethal electric field thresholds for cardiac tissue. The second numerical model was used to study PFA in infarcted ventricles, employing animal-specific ventricular geometry and infarcted tissue distribution. This model focused on accurately modeling electric field distribution in the infarcted left ventricle to determine the ability of PFA to ablate through infarcted scar tissue.

4.1. Background

Following the successful introduction of Pulsed Field Ablation (PFA) for isolating the pulmonary veins in the treatment of atrial fibrillation by irreversible electroporation [74], [75], [76], along with evidence of improved safety profiles and efficacy compared to radiofrequency ablation, there are now expanding efforts to use PFA for ventricular ablation [77], [78]. Achieving larger and deeper lesions by PFA in the thicker ventricular walls, as compared to atrial walls, will require further optimization and/or adjustments to PFA, such as higher dosing (using higher voltages and/or more pulses) or different vectoring of the field (i.e., different ablation and return electrode/catheter arrangements) [79], [80]. However, using higher dosing may lead to thermal damage and increase the risk of collateral injury.

The primary goal of this study was to investigate the application of Pulsed Field Ablation (PFA) in ventricular myocardium, particularly addressing the challenge of creating deeper lesions in thicker ventricular walls as opposed to atrial tissues.

This chapter focuses on the numerical models developed in this study, which were used to determine the lethal electric field threshold (LET) and thermal damage for PFA in healthy ventricles, and to predict the ability of PFA to ablate through scar tissue in infarcted ventricles.

4.2. Methods

The following is a brief overview of the general methods for *in vivo* experiments used in the study (for a complete overview of the methods refer to [47]).

We used fifteen 40–50 kg Yorkshire swine (10 healthy, 5 infarcted) in the study. PFA was performed using a two-catheter setup: a 5 mm tip focal ablation catheter (ConductrTM, Medtronic) in the left ventricle (LV) and a return catheter (MarinrTM, Medtronic) in the inferior vena cava (IVC). PFA was first performed in different segments of the LV of healthy pigs. The PFA dose was titrated by varying the pulse amplitude (1000, 1300, and 1500 V) and the number of pulse trains delivered (1-, 4-, 8-, and 16-pulse trains at 1500 V). The selected dosing was intended to create a range of PFA lesion sizes, from no durable lesion to durable transmural lesions, while preserving the nonthermal nature of PFA.

Lesion characteristics in healthy animals were assessed by cMRI at 24 hours, 7 days, and 6 weeks using native T1-weighted (T1w) and late gadolinium enhancement (LGE) cMRI, as well as by gross pathology on formalin-fixed cardiac cross sections and histopathology at 6 weeks. We also recorded iEGMs continuously for 30 seconds before and up to 5 minutes after ablation at each location and analyzed PFA-induced iEGM changes, which were then correlated with lesion size.

Finally, PFA was performed in both healthy and scarred regions of the LV in pigs 4–6 weeks post-infarct using the same two-catheter setup to explore the ability of PFA to create lesions in the presence of infarct scar. These PFA lesions were assessed only acutely, with sacrifice at 48 hours.

4.2.1. Numerical model of PFA in healthy left ventricle

The numerical model used to determine the lethal electric field threshold (LET) and thermal damage for PFA in healthy ventricles was developed in COMSOL Multiphysics (v6.1) and is described below. The model of PFA in healthy ventricles was a schematic model with an idealized geometry.

4.2.1.1. Simulation workflow

To calculate the lethal electric threshold (LET) of cardiac tissue, we first determined the electric field distribution for various ablation catheter positions in a stationary study using COMSOL. We then used MATLAB and LiveLink to extract the calculated lesion volumes for different electric field thresholds and performed the analysis (section 4.2.1.5).

To model temperature increase during PFA and potential thermal damage, the simulation workflow was as follows. First, blood flow was solved in a stationary study and the blood flow velocity distribution was then used in a subsequent time-dependent study, where temperature and electric field were solved simultaneously by coupling the heat equation (*4.8*) with the charge conservation equation (*4.4*). The time-dependent study was solved for the 16-train PFA protocol. Pauses between trains were set based on data from electrical current measurements: 2.5 s between each train and 5 s after every 4 trains. Timesteps of 0.25 s were specified, with one additional timestep before and after the application of each pulse train.

4.2.1.2. Model geometry

The numerical model geometry included the ventricles, the inferior vena cava (IVC), and surrounding bulk tissue (Figure 4-1). An idealized geometry of the ventricles was constructed using two ellipsoids truncated at the basal plane, neglecting the papillary muscles and trabeculations as described in [81]. The IVC was modelled as a cylinder. The dimensions of the schematic biventricular model and the position of the IVC were determined by scaling and aligning the biventricular model with measurements of heart size and orientation from the MRI. Geometries of the ablation and return catheters were built in Fusion 360 (Autodesk, San Francisco, CA, USA) and imported into COMSOL. The return catheter was positioned in the IVC based on the fluoroscopy images. The ablation catheter was positioned in various LV segments (Figure 4-3), perpendicular to the myocardial wall, with a 0.5-mm indentation.

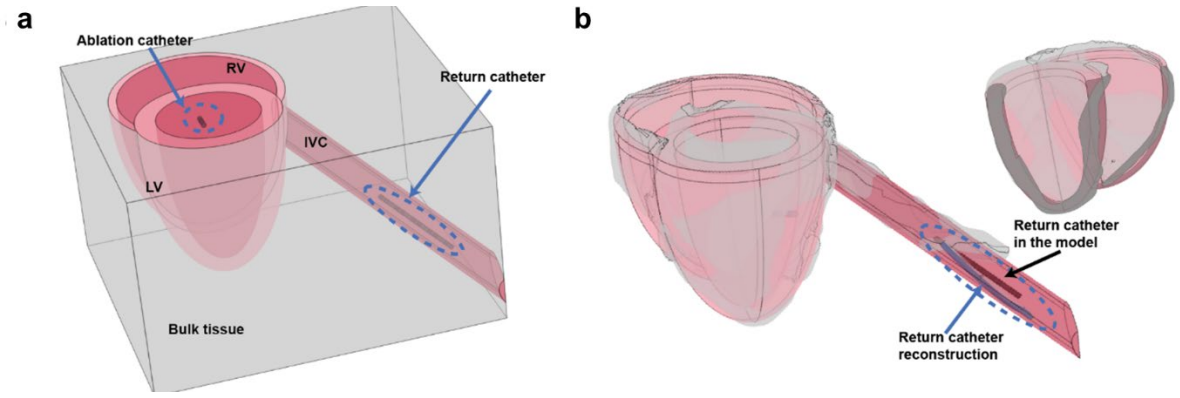

Figure 4-1: Schematic biventricular numerical model. (a) 3D geometry of the numerical model built and visualized using COMSOL Multiphysics. The model includes the left ventricle (LV), right ventricle (RV), inferior vena cava (IVC), ablation catheter, return catheter, and bulk tissue. (b) Example of alignment between the schematic biventricular model and the imported cMRI-based reconstruction of the ventricles and IVC complex (colored gray), as well as alignment of the return catheter in the model (colored black) with the fluoroscopy-based catheter reconstruction (colored blue). Figure adapted from [47].

4.2.1.3. Cardiac tissue anisotropy

The myocardium was modeled as an anisotropic material with three orthogonal directions: fiber direction, sheet direction, and normal to the sheet direction (Figure 4-2). For the sheet direction, the transmural direction was used, and for the fiber direction, a linear variation of the fiber angle across the wall was assumed with a fiber inclination of 80° at the endocardium and -40° at the epicardium.[82], [83] This reference system, which was used to describe electrical tissue properties, was created in two steps. First, the transmural direction was obtained using the Curvilinear Coordinate interface and the diffusion method, which solves the Laplace equation (*4.1*) for the specified inlet ($U = 1$ at the endocardium boundary surface) and outlet ($U = 0$ at the epicardium boundary surface) boundary conditions.

$$\Delta U = 0 \qquad 4.1$$

The gradient of the solution U forms the first basis vector and is oriented in the sheet direction. The second basis vector was defined manually in the apico-basal direction and the third basis vector was the cross product of these two. The resulting curvilinear system is then rotated by an angle Θ around the first basis vector to align the third basis vector along the fiber direction, as described in equation *4.2*.

$$\Theta = \beta \cdot \Theta_{\text{endo}} + (1 - \beta) \cdot \Theta_{epi} \qquad 4.2$$

Here $\Theta_{\text{endo}}$and Θ_{epi} represent the fiber inclination at the endocardium (80°) and epicardium (-40°) boundaries, respectively, and β is a dimensionless parameter representing the distance to the epicardium boundary. β takes values between 0 (epicardium) and 1 (endocardium) and is described in equation *4.3*:

$$\beta = \frac{D_{epi}}{D_{epi} + D_{endo}} \qquad 4.3$$

where D_{epi} and D_{endo} represent the fiber distance to the epicardium and endocardium, respectively, and were calculated using the Wall Distance interface in COMSOL.

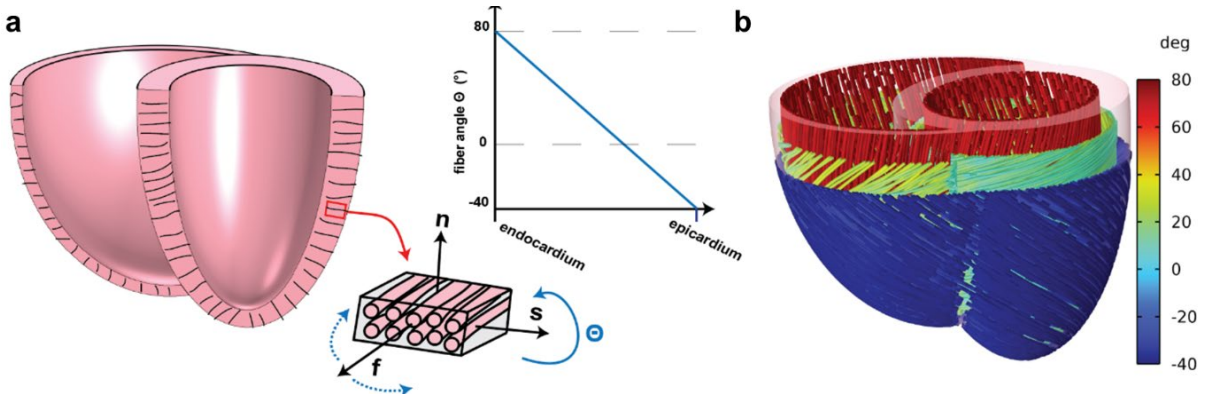

Figure 4-2: Modeling cardiac tissue anisotropy. (a) Schematic representation of myocardial structure, modeled with three orthogonal directions: fiber direction (f), sheet direction (s), and normal to the sheet direction (n). To account for the change in fiber direction from endocardium to epicardium in the model, we rotated the fiber direction (f) by an angle Θ around the sheet direction (s), which was approximated by the transmural direction. A linear variation of the fiber angle across the wall was assumed, with a fiber inclination of 80° at the endocardium and -40° at the epicardium. (b) Streamline plot of the myocardial fiber direction (f), with different colors depicting different inclinations of the fiber across the myocardial wall. Figure adapted from [47].

4.2.1.4. Electric field distribution

To model the electric field in the myocardium, the Electric Currents interface in COMSOL was used, where the continuity equation (*4.4*) for conservation of charge was solved:

$$\nabla \cdot (\sigma \nabla V) = 0 \qquad 4.4$$

where V is the electric potential and σ is the electrical conductivity. An electric potential boundary condition was applied at the electrodes of the return and ablation catheters. The voltage at the electrodes of the return catheter was set to zero, and the voltage at the ablation catheter electrode was set to the delivered voltage (1000 V, 1300V, or 1500 V). At all other boundaries, electric insulation (i.e., zero normal electric current through the boundary) was specified as a boundary condition. A 3% voltage drop at the ablation catheter electrode was included to account for voltage loss due to the catheter's internal wire resistance.

4.2.1.5. Calculating lethal electric field threshold – LET

Lethal electric field thresholds (**LET**) were calculated as follows:

1. With the help of cMRI, we assigned a myocardial segment to each *in vivo* PFA lesion based on the 13-segment model (Figure 4-3).

2. We positioned the ablation catheter in the model at the center of the determined segment (see Figure 4-3) for the specific lesions and calculated the electric field distribution.
3. We then used the bisection method to find the electric field threshold (LET_i) that results in the same calculated volume of myocardium exposed to electric field above the threshold (V_{model}) as the lesion volume determined with the LGE cMRI (detailed in [47]).

$$V_{model} = \iiint E \geq LET_i \, dV \qquad 4.5$$

Equation *4.5* shows the integration used to obtain the calculated tissue volume exposed above a certain LET_i.

4. We performed these calculations for every lesion at different time points post ablation (24 hours, 1 week, 6 weeks) and calculated the median LET for all lesions that received the same PFA dose for each imaging time point post ablation.

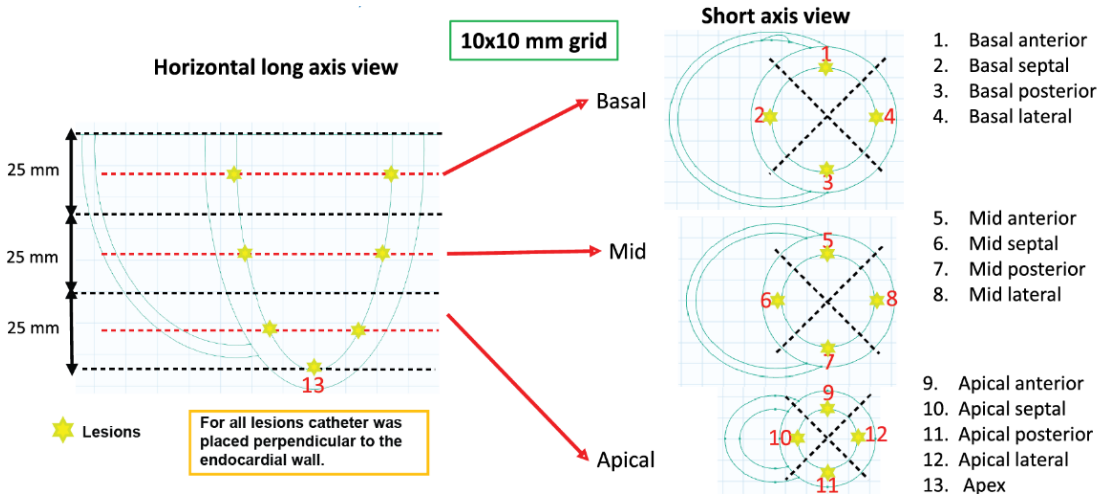

Figure 4-3: Segmentation of the left ventricle into 13 segments and the position of the ablation catheter in the numerical model. Figure adapted from [47].

4.2.1.6. Blood flow

To account for cooling of the myocardium, ablation and return electrodes through blood flow (the convection term of the heat equation (*4.8*)), a steady fluid flow in the laminar regime was modeled in the LV and IVC. To model blood flow in the laminar regime, the Laminar Flow interface in COMSOL was used, where the incompressible form of the continuity equation (*4.6*) for conservation of mass and the Navier–Stokes equation (*4.7*) for conservation of momentum

were solved in a separate stationary study. The resulting blood velocity field $\boldsymbol{u}$ was then imported into the coupled time-dependent study.

$$\nabla(\rho \boldsymbol{u}) = 0 \qquad 4.6$$

$$\rho\left(\frac{\partial \boldsymbol{u}}{\partial t} + \boldsymbol{u} \cdot \nabla \boldsymbol{u}\right) = -\nabla p + \nabla \cdot (\mu(\nabla \boldsymbol{u} + (\nabla \boldsymbol{u})^T) \qquad 4.7$$

where $\boldsymbol{u}$ is the fluid velocity, p is the fluid pressure, ρ is the fluid density, and μ is the fluid dynamic viscosity ($0.0035\,\frac{kg}{ms}$ was used for blood [84])

For blood flow in the left ventricle, an inlet boundary condition with average flow velocity and fully developed flow (i.e., parabolic laminar flow profile) was specified at the base of the ventricle and an outlet boundary condition of zero pressure was specified near the apex. At the ventricle walls and ablation catheter surface, a no-slip boundary condition was specified. Two values of the average inlet flow velocities were chosen: one for the low blood flow scenario ($u_{low} = 3\,\frac{cm}{s}$) and one for the high blood flow scenario ($u_{low} = 9\,\frac{cm}{s}$). The inlet velocities were multiplied by the ratio of the cross-sectional area at the position of the ablation catheter in the left ventricle to the surface area of the inlet, to ensure the average flow velocities around the ablation catheter and the ablated myocardium were 3 cm/s and 9 cm/s for the low and high blood flow scenarios, respectively, which is similar to velocities used in [85].

For blood flow in the IVC, an inlet boundary condition with constant flow rate and fully developed flow (i.e. parabolic laminar flow profile) was specified at the distal cross section of the IVC. The outlet boundary condition of zero pressure was specified at the proximal cross section at the IVC ostium in the RV. On the IVC inner walls and return catheter surface, a no-slip boundary condition was specified. Two values of inlet flow rates were chosen: one for the low blood flow scenario ($F_{low} = 15\,\frac{ml}{s}$) and one for the high blood flow scenario ($F_{high} = 37\,\frac{ml}{s}$), with values taken from [86]. The return catheter was positioned against the IVC wall to model the worst-case scenario.

4.2.1.7. Temperature distribution

Temperature increase during PFA depends on the interplay between ohmic heating of the tissue and blood during the application of the pulse train, and heat transfer through conduction and especially convection due to blood flow.

To model the temperature increase during PFA, the Heat Transfer in Solids and Fluids interface was used in COMSOL, where the heat equation (*4.8*) for conservation of energy was solved in a coupled time dependent study:

$$\rho c_P \left(\frac{\partial T}{\partial t} + \boldsymbol{u} \cdot \nabla T\right) - \nabla \cdot (k \nabla T) - Q = 0 \qquad 4.8$$

where ρ is the density, C_P is the heat capacity at constant pressure, k is the thermal conductivity, $\boldsymbol{u}$ is the fluid velocity field and Q is the heat source.

The heat source (Q) was described as follows:

$$Q = \text{ONOFF} \cdot \text{duty} \cdot Q_{ec} = \text{ONOFF} \cdot \text{duty} \cdot \sigma E^2 \qquad 4.9$$

Ohmic heating (Q_{ec}) is proportional to electrical conductivity (σ) and the square of the electric field distribution ($\boldsymbol{E}$) and is active only during the actual pulse duration within each pulse train. The electric field distribution ($\boldsymbol{E}$), was obtained by solving the charge conservation equation (*4.4*) in the same time-dependent study (bidirectionally coupled). When solving the charge conservation equation, a constant (rather than time-dependent) electric potential boundary condition was applied to the ablation electrode to reduce computational complexity. To relate the steady ohmic heating source to a pulsating one, the ohmic heating source was first multiplied by the duty factor of the PFA waveform ($duty$) to accurately model heating during the pulse train. To accurately model multiple pulse trains and the pauses between them, the heating source was multiplied by the $ONOFF$ variable, which was switched ON at the start of the pulse train and OFF at the end of the pulse train. This was implemented using the Events interface in COMSOL, which forces the solver to take additional time steps and reinitialize the dependent variables ($ONOFF$ and T) at the specified event times (start and end of the pulse train).

The following boundary conditions were chosen for the heat equation (4.8). At each blood flow inlet (IVC, LV), an inflow boundary condition was applied, and the upstream temperature was specified as 37 °C. A thermal insulation boundary condition (no heat flux across the boundary) was applied to the outer surface of the model. The initial temperature of the entire model was set to 37 °C.

4.2.1.8. Thermal damage

Compared to RFA, heating from PFA is not constant but occurs in short bursts during the delivery of pulse trains. For this reason, using the 50 °C isotherm, which is often used in RFA [87], to evaluate the extent of thermal damage would not provide accurate or realistic results.

To account for the pulsatile nature of heating from PFA delivery, we used the following two methods to calculate thermal damage. First, we used the "thermal dose" method, evaluating the volume of cardiac tissue where the temperature reached 55 °C or higher for at least 1 second. Second, we used the Arrhenius integral, equation *4.10*, to estimate thermal damage:

$$\Omega(t) = \int_o^t A e^{-\frac{\Delta E}{RT(t)}} dt\,, \qquad 4.10$$

where A is the frequency factor, ΔE is the activation energy, R the gas constant and T is the temperature. The volume of thermal damage was defined as the volume of cardiac tissue with a probability of cell death exceeding 63 % ($\Omega = 1$). The values of $A = 2.94 \cdot 10^{39}\ s^{-1}$ and $\Delta E = 2.596 \cdot 10^5 \frac{J}{mol}$ were taken from [88] for myocardium.

4.2.1.9. Material properties

The electrical conductivity of myocardium was modeled as anisotropic and dependent on both electric field and temperature, as described in equation *4.11*:

$$\sigma_{myo}(E,T) = \sigma_{\parallel,\perp} \cdot f_{EP}(|E|) \cdot \exp(0.015(T - 37\,°C)) \qquad 4.11$$

The temperature dependence of electrical conductivity of myocardium was described as exponential, with a rate of increase of 1.5 %.[89] Electrical conductivity along the myocardial fibers ($\sigma_{||} = 0.5\,S/m$) and the anisotropy ratio ($AR = \frac{\sigma_{\parallel}}{\sigma_{\perp}} = 1.34$), were taken from [33]. Electrical conductivity perpendicular to the myocardial fibers ($\sigma_{\perp}$) was calculated as $\sigma_{\perp} = \frac{\sigma_{\parallel}}{AR} = 0.375\,S/m$. Changes in electrical conductivity due to electroporation were modeled using a smoothed Heaviside function with two continuous derivatives [90]. Specifically, the function f_E represents a smooth increase from 1 to the electroporation conductivity increase factor ($EF = 2.65$), with the transition region centered at 550 V/cm and a width of the transition region of 500 V/cm [33].

The electrical conductivity of blood ($\sigma_{blood} = 0.7$ S/m) was taken from the IT'IS database (blood, 10 kHz). The electrical conductivity of bulk tissue ($\sigma_{bulk} = 0.38\,S/m$) was adjusted to align the calculated electrical current in the model with experimentally measured values.

The thermal properties of cardiac tissue were modeled as isotropic. The values for thermal capacity ($C_{myo} = 3686 \frac{J}{KgK}$) and density ($\rho_{myo} = 1081 \frac{kg}{m^3}$) for myocardium were taken from

the IT'IS database (heart muscle) [91]. The thermal conductivity of myocardium ($k_{myo}(T)$) was modeled as temperature dependent, as described in equation (*4.12*):

$$k_{myo}(T) = k_0(1 + 0.0012(T - 37\,°C)). \qquad 4.12$$

The initial thermal conductivity of myocardium at 37 °C ($k_0 = 0.56\frac{W}{mK}$) was taken from the IT'IS database (heart muscle) [91]. The temperature dependence of thermal conductivity of myocardium was described as linear. with a rate of increase of 0.12 % [89].

For blood, the values of thermal conductivity ($k_{blood} = 0.52\frac{W}{mK}$), thermal capacity ($C_{blood} = 3617\frac{J}{KgK}$) and density ($\rho_{blood} = 1050\frac{kg}{m^3}$) were taken from the IT'IS database (blood).[91]

For bulk tissue, the values of thermal conductivity ($k_{bulk} = 0.39\frac{W}{mK}$), thermal capacity ($C_{bulk} = 2372\frac{J}{KgK}$) and density ($\rho_{bulk} = 1027\frac{kg}{m^3}$) were taken from the IT'IS database (connective tissue).[91]

All material properties used in the numerical models and their references are listed in Supplementary Table 4-1.

Table 4-1: Material properties used in the numerical model

Material	Physical property	Value	Reference
Myocardium	$\sigma_{\parallel}$ - electrical conductivity parallel to the fibers	$0.5\,\frac{S}{m}$	[33]
	$\sigma_{\perp}$ - electrical conductivity perpendicular to the fibers	$0.375\,\frac{S}{m}$	[33]
	ρ_{myo} - density	$1081\,\frac{kg}{m^3}$	[91], heart muscle
	C_{myo} - thermal capacity	$3686\,\frac{J}{kgK}$	[91], heart muscle
	k_0 - thermal conductivity at 37°C	$0.56\,\frac{W}{mK}$	[91], heart muscle
	A - frequency factor (Arrhenius)	$2.94 \cdot 10^{39}\ s^{-1}$	[88]
	ΔE - activation energy	$2.596 \cdot 10^{5}\,\frac{J}{mol}$	[88]
Scar	σ_{scar} - electrical conductivity	$1\,\frac{S}{m}$	[92], [93]
Blood	σ_{blood} - electrical conductivity	$0.7\,\frac{S}{m}$	[91], blood 10 kHz
	ρ_{blood} - density	$1050\,\frac{kg}{m^3}$	[91], blood
	C_{blood} - thermal capacity	$3617\,\frac{J}{kgK}$	[91], blood
	k_{blood} - thermal conductivity	$0.52\,\frac{W}{mK}$	[91], blood
	μ_{blood} - dynamic viscosity	$0.0035\,\frac{kg}{ms}$	[84]
Bulk tissue	σ_{bulk} - electrical conductivity	$0.38\,\frac{S}{m}$	Original value determined from current measurements
	ρ_{bulk} - density	$1027\,\frac{kg}{m^3}$	[91], connective tissue
	C_{bulk} – thermal capacity	$2372\,\frac{J}{kgK}$	[91], connective tissue
Pt/Ir electrodes	$\rho_{Pt/Ir}$ - density	$21400\,\frac{kg}{m^3}$	COMSOL Material Library, Pt (solid)
	$C_{Pt/Ir}$ – thermal capacity	$133\,\frac{J}{kgK}$	COMSOL material library, Pt (solid)
	$k_{Pt/Ir}$ – thermal conductivity	$31\,\frac{W}{mK}$	[70]

4.2.2. Numerical model of PFA in infarcted left ventricle

The numerical model used to predict the extent of PFA lesions in infarcted ventricles, was developed in COMSOL Multiphysics (v6.1) and is described below. A detailed, animal-specific model was used for modeling PFA in infarcted ventricles.

4.2.2.1. Animal specific geometry and fibrotic tissue distribution

Pre-ablation 3D LGE cMR images were processed using ADAS 3D software (Barcelona, Spain) to obtain animal-specific ventricular geometry and fibrotic tissue distribution (scar map). In the scar map, normalized pixel intensity thresholds of 40% and 60% were used to differentiate healthy tissue (<40%), border zone (40%-60%), and dense scar (>60%).

The numerical model incorporated the animal-specific LV shell and scar map, which were used to assign different tissue properties in the LV. A simple cylinder representing the IVC was positioned relative to the LVs based on the MRI reconstructions. The ablation catheter was positioned at the lesion location identified by ablation tags from the EP navigation system (EnSite Precision), and the return catheter was positioned in the IVC based on the catheter location reconstruction for the same lesion.

4.2.2.2. Electric field distribution

To model the electric field distribution in infarcted myocardium, the continuity equation for conservation of charge was solved as described in section 4.2.1.4.

4.2.2.3. Tissue properties

The three tissue types (healthy tissue, border zone and dense scar) were included in the model by importing the scar maps from ADAS (determined from LGE cMRI as described above) into the model as the scar function. The scar function (f_{scar}) assigned a valued of 0 to healthy myocardium (<40% pixel signal intensity), a value of 1 to dense scar (>60% pixel signal intensity), and values between 0 and 1 were used to represent heterogeneous scar / border zone (40-60% pixel signal intensity). Equation (*4.13*) shows the prescribed electrical conductivity of tissue in the left ventricle based on the scar function.

$$\sigma_{tissue} = f_{scar} \cdot \sigma_{scar} + (1 - f_{scar}) \cdot \sigma_{\parallel,\perp} \cdot f_{EP}(E) \qquad 4.13$$

The electrical conductivity of healthy myocardium was modeled as anisotropic and electric field dependent. The electrical conductivity of scar tissue was considered isotropic and independent of the electric field; a value of $\sigma_{scar} = 1\ S/m$ was chosen based on the

measurements reported in [92], [93]. For the conductivity of the border zone a linear combination of electrical conductivities of scar (σ_{scar}) and healthy myocardium ($\sigma_{myo}(E)$) was used.

All material properties used in the numerical models and their literature sources are listed in Table 4-1.

4.3. Results

4.3.1. Electric field distribution and Lethal Electric Field Threshold

We determined the lethal electric field threshold (LET) for ventricular myocardium *in vivo* by using numerical modeling to calculate the electric field distribution during PFA and identifying the electric field threshold at which the calculated lesion volume matched the lesion volume measured on 3D LGE cMRI (see section 4.2.1.5). A matching LET was identified for every experimental lesion at all available time points - 24 hours, 7 days, and 6 weeks post-ablation, - taking into account the location of each individual lesion in healthy animals (Figure 4-4, panels a-c). A power function [94] was fitted to the LET as a function of the number of trains for all three evaluation time points.

Median LET varied with the number of pulse trains; at 7 days, thresholds were 725, 520, 484, and 394 V/cm for 1, 4, 8, and 16 pulse trains, respectively. Median LET was lower at 24 hours than at 7 days and 6 weeks, reflecting the larger lesion volumes observed on LGE MRI at the earlier time point.

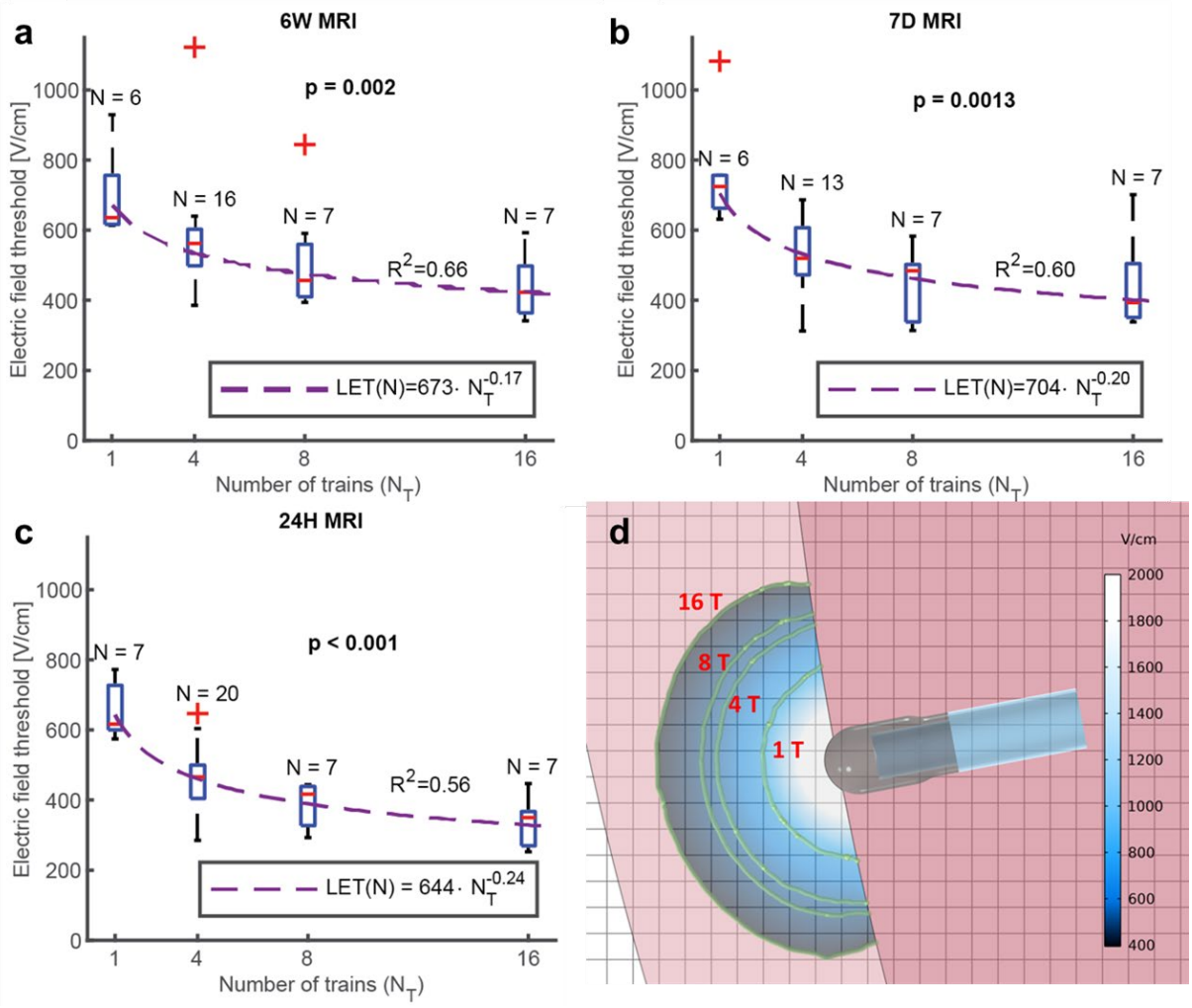

Figure 4-4: Lethal electric field threshold (LET). LET was determined by comparing the calculated electric field distribution with the volume measured by 3D LGE cMRI at different time points after ablation and with varying numbers of pulse trains: a) At 6 weeks, the median LET was 636, 562, 457, and 423 V/cm for 1, 4, 8, and 16 trains, respectively. b) At 7 days, the median LET was 725, 520, 484, and 394 V/cm for 1, 4, 8, and 16 pulse trains, respectively. c) At 24 hours, the median LET was 617, 466, 417, and 350 V/cm for 1, 4, 8, and 16 pulse trains, respectively. d) Predicted electric field distribution in cardiac tissue for a mid-posterior lesion and 1500 V, with green contours representing the median LET threshold calculated from the 7-day LGE cMRI volumes for different numbers of trains, as indicated on the individual contours. Figure adapted from [47].

When calculating the electric field distribution for each individual lesion, we accounted for the different positions of the ablation catheter inside the LV, however we did not account for the different catheter angles and contact with the endocardial wall, which can also affect the electric field distribution and the predicted lesion volume for a specific LET.

Figure 4-5 shows the effect of lesion location, catheter angle and insertion depth on the lesion volume for the 4-train 7-day LGE cMRI LET (520 V/cm). We also compare the measured lesion

volumes (7-day LGE cMRI) for 1, 4, 8 and 16 trains with the predicted range of calculated lesion volumes when accounting for the variability in catheter angles, insertion depth and location (Figure 4-5, panel d).

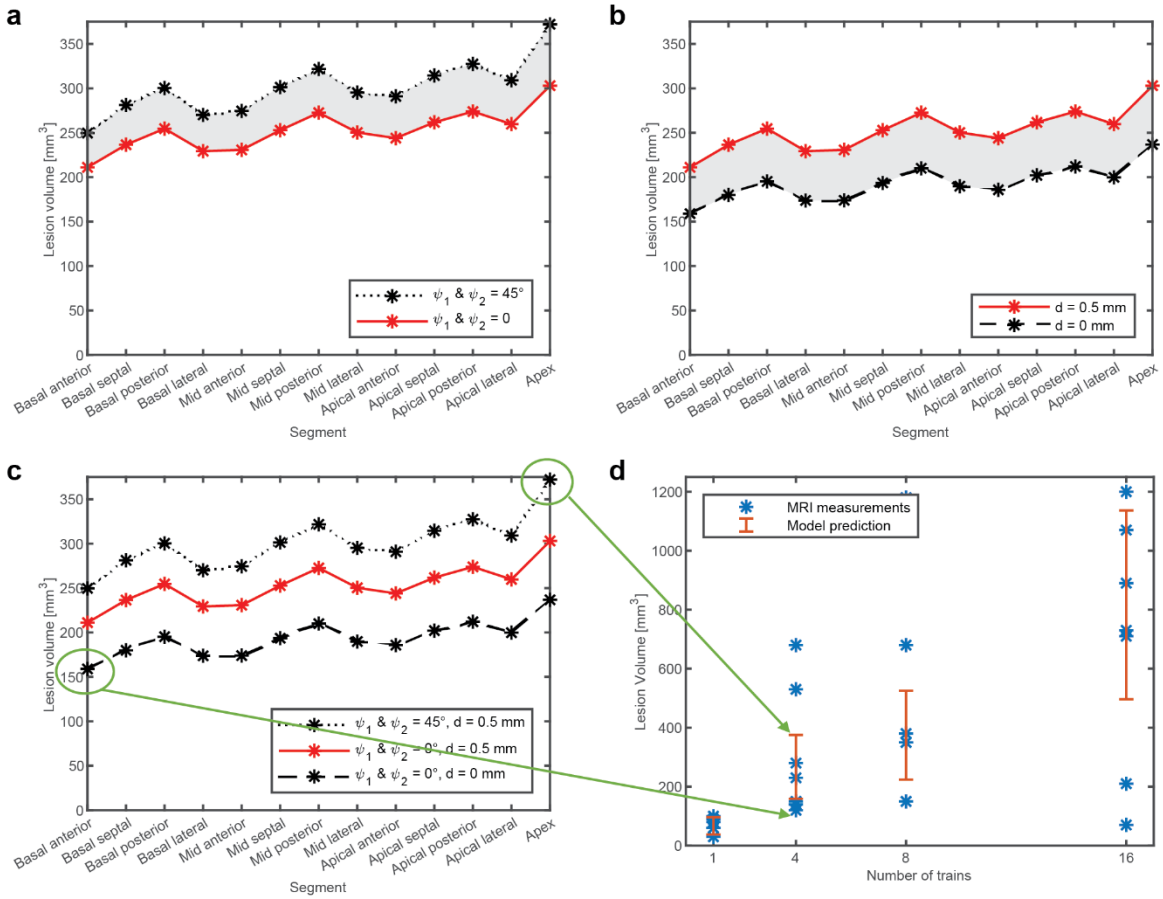

*Figure 4-5: Effect of catheter insertion depth, angle, and lesion location on computed lesion volume. (a) Effect of catheter angle on the calculated lesion volume in different LV segments for the calculated 4-train 7D LGE cMRI LET (520 V/cm). Catheter insertion depth was fixed at 0.5 mm. $\psi_1$represents the inclination of the catheter shaft in the up-down direction (base-apex) and $\psi_2$represents the rotation of the catheter around the z axis of the model, where $\psi_1 \,\&\, \psi_2 = 0°$ means the catheter is positioned perpendicular to the myocardial wall. (**b**) Effect of catheter insertion depth on the calculated lesion volume in different LV segments for the calculated 4 train 7D LGE cMRI LET (520 V/cm). The catheter was perpendicular to the myocardial wall. (**c**) Combination of catheter angle and insertion depth that results in minimum and maximum calculated lesion volume (black) for the calculated 4-train 7D LGE cMRI LET (520 V/cm), and the combination used in the model to find the LET (red). (**d**) Comparison of measured lesion volumes (7D LGE cMRI) for 1, 4, 8, and 16 trains (indicated by *) with the uncertainty of calculated lesion volumes when accounting for variability in catheter angles, insertion depth and location. Error bars represent the minimum and maximum calculated lesion volume for each 7D LGE cMRI LET (1, 4, 8, 16 trains), obtained by changing lesion location (1-13), catheter insertion depth (0-0.5mm), and angle (0- 45°). Figure adapted from [47].*

4.3.1.1. Electric field distribution in blood

We also determined the distribution of the electric field in blood (Figure 4-6), but we did not determine the LET for erythrocytes in this study. The LET for erythrocytes is expected to be higher than that for cardiomyocytes because erythrocytes are much smaller. The smaller size of erythrocytes leads to lower induced transmembrane voltages compared to larger cardiomyocytes at the same (extracellular) electric fields. Consequently, electroporation of erythrocyte membranes occurs at higher electric field strengths. The model predicts that the average volume of blood (across different lesion locations in the LV) exposed to an electric field above 1000 V/cm is 232 mm^3, with 175 mm^3 is in the LV and 57 mm^3 in the IVC. The average volume of blood exposed to an electric field above 1500 V/cm is 100 mm^3, with 89 mm^3 in the LV and 11 mm^3 in the IVC. These values represent instantaneous volumes that do not account for blood flow and should therefore be considered as the volume exposed to a single pulse train.

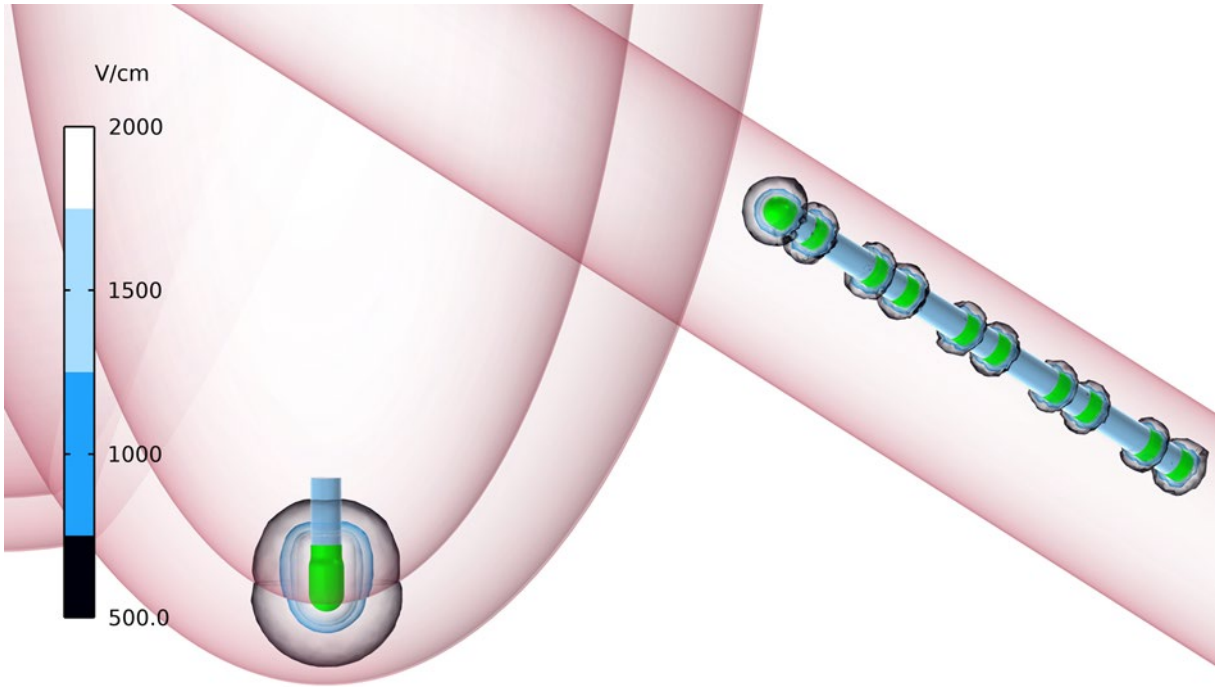

Figure 4-6: Calculated electric field distribution in tissue and blood for an apex lesion with an applied voltage of 1500 V. Electrodes are colored green.

4.3.2. Temperature increases during PFA and thermal damage

Delivery of high-voltage electric pulses (i.e., PFA) with the aim of creating a durable lesion in the myocardium by irreversible electroporation inevitably results in some Joule heating. This heating is greatest closest to the electrodes on the catheter. We used numerical modeling to

estimate heating near the ablation catheter under two blood flow conditions: one representing low blood flow and one representing high blood flow, with average flow velocities of $u_{low} = 3\frac{cm}{s}$ and $u_{high} = 9\frac{cm}{s}$ respectively.

Figure 4-7 shows the predicted temperature increase and distribution during PFA for a 16th train pulse protocol for the mid posterior lesion, for which the model predicts the highest electric current. The maximum computed temperatures at 1-, 3-, and 7-mm depth under the ablation catheter were 60, 46, and 39 °C, respectively. Numerical modeling also showed that peak temperatures on the electrode-blood surface of the ablation catheter did not exceed 66 °C in a low blood-flow condition, while the temperatures on the electrode-blood surface of the return catheter in the IVC did not exceed 41 °C in a worst-case scenario, specifically, a low blood-flow condition with the return catheter pressed against the IVC wall.

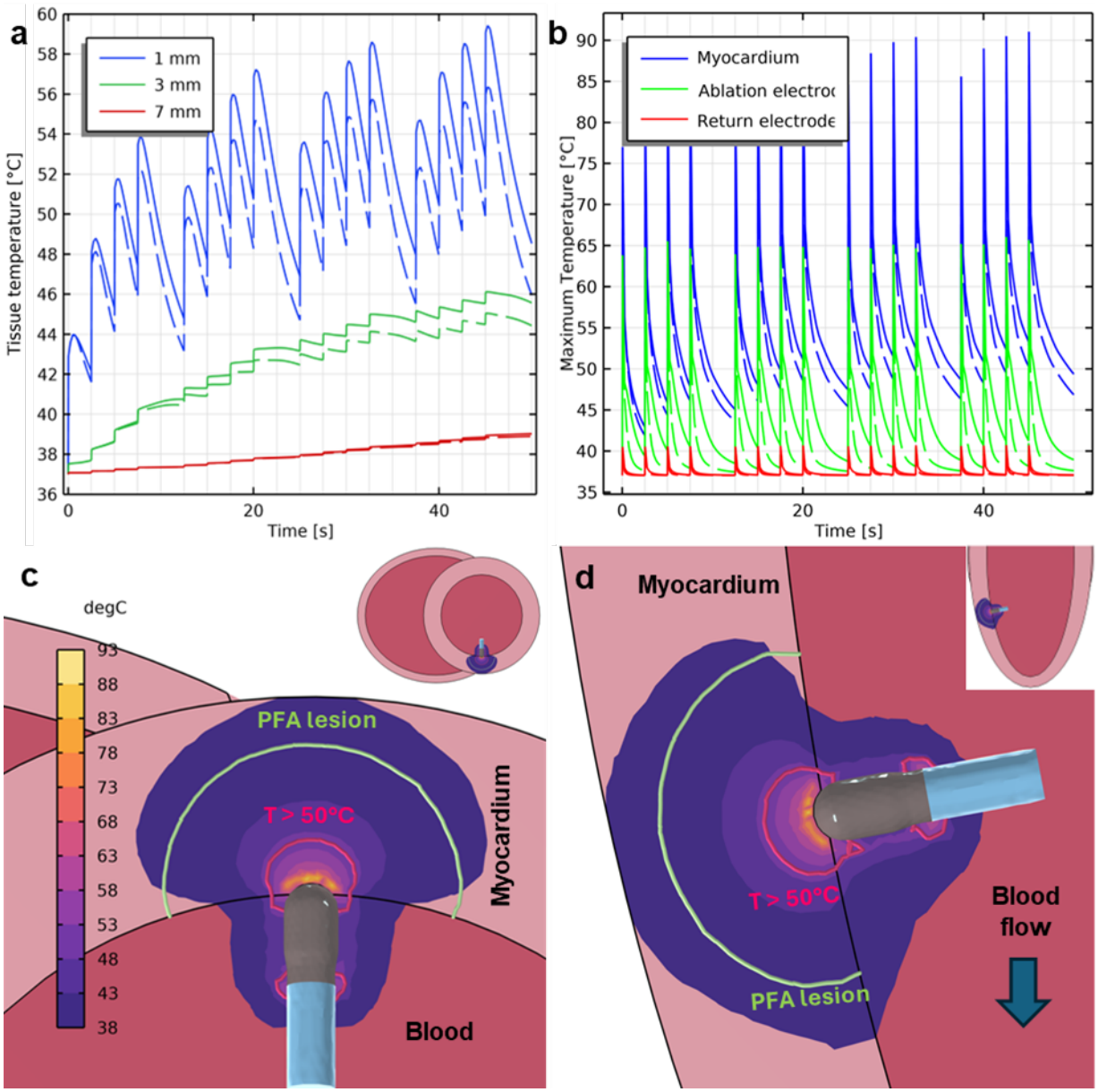

Figure 4-7: Temperature increase during PFA. a) Calculated temperature in the myocardium at depths of 1, 3, and 7 mm for the 16-pulse-train protocol. b) Calculated maximum temperatures for the 16-train protocol in the myocardium and on the ablation and return electrode surfaces. Solid lines indicate the low blood flow scenario, and dashed lines indicate the high flow scenario. Calculated temperature distribution in the myocardium and blood pool at the end of the 16th train (peak temperature) for the mid posterior lesion and low blood flow condition: c) short axis view and d) long axis view. Only temperature increases of at least 1 °C are shown. The green line indicates the possible size of the PFA lesion based on the 16-train 7-day MRI LET (median value: 394 V/cm). Figure adapted from [47].

Figure 4-8 shows predicted thermal damage during PFA for a 16th train pulse protocol for the mid posterior lesion and compares it with predicted non-thermal damage due to irreversible electroporation. The maximum predicted volume of thermal damage was 13 mm^3 (representing

less than 2% of the total lesion volume) using a threshold of 1 s at ≥ 55 °C in a low blood-flow condition. The maximal volume of tissue with a probability of cell death exceeding 63 % was 2.5 mm^3 using the Arrhenius integral in a low blood-flow condition. Panel a illustrates the extent of maximal thermal damage based on the numerical model in comparison with the total lesion size achieved by PFA, which is due to irreversible electroporation. The minute volumes of thermal damage obtained with the numerical models are consistent with the lack of a thermal signature in iron-sensitive native T1-weighted MR (for more information refer to [47]).

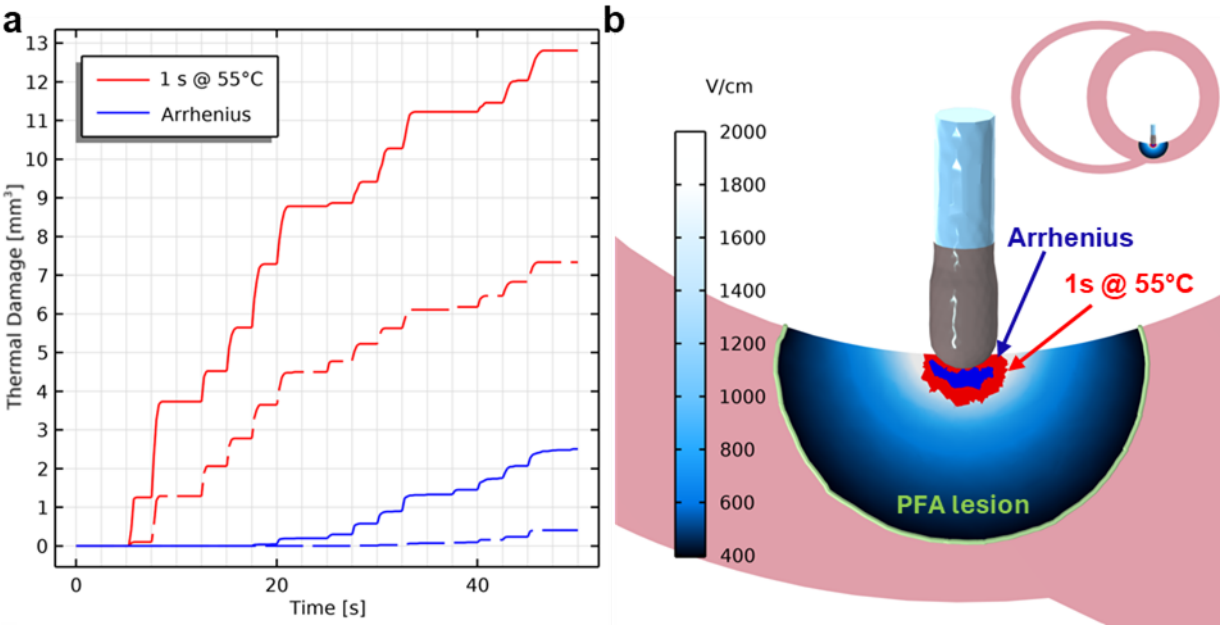

Figure 4-8: Nonthermal vs. thermal damage by Pulsed Field Ablation. a) Calculated thermal damage for the 16-train protocol using a threshold of 1 s at ≥ 55 °C and the Arrhenius integral, with a probability of cell death exceeding 63%. Solid lines represent the low blood flow scenario, and dashed lines represent the high flow scenario. b) Predicted nonthermal vs. thermal damage for the 16-train protocol. The calculated electric field distribution in the myocardium indicates the PFA lesion based on the 16-train 7-day MRI LET; only electric field values above 394 V/cm are shown. The red area indicates possible thermal damage using a threshold of 1 s at ≥ 55 °C, and the blue area indicates damage using the Arrhenius integral in the low blood-flow condition (worst case). Figure adapted from [47].

4.3.3. Ablation through fibrotic scar

In a series of chronically infarcted porcine hearts exhibiting dense fibrous remodeling (scarring) of the LV, we targeted the PFA (1500 V 8 trains) at either healthy myocardium, border zone, or dense scar using an endocardial approach.

The objective was to investigate the ability of PFA to create lesions in the presence of scar tissue using the same bipolar catheter configuration, and to compare lesion extent with predictions from modeling.

Numerical modeling of electric field distribution, incorporating tissue anisotropy, changes in electrical conductivity due to electroporation, and heterogeneous conductivity of chronically infarcted ventricles, allowed us to predict the extent of PFA lesions. The numerical model demonstrated the ability of PFA lesion to penetrate the dense scar located in the middle of the myocardium during ablation in a chronically infarcted region (Figure 4-9, panel b). The predicted extent of lesion formation toward the epicardial side beyond the intramural scar closely matched the observed extent of lesion formation on histopathology (Figure 4-9, panel c).

To predict the extent of PFA lesions, the LET determined based on MRI at 48 hours (8 trains) for healthy tissue in infarcted pigs was used (median value: 456 V/cm), which is higher than the threshold determined in healthy animals at 24 hours (median value: 417 V/cm); however, the difference was not significant ($p = 0.11$, Kruskal-Wallis test)).

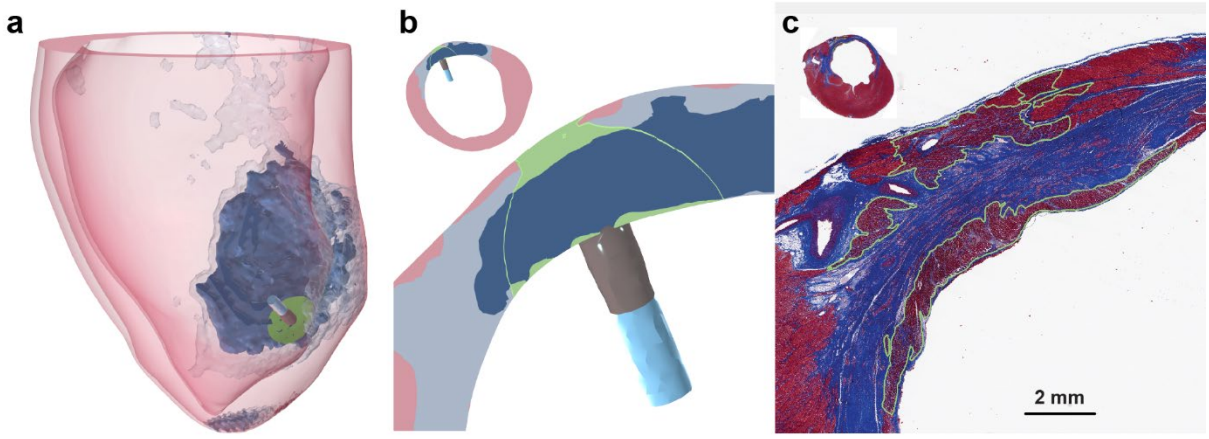

Figure 4-9: Pulsed field ablation in infarcted ventricles. a) 3D numerical model of infarcted ventricle. Healthy myocardium is shaded red; dense scar and border zone are shaded dark and light blue, respectively; and the PFA lesion is shaded green. b) Short-axis cross-section of the LV at the lesion location. The image shows the in silico electric field above the LET, outlined in green. c) The corresponding Masson's trichrome-stained histology section demonstrates the presence of an acute transmural PFA lesion despite the presence of significant regional intramural myocardial scar (red = myocardium, blue = fibrosis, purple = irreversible injury; acute lesion outlined in green). Figure adapted from [47].

4.4. Discussion

4.4.1. Lethal electric field threshold

It is often suggested that cardiac tissue is more sensitive to electroporation than other tissues; that is, it has a lower threshold for damage. However, the lethal electric field threshold (LET) for cardiac tissue *in vivo* remains undetermined. The median LET *in vivo* for four trains was 520-562 V/cm, as determined from LGE lesion volumes measured 7 days or 6 weeks after PFA. This is comparable to the recently published median LET of 535 V/cm determined for four trains in porcine hearts ex vivo (N=51 lesions in n=6 hearts), even though the time point and assay for determining cell death were different [33]. Figure 4-4 also shows that LET can be reduced by applying more pulses, but there is a diminishing return with additional pulse trains.

The concept of LET is appealing and enables prediction of lesion size even in complex tissue such as ventricular myocardium. However, LET depends on pulse parameters and waveform, as well as when and how (e.g., TTC vs. LGE cMRI) lesion size was determined [33], [95], [96], [97]. Since LET depends on the waveform and number of trains [98], it is important to determine the LET for a specific waveform or at least establish the LET difference between different waveforms. It is known that long monophasic pulses (e.g., 100-µs duration) are more efficient in achieving electroporation than short biphasic pulses (e.g., HFIRE) [33], [99]. Critically, since the lethal electric field threshold (LET) is determined by comparing the modeled electric field distribution to the lesion size, the accuracy of the LET value also depends on how well the numerical model captures the actual field distribution, which is governed by electrode geometry and arrangement, and tissue electrical properties [90], [100].

4.4.2. Electric field in blood

It is important to note that the electric field during PFA is also present in the blood pool around the catheter (Figure 4-6) and can potentially affect blood cells. It has been shown that platelets can be activated by electroporation [101], that electroporation modifies the activation of neutrophils [102], and that electroporation leads to hemolysis [103], [104].The volume of blood exposed to electric fields over 1000 or 1500 V/cm calculated in the results (section 4.3.1.1) refers to the volume exposed during a single train of pulses. In reality, blood would be exchanged between different pulse trains, with the extent of hemolysis depending on the number of pulse applications [105], [106] and the catheter design [107].

4.4.3. Thermal damage

PFA is frequently described as a nonthermal ablation modality, in which cell damage is achieved by membrane electroporation. The general belief is that the electric field is not applied for durations sufficient to produce a lethal thermal dose in tissue [108]. The nonthermal nature of PFA is thought to support an improved clinical safety profile with less potential for collateral thermal injury than clinically standard thermal modalities such as RFA. However, high PFA doses may cause bubble release of thermal origin [46]. Additionally, a small temperature rise (<8°C), was reported in an experimental setting [109]. We therefore evaluated whether the PFA delivery scheme used in our animal study produced sufficient tissue heating to cause thermal injury.

Two approaches were used: tissue temperature numerical modeling and *in vivo* imaging with a temperature-sensitive MRI technique (T1w MRI). The models estimated minimal thermal damage around the catheter tip in contact with myocardium, representing less than 2% of the total PFA lesion volume for the highest delivered dose and low blood flow. This prediction was supported in the animal experiment by the absence of thermal signature in T1w MRI [47].

4.4.4. PFA in infarcted LV

One of the most promising aspects of PFA treatment is its ability to penetrate beyond dense scar tissue associated with replacement fibrosis after myocardial infarction. An important determinant of electric field distribution in heterogeneous tissue is the electrical conductivity of the different tissue layers. For a given voltage delivered via the PFA catheter, the local electric field depends not only on the total impedance of the tissue between the (focal) ablation catheter and the return electrodes, but also on the local electrical conductivity of the tissue. Scar tissue generally has higher low-frequency conductivity than healthy myocardial tissue because scar is mature fibrosis that is hypocellular but rich in a mature collagenous matrix [92], [93], [110], [111]. Therefore, the electric field in scar tissue will generally be lower than in healthy myocardium and scars will not impede the penetration of the electric field; this is shown in Figure 4-9.

4.4.5. Limitations

The *in vivo* study of PFA in healthy and infarcted swine ventricles used the same waveform as the PulseSelect^{TM} PFA system (Medtronic, Inc.). This waveform is not optimized for thick-walled ventricular ablations or for delivery between two catheters.

LET was determined for this specific waveform and may have different values when using other waveforms or different numbers of pulse trains.

We did not control the contact force during PFA, however, previous studies have shown contact force is less impactful than mere tissue contact itself [112], [113].

We also did not control the catheter angle relative to the ventricular wall during PFA, but numerical evaluation estimated that changes in angle and tissue indentation by catheter would result in approximately ±20 % variation in total lesion volume (Figure 4-5).

LET was determined by comparing the total volume of observed lesions in cMRI with the calculated electric field distribution from numerical modeling; the exact lesion shape was not considered.

4.5. Conclusions

Using numerical modeling to calculate electric field distribution and determine lesion volume at a given LET and comparing this with lesion volume measured on LGE cMRI, enabled us to determine for the first time the lethal electric field thresholds for cardiac tissue *in vivo* and their dependence on the number of pulse trains and the time point of evaluation. The study showed that we can reduce LET, that is, increase lesion size, by applying more pulse trains, but there are diminishing returns.

Numerical modeling and temperature-sensitive MRI confirmed the nonthermal nature of PFA: for the specific pulse protocols used in the study, with less than 2% of a lesion's volume at the highest dose used being attributed to thermal damage.

The results from numerical modeling and histology suggest that ischemic scar does not impede PFA lesion depth.

5. General conclusions

The overarching aim of this dissertation was to develop and validate advanced numerical models to accurately predict electric field and temperature distributions during electroporation-based treatments involving fluid flow. The dissertation focused particularly on pulsed electric field (PEF) applications in food processing and pulsed field ablation (PFA) treatments for cardiac arrhythmias, with the goal of improving the safety and efficacy of these technologies through precise multiphysics modeling.

In the first study (Chapter 2), we advanced the numerical modeling of continuous-flow PEF treatment chambers through two key contributions: the development of a pulse-resolved model and the introduction of a particle-level exposure analysis. The pulse-resolved numerical model of continuous-flow PEF treatment chambers, validated against experimental data, improves upon conventional duty-cycle approximations by modeling each pulse individually. The model was validated against temperature measurements at the outlet of parallel plate and colinear treatment chambers for different pulse protocols and fluid flows. It provides insight into transient temperature fluctuations at various locations in the chamber caused by the delivery of pulsed field energy, which are smoothed out by the duty cycle approach. The magnitude of these fluctuations depends on the PEF treatment parameters, chamber geometry, and fluid flow. If transient temperature fluctuations inside the treatment volume are small, the duty cycle approach may be sufficient; however, if the transient temperature fluctuations are large, the duty cycle approach could fail to predict potential thermal damage to the product and the risk of equipment deterioration. Thus, the pulse-resolved modeling approach offers potential advantages for more in-depth optimization of chamber design, pulse protocols, and for ensuring overall process quality and safety. This study also introduced the particle-level exposure analysis, an extension applicable to both the pulse-resolved and duty-cycle models. By evaluating the exposure of each particle or cell to electric field and temperature along its trajectory in the treatment chamber, this analysis allows us to derive key exposure metrics – such as the maximum temperature reached by each particle and the cumulative time spent above an electric-field threshold - and their statistical distribution across the entire product. These distributions provide direct insight into treatment homogeneity and could be essential for assessing actual PEF treatment outcomes, by revealing the fraction of the product that may be undertreated or at risk of thermal damage. The framework can therefore serve as a valuable tool

for comparing the effects of different chamber geometries, flow rates, and pulse protocols on treatment homogeneity, and for building stronger connections between simulation and experimental results.

In the second study (Chapter 3), we investigated bubble formation during intracardiac PFA using a numerical model of a bipolar PFA catheter in saline solution and high-speed camera recordings during experiments. The numerical model focused on accurately simulating heating of the solution around the sharp electrode edges and examined the thermal mechanisms of bubble formation, specifically degassing and boiling, by incorporating the phase change of water from liquid to gas. By comparing insights from the numerical model with high-speed camera recordings of the experiments, we found that bubbles originating from electrochemical reactions are more prevalent in monophasic pulsing protocols, whereas in high-frequency biphasic pulsing protocols, bubbles are mainly caused by boiling of the medium. Degassing of the liquid due to lower gas solubility at elevated temperatures appears to play a role, though a minor one. Therefore, the treatment protocols best suited to minimizing gas release are biphasic trains of short (µs) pulses with a significant inter-pulse delay (i.e., low duty cycle) to prevent excessive localized heating. The findings also highlighted the critical influence of electrode geometry, recommending the avoidance of sharp edges to mitigate localized heating and arcing.

In the scope of third study (Chapter 4), we developed comprehensive numerical models of *in vivo* endocardial PFA in both healthy and chronically infarcted porcine ventricles. These models provided electric field and temperature distributions during PFA for different ablation catheter positions, taking into account cardiac tissue anisotropy, intracardiac blood flow, and fibrotic tissue distribution (scarmap). By comparing predicted lesion volumes for specific electric field thresholds with lesion volumes measured by LGE cMRI, we determined for the first time the *in vivo* lethal electric field threshold for ventricular myocardium and its dependence on the number of pulse trains and the time point of evaluation. Numerical modeling and temperature-sensitive MRI confirmed the nonthermal nature of PFA: for the specific pulse protocols used in the study, less than 2% of a lesion's volume at the highest dose was attributed to thermal damage. Importantly, the models demonstrated that PFA can effectively penetrate dense myocardial scars, which was confirmed through histology, providing essential insights for clinical applications targeting arrhythmogenic substrates in scarred ventricles.

In summary, this dissertation has significantly advanced the understanding and predictability of electric field and temperature dynamics in electroporation-based treatments through rigorous numerical modeling and experimental validation. The developed models provide a valuable computational framework to improve the safety and effectiveness of PEF and PFA technologies, offering a strong foundation for future research and optimization in both food processing and cardiac ablation.

6. Original contributions to science

Advanced numerical models of continuous flow pulsed electric field (PEF) treatment chambers

Accurate modeling of electric field and temperature distributions is an important tool for optimizing pulsed electric field (PEF) processes. In this contribution, a validated pulse-resolved numerical model of continuous-flow PEF treatment chambers was developed, improving upon conventional duty-cycle approximations by explicitly modeling each electrical pulse. This novel approach provides detailed insights into transient temperature fluctuations, enabling more precise predictions of temperature dynamics inside the treatment chamber.

Additionally, a particle-level exposure analysis was introduced, evaluating the total exposure of each particle or cell to electric field and temperature along its trajectory to derive key exposure metrics and their statistical distribution across the entire product. This analysis provides a direct measure of treatment homogeneity and a potential link to PEF treatment outcomes such as process efficacy and quality, offering a more comprehensive and effective framework for PEF process optimization.

Numerical model of bubble formation during intracardiac pulsed field ablation (PFA)

We performed an *in vitro* study on the mechanism of bubble formation during intracardiac pulsed field ablation (PFA), which can affect treatment safety. In the scope of this study, a numerical model of a bipolar PFA catheter in saline solution was developed and validated against high-speed camera recordings from the experiments. This model accurately captured heating around sharp electrode edges and the thermal mechanisms of bubble formation, including degassing and boiling. The study revealed that electrochemical bubble formation is predominant in monophasic protocols, while boiling dominates in high-frequency biphasic protocols. The findings indicated that optimal protocols for minimizing gas release are biphasic pulses with low duty cycles, and also emphasized the importance of avoiding sharp electrode edges to reduce localized heating and arcing.

Numerical models of *in vivo* intracardiac pulsed field ablation (PFA) in healthy and infarcted swine ventricles

We developed detailed numerical models of *in vivo* pulsed field ablation (PFA) in healthy and infarcted ventricles, accounting for ventricular geometry, cardiac tissue anisotropy, blood flow,

and scar tissue distribution. The model enabled us to determine *in vivo* lethal electric field thresholds for ventricular myocardium. It also allowed us to assess temperature distribution during PFA and potential thermal damage in tissue. Importantly, the developed models also enabled us to investigate the capacity of PFA to create lesions in the presence of scar tissue, providing important clinical insights for arrhythmia treatment in scarred ventricles. These models can be used to determine lesion shape and size, as well as potential thermal damage, for any novel catheter design.

.

7. References

[1] T. Kotnik, L. Rems, M. Tarek, and D. Miklavčič, "Membrane Electroporation and Electropermeabilization: Mechanisms and Models," *Annu. Rev. Biophys.*, vol. 48, no. 1, pp. 63–91, May 2019, doi: 10.1146/annurev-biophys-052118-115451.

[2] T. Kotnik, P. Kramar, G. Pucihar, D. Miklavcic, and M. Tarek, "Cell membrane electroporation- Part 1: The phenomenon," *IEEE Electr. Insul. Mag.*, vol. 28, no. 5, pp. 14–23, Sept. 2012, doi: 10.1109/MEI.2012.6268438.

[3] L. Rems and D. Miklavčič, "Tutorial: Electroporation of cells in complex materials and tissue," *J. Appl. Phys.*, vol. 119, no. 20, p. 201101, May 2016, doi: 10.1063/1.4949264.

[4] M. L. Yarmush, A. Golberg, G. Serša, T. Kotnik, and D. Miklavčič, "Electroporation-Based Technologies for Medicine: Principles, Applications, and Challenges," *Annu. Rev. Biomed. Eng.*, vol. 16, no. 1, pp. 295–320, July 2014, doi: 10.1146/annurev-bioeng-071813-104622.

[5] B. Geboers *et al.*, "High-Voltage Electrical Pulses in Oncology: Irreversible Electroporation, Electrochemotherapy, Gene Electrotransfer, Electrofusion, and Electroimmunotherapy," *Radiology*, vol. 295, no. 2, pp. 254–272, May 2020, doi: 10.1148/radiol.2020192190.

[6] T. Kotnik, W. Frey, M. Sack, S. Haberl Meglič, M. Peterka, and D. Miklavčič, "Electroporation-based applications in biotechnology," *Trends Biotechnol.*, vol. 33, no. 8, pp. 480–488, Aug. 2015, doi: 10.1016/j.tibtech.2015.06.002.

[7] A. Golberg *et al.*, "Energy-efficient biomass processing with pulsed electric fields for bioeconomy and sustainable development," *Biotechnol. Biofuels*, vol. 9, no. 1, p. 94, Dec. 2016, doi: 10.1186/s13068-016-0508-z.

[8] G. A. Ballash *et al.*, "Pulsed electric field application reduces carbapenem- and colistin-resistant microbiota and blaKPC spread in urban wastewater," *J. Environ. Manage.*, vol. 265, p. 110529, July 2020, doi: 10.1016/j.jenvman.2020.110529.

[9] S. Toepfl, C. Siemer, G. Saldaña-Navarro, and V. Heinz, "Overview of Pulsed Electric Fields Processing for Food," in *Emerging Technologies for Food Processing*, Elsevier, 2014, pp. 93–114. doi: 10.1016/B978-0-12-411479-1.00006-1.

[10] S. Mahnič-Kalamiza, E. Vorobiev, and D. Miklavčič, "Electroporation in Food Processing and Biorefinery," *J. Membr. Biol.*, vol. 247, no. 12, pp. 1279–1304, Dec. 2014, doi: 10.1007/s00232-014-9737-x.

[11] "Juice preservation by pulsed electric fields," *Stewart Postharvest Rev.*, vol. 8, no. 2, pp. 1–4, 2012, doi: 10.2212/spr.2012.2.3.

[12] D. Bermúdez-Aguirre, C. P. Dunne, and G. V. Barbosa-Cánovas, "Effect of processing parameters on inactivation of Bacillus cereus spores in milk using pulsed electric fields," *Int. Dairy J.*, vol. 24, no. 1, pp. 13–21, May 2012, doi: 10.1016/j.idairyj.2011.11.003.

[13] C. Delso, A. Berzosa, J. Sanz, I. Álvarez, and J. Raso, "Microbial Decontamination by Pulsed Electric Fields (PEF) in Winemaking," in *Grapes and Wine [Working Title]*, IntechOpen, 2021. doi: 10.5772/intechopen.101112.

[14] P. Mañas and R. Pagán, "Microbial inactivation by new technologies of food preservation," *J. Appl. Microbiol.*, vol. 98, no. 6, pp. 1387–1399, June 2005, doi: 10.1111/j.1365-2672.2005.02561.x.

[15] S. Toepfl, A. Mathys, V. Heinz, and D. Knorr, "Review: Potential of High Hydrostatic Pressure and Pulsed Electric Fields for Energy Efficient and Environmentally Friendly

Food Processing," *Food Rev. Int.*, vol. 22, no. 4, pp. 405–423, Dec. 2006, doi: 10.1080/87559120600865164.
[16] M. Morales-de la Peña, P. Elez-Martínez, and O. Martín-Belloso, "Food Preservation by Pulsed Electric Fields: An Engineering Perspective," *Food Eng. Rev.*, vol. 3, no. 2, pp. 94–107, June 2011, doi: 10.1007/s12393-011-9035-7.
[17] D. Gerlach, N. Alleborn, A. Baars, A. Delgado, J. Moritz, and D. Knorr, "Numerical simulations of pulsed electric fields for food preservation: A review," *Innov. Food Sci. Emerg. Technol.*, vol. 9, no. 4, pp. 408–417, Oct. 2008, doi: 10.1016/j.ifset.2008.02.001.
[18] B. Qin, Q. Zhang, G. V. Barbosa-Cánovas, B. G. Swanson, and P. D. Pedrow, "Pulsed Electric Field Treatment Chamber Design for Liquid Food Pasteurization Using a Finite Element Method," *Trans. ASAE*, vol. 38, no. 2, pp. 557–565, 1995, doi: 10.13031/2013.27866.
[19] N. Meneses, H. Jaeger, J. Moritz, and D. Knorr, "Impact of insulator shape, flow rate and electrical parameters on inactivation of E. coli using a continuous co-linear PEF system," *Innov. Food Sci. Emerg. Technol.*, vol. 12, no. 1, pp. 6–12, Jan. 2011, doi: 10.1016/j.ifset.2010.11.007.
[20] M. Lindgren, K. Aronsson, S. Galt, and T. Ohlsson, "Simulation of the temperature increase in pulsed electric field (PEF) continuous flow treatment chambers," *Innov. Food Sci. Emerg. Technol.*, vol. 3, no. 3, pp. 233–245, Sept. 2002, doi: 10.1016/S1466-8564(02)00044-9.
[21] K. Huang, L. Yu, L. Gai, and J. Wang, "Coupled Simulations in Colinear and Coaxial Continuous Pulsed Electric Field Treatment Chambers," *Trans. ASABE*, pp. 1473–1484, Sept. 2013, doi: 10.13031/trans.56.9167.
[22] A. Fiala, P. C. Wouters, E. van den Bosch, and Y. L. M. Creyghton, "Coupled electrical-fluid model of pulsed electric field treatment in a model food system," *Innov. Food Sci. Emerg. Technol.*, vol. 2, no. 4, pp. 229–238, Dec. 2001, doi: 10.1016/S1466-8564(01)00042-X.
[23] H. Jaeger, N. Meneses, and D. Knorr, "Impact of PEF treatment inhomogeneity such as electric field distribution, flow characteristics and temperature effects on the inactivation of E. coli and milk alkaline phosphatase," *Innov. Food Sci. Emerg. Technol.*, vol. 10, no. 4, pp. 470–480, Oct. 2009, doi: 10.1016/j.ifset.2009.03.001.
[24] R. Buckow, S. Schroeder, P. Berres, P. Baumann, and K. Knoerzer, "Simulation and evaluation of pilot-scale pulsed electric field (PEF) processing," *J. Food Eng.*, vol. 101, no. 1, pp. 67–77, Nov. 2010, doi: 10.1016/j.jfoodeng.2010.06.010.
[25] K. Knoerzer, P. Baumann, and R. Buckow, "An iterative modelling approach for improving the performance of a pulsed electric field (PEF) treatment chamber," *Comput. Chem. Eng.*, vol. 37, pp. 48–63, Feb. 2012, doi: 10.1016/j.compchemeng.2011.09.002.
[26] P. A. Garcia, R. E. N. Ii, and R. V. Davalos, "NON-THERMAL IRREVERSIBLE ELECTROPORATION FOR TISSUE ABLATION," p. 22.
[27] B. Howard *et al.*, "Reduction in Pulmonary Vein Stenosis and Collateral Damage With Pulsed Field Ablation Compared With Radiofrequency Ablation in a Canine Model," *Circ. Arrhythm. Electrophysiol.*, vol. 13, no. 9, p. e008337, Sept. 2020, doi: 10.1161/CIRCEP.120.008337.
[28] A. Sugrue *et al.*, "Irreversible electroporation for catheter-based cardiac ablation: a systematic review of the preclinical experience," *J. Interv. Card. Electrophysiol.*, vol. 55, no. 3, pp. 251–265, Sept. 2019, doi: 10.1007/s10840-019-00574-3.

[29] A. Verma, S. J. Asivatham, T. Deneke, Q. Castellvi, and R. E. Neal, “Primer on Pulsed Electrical Field Ablation: Understanding the Benefits and Limitations,” *Circ. Arrhythm. Electrophysiol.*, vol. 14, no. 9, Sept. 2021, doi: 10.1161/CIRCEP.121.010086.
[30] A. Belalcazar, “Safety and efficacy aspects of pulsed field ablation catheters as a function of electrode proximity to blood and energy delivery method,” *Heart Rhythm O2*, vol. 2, no. 6, pp. 560–569, Dec. 2021, doi: 10.1016/j.hroo.2021.10.004.
[31] D. Meckes, M. Emami, I. Fong, D. H. Lau, and P. Sanders, “PULSED-FIELD ABLATION: COMPUTATIONAL MODELLING OF ELECTRIC FIELDS FOR LESION DEPTH ANALYSIS,” *Heart Rhythm O2*, p. S2666501822001143, May 2022, doi: 10.1016/j.hroo.2022.05.009.
[32] B. Howard *et al.*, “Effects of Electrode-Tissue Proximity on Cardiac Lesion Formation Using Pulsed Field Ablation,” *Circ. Arrhythm. Electrophysiol.*, vol. 15, no. 10, Oct. 2022, doi: 10.1161/CIRCEP.122.011110.
[33] B. Kos *et al.*, “Determination of lethal electric field threshold for pulsed field ablation in ex vivo perfused porcine and human hearts,” *Front. Cardiovasc. Med.*, vol. 10, p. 1160231, June 2023, doi: 10.3389/fcvm.2023.1160231.
[34] A. Petras *et al.*, “Is a single lethal electric field threshold sufficient to characterize the lesion size in computational modeling of cardiac pulsed field ablation?,” *Heart Rhythm O2*, p. S2666501825000790, Feb. 2025, doi: 10.1016/j.hroo.2025.02.014.
[35] M. Gómez-Barea, T. García-Sánchez, and A. Ivorra, “A computational comparison of radiofrequency and pulsed field ablation in terms of lesion morphology in the cardiac chamber,” *Sci. Rep.*, vol. 12, no. 1, p. 16144, Sept. 2022, doi: 10.1038/s41598-022-20212-9.
[36] L. Zang, K. Gu, X. Ji, H. Zhang, S. Yan, and X. Wu, “Comparative Analysis of Temperature Rise between Convective Heat Transfer Method and Computational Fluid Dynamics Method in an Anatomy-Based Left Atrium Model during Pulsed Field Ablation: A Computational Study,” *J. Cardiovasc. Dev. Dis.*, vol. 10, no. 2, p. 56, Jan. 2023, doi: 10.3390/jcdd10020056.
[37] I. Lackovic, R. Magjarevic, and D. Miklavcic, “Three-dimensional finite-element analysis of joule heating in electrochemotherapy and in vivo gene electrotransfer,” *IEEE Trans. Dielectr. Electr. Insul.*, vol. 16, no. 5, pp. 1338–1347, Oct. 2009, doi: 10.1109/TDEI.2009.5293947.
[38] P. Agnass *et al.*, “Mathematical modeling of the thermal effects of irreversible electroporation for *in vitro* , *in vivo* , and clinical use: a systematic review,” *Int. J. Hyperthermia*, vol. 37, no. 1, pp. 486–505, Jan. 2020, doi: 10.1080/02656736.2020.1753828.
[39] R. V. Davalos, S. Bhonsle, and R. E. Neal, “Implications and considerations of thermal effects when applying irreversible electroporation tissue ablation therapy,” *The Prostate*, vol. 75, no. 10, pp. 1114–1118, July 2015, doi: 10.1002/pros.22986.
[40] G. Wardhana, J. P. Almeida, M. Abayazid, and J. J. Fütterer, “Development of a thermal model for irreversible electroporation: an approach to estimate and optimize the IRE protocols,” *Int. J. Comput. Assist. Radiol. Surg.*, vol. 16, no. 8, pp. 1325–1334, Aug. 2021, doi: 10.1007/s11548-021-02403-3.
[41] A. González-Suárez, E. Berjano, J. M. Guerra, and L. Gerardo-Giorda, “Computational Modeling of Open-Irrigated Electrodes for Radiofrequency Cardiac Ablation Including Blood Motion-Saline Flow Interaction,” *PLOS ONE*, vol. 11, no. 3, p. e0150356, Mar. 2016, doi: 10.1371/journal.pone.0150356.

[42] A. González-Suárez and E. Berjano, “Comparative Analysis of Different Methods of Modeling the Thermal Effect of Circulating Blood Flow During RF Cardiac Ablation,” *IEEE Trans. Biomed. Eng.*, p. 10, 2015.
[43] A. González-Suárez, J. J. Pérez, R. M. Irastorza, A. D’Avila, and E. Berjano, “Computer modeling of radiofrequency cardiac ablation: 30 years of bioengineering research,” *Comput. Methods Programs Biomed.*, p. 106546, Nov. 2021, doi: 10.1016/j.cmpb.2021.106546.
[44] S. Coderch-Navarro, E. Berjano, O. Camara, and A. González-Suárez, “High-power short-duration vs. standard radiofrequency cardiac ablation: comparative study based on an in-silico model,” *Int. J. Hyperthermia*, vol. 38, no. 1, pp. 582–592, Jan. 2021, doi: 10.1080/02656736.2021.1909148.
[45] P. Lombergar, K. Flisar, D. Miklavčič, and S. Mahnič-Kalamiza, “Time-dependent model of temperature distribution in continuous flow pulsed electric field treatment chambers,” *Innov. Food Sci. Emerg. Technol.*, vol. 93, p. 103628, May 2024, doi: 10.1016/j.ifset.2024.103628.
[46] S. Mahnič-Kalamiza *et al.*, “Elucidating the mechanisms of microbubble formation in intracardiac pulsed field ablation,” *Electrochimica Acta*, vol. 497, p. 144550, Sept. 2024, doi: 10.1016/j.electacta.2024.144550.
[47] D. Miklavčič *et al.*, “Biophysics and electrophysiology of pulsed field ablation in normal and infarcted porcine cardiac ventricular tissue,” *Sci. Rep.*, vol. 14, no. 1, p. 32063, Dec. 2024, doi: 10.1038/s41598-024-83683-y.
[48] D. Miklavčič, “Network for Development of Electroporation-Based Technologies and Treatments: COST TD1104,” *J. Membr. Biol.*, vol. 245, no. 10, pp. 591–598, Oct. 2012, doi: 10.1007/s00232-012-9493-8.
[49] T. Reichlin *et al.*, “Pulsed Field or Cryoballoon Ablation for Paroxysmal Atrial Fibrillation,” *N. Engl. J. Med.*, vol. 392, no. 15, pp. 1497–1507, Apr. 2025, doi: 10.1056/NEJMoa2502280.
[50] R. B. McCleskey, “Electrical Conductivity of Electrolytes Found In Natural Waters from (5 to 90) °C,” *J. Chem. Eng. Data*, vol. 56, no. 2, pp. 317–327, Feb. 2011, doi: 10.1021/je101012n.
[51] B. Prasad Lamsal and V. Kumar Jindal, “Variation in Electrical Conductivity of Selected Fruit Juices During Continuous Ohmic Heating,” *KMUTNB Int. J. Appl. Sci. Technol.*, vol. 7, no. 1, pp. 47–56, Mar. 2014, doi: 10.14416/j.ijast.2014.01.008.
[52] T. Eleršek *et al.*, “Electroporation as a Solvent-Free Green Technique for Non-Destructive Extraction of Proteins and Lipids From Chlorella vulgaris,” *Front. Bioeng. Biotechnol.*, vol. 8, p. 443, May 2020, doi: 10.3389/fbioe.2020.00443.
[53] G. Pataro, G. Ferrentino, C. Ricciardi, and G. Ferrari, “Pulsed electric fields assisted microbial inactivation of S. cerevisiae cells by high pressure carbon dioxide,” *J. Supercrit. Fluids*, vol. 54, no. 1, pp. 120–128, July 2010, doi: 10.1016/j.supflu.2010.04.003.
[54] K. Flisar, S. H. Meglic, J. Morelj, J. Golob, and D. Miklavcic, “Testing a prototype pulse generator for a continuous flow system and its use for E. coli inactivation and microalgae lipid extraction,” *Bioelectrochemistry*, vol. 100, pp. 44–51, Dec. 2014, doi: 10.1016/j.bioelechem.2014.03.008.
[55] J. Raso *et al.*, “Recommendations guidelines on the key information to be reported in studies of application of PEF technology in food and biotechnological processes,” *Innov. Food Sci. Emerg. Technol.*, vol. 37, pp. 312–321, Oct. 2016, doi: 10.1016/j.ifset.2016.08.003.

[56] M. Rebersek, D. Miklavcic, C. Bertacchini, and M. Sack, “Cell membrane electroporation-Part 3: the equipment,” *IEEE Electr. Insul. Mag.*, vol. 30, no. 3, pp. 8–18, May 2014, doi: 10.1109/MEI.2014.6804737.
[57] H. S. Fogler, *Elements of chemical reaction engineering*, Fifth edition. Boston: Prentice Hall, 2016.
[58] J. Morren, B. Roodenburg, and S. W. H. de Haan, “Electrochemical reactions and electrode corrosion in pulsed electric field (PEF) treatment chambers,” *Innov. Food Sci. Emerg. Technol.*, vol. 4, no. 3, pp. 285–295, Sept. 2003, doi: 10.1016/S1466-8564(03)00041-9.
[59] N. Boc *et al.*, “Ultrasonographic changes in the liver tumors as indicators of adequate tumor coverage with electric field for effective electrochemotherapy,” *Radiol. Oncol.*, vol. 52, no. 4, pp. 383–391, Oct. 2018, doi: 10.2478/raon-2018-0041.
[60] M. H. A. Groen *et al.*, “In vivo analysis of the origin and characteristics of gaseous microemboli during catheter-mediated irreversible electroporation,” *EP Eur.*, vol. 23, no. 1, pp. 139–146, Jan. 2021, doi: 10.1093/europace/euaa243.
[61] K. Neven *et al.*, “Absence of (sub-)acute cerebral events or lesions after electroporation ablation in the left-sided canine heart,” *Heart Rhythm*, vol. 18, no. 6, pp. 1004–1011, June 2021, doi: 10.1016/j.hrthm.2021.02.015.
[62] A. Kiss, E. Nagy-Baló, G. Sándorfi, I. Édes, and Z. Csanádi, “Cerebral microembolization during atrial fibrillation ablation: Comparison of different single-shot ablation techniques,” *Int. J. Cardiol.*, vol. 174, no. 2, pp. 276–281, June 2014, doi: 10.1016/j.ijcard.2014.03.175.
[63] C. Herrera Siklódy *et al.*, “Incidence of Asymptomatic Intracranial Embolic Events After Pulmonary Vein Isolation,” *J. Am. Coll. Cardiol.*, vol. 58, no. 7, pp. 681–688, Aug. 2011, doi: 10.1016/j.jacc.2011.04.010.
[64] A. Zupanic, S. Ribaric, and D. Miklavcic, “Increasing the repetition frequency of electric pulse delivery reduces unpleasant sensations that occur in electrochemotherapy,” *Neoplasma*, vol. 54, no. 3, pp. 246–250, 2007.
[65] T. Potočnik, D. Miklavčič, and A. Maček Lebar, “Gene transfer by electroporation with high frequency bipolar pulses in vitro,” *Bioelectrochemistry*, p. 107803, Mar. 2021, doi: 10.1016/j.bioelechem.2021.107803.
[66] S. Mahnič-Kalamiza and D. Miklavčič, “Scratching the electrode surface: Insights into a high-voltage pulsed-field application from in vitro & in silico studies in indifferent fluid,” *Electrochimica Acta*, vol. 363, p. 137187, Dec. 2020, doi: 10.1016/j.electacta.2020.137187.
[67] C. A. Schneider, W. S. Rasband, and K. W. Eliceiri, “NIH Image to ImageJ: 25 years of image analysis,” *Nat. Methods*, vol. 9, no. 7, pp. 671–675, July 2012, doi: 10.1038/nmeth.2089.
[68] R. B. McCleskey, “Electrical Conductivity of Electrolytes Found In Natural Waters from (5 to 90) °C,” *J. Chem. Eng. Data*, vol. 56, no. 2, pp. 317–327, Feb. 2011, doi: 10.1021/je101012n.
[69] G. D. Scott and D. M. Kilgour, “The density of random close packing of spheres,” *J. Phys. Appl. Phys.*, vol. 2, no. 6, pp. 863–866, June 1969, doi: 10.1088/0022-3727/2/6/311.
[70] H. Sun *et al.*, “Thermal and Electrical Conductivities of Platinum/Iridium Microwires,” *J. Electron. Mater.*, vol. 52, no. 3, pp. 2185–2192, Mar. 2023, doi: 10.1007/s11664-022-10190-z.

[71] R. Battino, T. R. Rettich, and T. Tominaga, “The Solubility of Nitrogen and Air in Liquids,” *J. Phys. Chem. Ref. Data*, vol. 13, no. 2, pp. 563–600, Apr. 1984, doi: 10.1063/1.555713.
[72] R. Battino, “The Ostwald coefficient of gas solubility,” *Fluid Phase Equilibria*, vol. 15, no. 3, pp. 231–240, Jan. 1984, doi: 10.1016/0378-3812(84)87009-0.
[73] T. J. Pfefer, B. Choi, G. Vargas, K. M. McNally, and A. J. Welch, “Pulsed Laser-Induced Thermal Damage in Whole Blood,” *J. Biomech. Eng.*, vol. 122, no. 2, pp. 196–202, Apr. 2000, doi: 10.1115/1.429642.
[74] E. Anter *et al.*, “Dual-energy lattice-tip ablation system for persistent atrial fibrillation: a randomized trial,” *Nat. Med.*, pp. 1–8, May 2024, doi: 10.1038/s41591-024-03022-6.
[75] V. Y. Reddy *et al.*, “Pulsed Field or Conventional Thermal Ablation for Paroxysmal Atrial Fibrillation,” *N. Engl. J. Med.*, vol. 389, no. 18, pp. 1660–1671, Nov. 2023, doi: 10.1056/NEJMoa2307291.
[76] A. Verma *et al.*, “Pulsed Field Ablation for the Treatment of Atrial Fibrillation: PULSED AF Pivotal Trial,” *Circulation*, vol. 147, no. 19, pp. 1422–1432, May 2023, doi: 10.1161/CIRCULATIONAHA.123.063988.
[77] K.-R. J. Chun *et al.*, “State-of-the-art pulsed field ablation for cardiac arrhythmias: ongoing evolution and future perspective,” *EP Eur.*, vol. 26, no. 6, p. euae134, June 2024, doi: 10.1093/europace/euae134.
[78] C. A. Martin, M. T. Zaw, N. Jackson, D. Morris, and P. Costanzo, “First worldwide use of pulsed-field ablation for ventricular tachycardia ablation via a retrograde approach,” *J. Cardiovasc. Electrophysiol.*, vol. 34, no. 8, pp. 1772–1775, Aug. 2023, doi: 10.1111/jce.16002.
[79] H. D. Yavin, K. Higuchi, J. Sroubek, A. Younes, I. Zilberman, and E. Anter, “Pulsed-Field Ablation in Ventricular Myocardium Using a Focal Catheter: The Impact of Application Repetition on Lesion Dimensions,” *Circ. Arrhythm. Electrophysiol.*, p. CIRCEP.121.010375, Aug. 2021, doi: 10.1161/CIRCEP.121.010375.
[80] M. van Zyl *et al.*, “Bipolar Electroporation Across the Interventricular Septum: Electrophysiological, Imaging, and Histopathological Characteristics,” *JACC Clin. Electrophysiol.*, vol. 8, no. 9, pp. 1106–1118, Sept. 2022, doi: 10.1016/j.jacep.2022.06.002.
[81] R. Willems, K. L. P. M. Janssens, P. H. M. Bovendeerd, C. V. Verhoosel, and O. Van Der Sluis, “An isogeometric analysis framework for ventricular cardiac mechanics,” *Comput. Mech.*, vol. 73, no. 3, pp. 465–506, Mar. 2024, doi: 10.1007/s00466-023-02376-x.
[82] K. L. Sack *et al.*, “Construction and Validation of Subject-Specific Biventricular Finite-Element Models of Healthy and Failing Swine Hearts From High-Resolution DT-MRI,” *Front. Physiol.*, vol. 9:539, May 2018, doi: 10.3389/fphys.2018.00539.
[83] Wei-Ning Lee *et al.*, “Mapping Myocardial Fiber Orientation Using Echocardiography-Based Shear Wave Imaging,” *IEEE Trans. Med. Imaging*, vol. 31, no. 3, pp. 554–562, Mar. 2012, doi: 10.1109/TMI.2011.2172690.
[84] S. N. Doost, D. Ghista, B. Su, L. Zhong, and Y. S. Morsi, “Heart blood flow simulation: a perspective review,” *Biomed. Eng. OnLine*, vol. 15, no. 1, p. 101, Dec. 2016, doi: 10.1186/s12938-016-0224-8.
[85] M. Gómez-Barea, T. García-Sánchez, and A. Ivorra, “A computational comparison of radiofrequency and pulsed field ablation in terms of lesion morphology in the cardiac chamber,” *Sci. Rep.*, vol. 12, no. 1, p. 16144, Sept. 2022, doi: 10.1038/s41598-022-20212-9.

[86] A. A. Joseph, D. Voit, and J. Frahm, “Inferior vena cava revisited – Real-time flow MRI of respiratory maneuvers,” *NMR Biomed.*, vol. 33, no. 4, p. e4232, Apr. 2020, doi: 10.1002/nbm.4232.
[87] A. González-Suárez, J. J. Pérez, R. M. Irastorza, A. D’Avila, and E. Berjano, “Computer modeling of radiofrequency cardiac ablation: 30 years of bioengineering research,” *Comput. Methods Programs Biomed.*, vol. 214, p. 106546, Feb. 2022, doi: 10.1016/j.cmpb.2021.106546.
[88] J. Pearce, “Mathematical models of laser-induced tissue thermal damage,” *Int. J. Hyperthermia*, vol. 27, no. 8, pp. 741–750, Dec. 2011, doi: 10.3109/02656736.2011.580822.
[89] A. Gonzalez-Suarez and E. Berjano, “Comparative Analysis of Different Methods of Modeling the Thermal Effect of Circulating Blood Flow During RF Cardiac Ablation,” *IEEE Trans. Biomed. Eng.*, vol. 63, no. 2, pp. 250–259, Feb. 2016, doi: 10.1109/TBME.2015.2451178.
[90] S. Corovic, I. Lackovic, P. Sustaric, T. Sustar, T. Rodic, and D. Miklavcic, “Modeling of electric field distribution in tissues during electroporation,” *Biomed. Eng. OnLine*, vol. 12, no. 1, p. 16, Dec. 2013, doi: 10.1186/1475-925X-12-16.
[91] P. A. Hasgall *et al.*, “IT’IS Database for thermal and electromagnetic parameters of biological tissues.,” no. Version 4.1, Feb. 2022, doi: 10.13099/VIP21000-04-1.
[92] Y. Salazar, R. Bragos, O. Casas, J. Cinca, and J. Rosell, “Transmural Versus Nontransmural In Situ Electrical Impedance Spectrum for Healthy, Ischemic, and Healed Myocardium,” *IEEE Trans. Biomed. Eng.*, vol. 51, no. 8, pp. 1421–1427, Aug. 2004, doi: 10.1109/TBME.2004.828030.
[93] J. Cinca, “Passive transmission of ischemic ST segment changes in low electrical resistance myocardial infarct scar in the pig,” *Cardiovasc. Res.*, vol. 40, no. 1, pp. 103–112, Oct. 1998, doi: 10.1016/S0008-6363(98)00145-X.
[94] G. Pucihar, J. Krmelj, M. Reberšek, T. Napotnik, and D. Miklavčič, “Equivalent Pulse Parameters for Electroporation,” *IEEE Trans. Biomed. Eng.*, vol. 58, no. 11, pp. 3279–3288, Nov. 2011, doi: 10.1109/TBME.2011.2167232.
[95] M. Casciola, T. K. Feaster, M. J. Caiola, D. Keck, and K. Blinova, “Human in vitro assay for irreversible electroporation cardiac ablation,” *Front. Physiol.*, vol. 13, p. 1064168, Jan. 2023, doi: 10.3389/fphys.2022.1064168.
[96] M. Casciola, A. Kaboudian, T. K. Feaster, A. Narkar, and K. Blinova, “Pulsed electric field performance calculator tool based on an in vitro human cardiac model,” *Front. Physiol.*, vol. 15, p. 1395923, June 2024, doi: 10.3389/fphys.2024.1395923.
[97] J. A. Vogel *et al.*, “Time-Dependent Impact of Irreversible Electroporation on Pancreas, Liver, Blood Vessels and Nerves: A Systematic Review of Experimental Studies,” *PloS One*, vol. 11, no. 11, p. e0166987, 2016, doi: 10.1371/journal.pone.0166987.
[98] E. J. Jacobs, K. N. Aycock, P. P. Santos, J. L. Tuohy, and R. V. Davalos, “Rapid estimation of electroporation-dependent tissue properties in canine lung tumors using a deep neural network,” *Biosens. Bioelectron.*, vol. 244, p. 115777, Jan. 2024, doi: 10.1016/j.bios.2023.115777.
[99] B. Mercadal, N. Beitel-White, K. N. Aycock, Q. Castellví, R. V. Davalos, and A. Ivorra, “Dynamics of Cell Death After Conventional IRE and H-FIRE Treatments,” *Ann. Biomed. Eng.*, vol. 48, no. 5, pp. 1451–1462, May 2020, doi: 10.1007/s10439-020-02462-8.
[100] D. Miklavčič, K. Beravs, D. Šemrov, M. Čemažar, F. Demšar, and G. Serša, “The Importance of Electric Field Distribution for Effective in Vivo Electroporation of

Tissues," *Biophys. J.*, vol. 74, no. 5, pp. 2152–2158, May 1998, doi: 10.1016/S0006-3495(98)77924-X.
[101] J. Zhang, P. F. Blackmore, B. Y. Hargrave, S. Xiao, S. J. Beebe, and K. H. Schoenbach, "Nanosecond pulse electric field (nanopulse): A novel non-ligand agonist for platelet activation," *Arch. Biochem. Biophys.*, vol. 471, no. 2, pp. 240–248, Mar. 2008, doi: 10.1016/j.abb.2007.12.009.
[102] S. Simcic, F. Bobanović, V. Kotnik, and L. Vodovnik, "Local changes in membrane potential intensify neutrophil oxidative burst," *Physiol. Chem. Phys. Med. NMR*, vol. 29, no. 1, pp. 39–47; discussion 47-50, 1997.
[103] S. Mohanty *et al.*, "Acute Kidney Injury Resulting From Hemoglobinuria After Pulsed-Field Ablation in Atrial Fibrillation: Is it Preventable?," *JACC Clin. Electrophysiol.*, vol. 10, no. 4, pp. 709–715, Apr. 2024, doi: 10.1016/j.jacep.2023.12.008.
[104] S. Venier *et al.*, "Severe acute kidney injury related to haemolysis after pulsed field ablation for atrial fibrillation," *EP Eur.*, vol. 26, no. 1, p. euad371, Jan. 2024, doi: 10.1093/europace/euad371.
[105] M. Nies *et al.*, "Hemolysis After Pulsed Field Ablation: Impact of Lesion Number and Catheter-Tissue Contact," *Circ. Arrhythm. Electrophysiol.*, vol. 17, no. 6, p. e012765, June 2024, doi: 10.1161/CIRCEP.124.012765.
[106] M. A. Popa *et al.*, "Characterization and Clinical Significance of Hemolysis After Pulsed Field Ablation for Atrial Fibrillation: Results of a Multicenter Analysis," *Circ. Arrhythm. Electrophysiol.*, vol. 17, no. 10, p. e012732, Oct. 2024, doi: 10.1161/CIRCEP.124.012732.
[107] A. Belalcazar and E. K. Heist, "Comparison of efficiency of PFA catheter designs by computer modeling," *J. Cardiovasc. Electrophysiol.*, p. jce.16459, Oct. 2024, doi: 10.1111/jce.16459.
[108] R. V. Davalos, L. M. Mir, and B. Rubinsky, "Tissue Ablation with Irreversible Electroporation," *Ann. Biomed. Eng.*, vol. 33, no. 2, pp. 223–231, Feb. 2005, doi: 10.1007/s10439-005-8981-8.
[109] A. Verma, P. Zhong, Q. Castellvi, S. Girouard, V. Mediratta, and R. E. Neal, "Thermal Profiles for Focal Pulsed Electric Field Ablation," *JACC Clin. Electrophysiol.*, p. S2405500X23002888, July 2023, doi: 10.1016/j.jacep.2023.05.005.
[110] G. Amorós-Figueras *et al.*, "Endocardial infarct scar recognition by myocardial electrical impedance is not influenced by changes in cardiac activation sequence," *Heart Rhythm*, vol. 15, no. 4, pp. 589–596, Apr. 2018, doi: 10.1016/j.hrthm.2017.11.031.
[111] D. Schwartzman, I. Chang, and M. S. Mirotznik, "Electrical Impedance Properties of Normal and Chronically Infarcted Left Ventricular Myocardium," p. 12.
[112] U. Sandhu *et al.*, "*In vivo* pulsed-field ablation in healthy vs. chronically infarcted ventricular myocardium: biophysical and histologic characterization," *EP Eur.*, p. euac252, Feb. 2023, doi: 10.1093/europace/euac252.
[113] L. Di Biase *et al.*, "Pulsed Field Ablation Index-Guided Ablation for Lesion Formation: Impact of Contact Force and Number of Applications in the Ventricular Model," *Circ. Arrhythm. Electrophysiol.*, vol. 17, no. 4, p. e012717, Apr. 2024, doi: 10.1161/CIRCEP.123.012717.